The physical space model of the icosahedral quasicrystal

正二十面体準結晶の物理空間モデル

Ireneusz Jozef Buganski

Crystal Physics Laboratory

Division of Applied Physics

Graduate School of Engineering

Hokkaido University

Sapporo, Japan

Table of Contents

Acknowledgments

I am very much in debt of **Assoc. Prof. Hiroyuki Takakura** who hosted me in Japan throughout my Ph.D. course at Hokkaido University and supervised my work. He was always there to explain to me the unknown and patiently correct me in the moments of flaws. This work could not be done without his support.

I am sincerely grateful to **Prof. Janusz Wolny** for inviting me to his laboratory when I was still an undergraduate student and taught me the principles of the quasicrystals.

I would like to acknowledge Mr. Y. Kaneko for his help in single crystal growth of ZnMgTm and Dr. T. Matsumoto, Rigaku oxford diffraction, for his help in single-crystal X-ray intensity data collection, the researchers form SOLEIL synchrotron facility who were kind to help with the X-ray diffraction measurement of the ZnMgHf quasicrystal.

Special thanks to **Kotoba Toyonaga** for a helping hand in all the in-house experiments and being my roommate at the university office.

Best regards to all members of our small Polish Community in Sapporo for guiding me through Japan and help to explore it like I could never without them.

I am grateful to **Patrycja Świeczkowska** for unbounded support.

Abstract

The scientific interest in the atomic structure of quasicrystals (QCs), has never faded since Dan Shechtman's discovery in 1982. So far, only about twenty QCs were analyzed quantitatively, which signifies how difficult the process of the structure analysis is. A lot of research has been dedicated to icosahedral (i) QCs in a Tsai-type family since the first binary Cd-Yb QC was discovered. In 2007, a highly-accurate atomic structure model of this QC, based on the cluster-approach, was developed. Since then, the model has served as a structural template for any other QC in this family. Such a template, however, does not exist for the Bergman family, which are formed mainly in the Zn-Mg-*R* (*R* = rare earth) systems. The discovery of Zn-Mg-*R* iQCs arose a great interest in their magnetic properties because well-localized magnetic moments are carried by the 4*f* electrons of the *R* ions which arrange quasiperiodically in the structure. Numerous measurements of magnetic moments show spin-glass-like behavior in a low-temperature regime. In order to explain the measured magnetic properties, a detailed atomic structure model of Bergman QC is needed and such a challenge was taken in this thesis.

In chapter one a thorough introduction to the crystallography of QCs is given. It starts with historical background about the first observation of structures with a translational symmetry being broken. A whole subsection is dedicated to the definition of QCs as there is still a nomenclature confusion, even among scientists working in the field. The chapter ends with a summary about every of four known types of QCs with forbidden symmetries and the motivation of the thesis is explained.

In chapter two the mathematical foundations of the crystallography of QCs are given. Two methods that were developed to represent mathematically the quasiperiodic structures are described in detail: the higher-dimensional approach, where the set of quasiperiodic points is lifted to nD space, with $n > 3$, for 3D structures and the Average Unit Cell approach (AUC). Those two approaches are shown to be complementary as long as the nD representation of the structure exists.

Chapter three focuses on the Ammann-Kramer-Neri tiling (AKNT), which was formerly known as three-dimensional Penrose tiling, and its application to the structure solution of iQCs. The AKNT is shown to be built of two prototiles: oblate and prolate rhombohedra, associated with a golden ratio. Their spatial arrangement ensures the icosahedral symmetry. The projection method, involving a higher-dimensional space is presented and a mathematical procedure of obtaining the AKNT from the nD space is discussed. The most important part of this chapter is a meticulous derivation of the structure factor of the AKNT. The AKNT serves as a quasilattice for the iQC and the geometric component of the structure factor is indispensable.

Chapter four is dedicated to the full analysis of the atomic structure of the Zn-Mg-Tm P-type iQC. It starts with a review of the literature on Bergman QCs. The details on the crystal growth method and the diffraction experiment are presented. The next two subsections focus on the *ab initio* structure solution by a charge flipping method and a consecutive structure refinement of the model. After that, decoration of the asymmetric part of the rhombohedral units with clusters was found. It is shown that

all the atoms belong to a triacontahedral cluster when the *a*-linkage along a 5-fold direction is allowed. In the end, the nD representation of the structure was plotted against a simple-decoration model. The refined model was proven to match the experimental results by calculating the crystallographic R factor equal to 9.8% and the residual electron density is less than 4%.

Chapter five is dedicated to the crystal growth and the local structure analysis of the Zn-Mg-Hf F-type iQC. It is also a Bergman QC, but due to the formation of the superstructure, the analysis is far more complicated. The 6D unit cell must be two times expanded in every direction with respect to the primitive lattice, resulting in having 32 centering translations. The experimental details are presented, including the first in the literature crystal growth, for this system, that ended with a high-quality monocrystals useful for X-ray diffraction. Based on the *ab initio* structure solution two types of clusters were identified. Both are Bergman-type but are differentiated by the preferential occupancy of the high-symmetry nodes of the rhombic triacontahedral shell by Hf elements.

Chapter six proceeds a discussion of the results and a research impact. First, the new model of the iQC, based on Zn-Mg-Tm system, is interpreted to show its significant differences with respect to the existing model of the Tsai-type QCs. First of all, the model is solved in the real space, not in the higher-dimensional space. Second, clusters are no longer building blocks of the structure and they appear as a result of atomic decoration of the rhombohedra of the AKNT with an edge length of 21.7 Å. Atomic clusters are no longer limited to be linked with *b* and *c* linkages but the additional *a* linkage is permitted. It is supported by the analysis of the electron density in the *ab initio* structure solution. The F-type Bergman QC manifests the same linkages even though two types of clusters must be considered. In the future perspective, the new model of Bergman QC will be generalized to all families of iQC, including F-type superstructure.

1. Introduction

Crystallography as a branch of science matured at the beginning of the XXth century when Max von Laue collected the first diffraction diagram of the X-ray radiation scattered over copper sulfate as a medium [1]. One year later William Lawrance Bragg together with his father William Henry Bragg conducted a series of experiments using a variety of crystals including pyrite, sodium chloride, quartz, etc. Their research concluded with the formulation of a law known today as the Braggs law [2]. According to this law, the maxims of the interference peaks occur for the specifically defined scattering angles. As stated in their paper, the diffraction peak is formed by beams reflected by adjacent crystallographic planes. The condition of the constructive interference between beams is realized only for certain angles. The model was vastly accepted by the research community and the crystallographic plane became a fundamental idea standing behind every analysis of the crystallographic structure.

The concept of the periodicity being an inherent feature of every crystal dates back to the XVIIIth century and the work of Rene-Just Hauy. This French investigator was mesmerized by the broken calcite crystal which preserved its geometrical shape after several steps involving cutting it into smaller and smaller pieces. He concluded, it must be therefore built of an elementary building block that in the end could not be divided without changing the properties of the material. The discovery was published in 1784 in the book *Essai d'une theorie sur la structure des crystaux* [3]. He is also responsible for the formulation of the symmetry rule. According to the rule only 1-, 2-, 3-, 4- and 6-fold rotational axis is possible in a crystal. This law is partially indebted to Johannes Kepler who substantiated that the 2D plane can be covered precisely by three polygons: the triangle, the square and the hexagon [4]. The covering by pentagons was always resulting in voids shaped into five-pointed stars. That observation was yet to be rediscovered.

The dogma about periodicity as an indispensable part of the crystalline structure order became a motor of the progress. The unified group theory of crystals was developed by Auguste Bravais, Arthur Moritz Schoenflies and Jewgraf Fedorow [5, 6]. Later the mathematical methodology of the crystal structure solution was enriched by Arthur Lindo Patterson [7], Herbert Hauptman [8] and Jerome Karle [9]. The belief in a periodic invariance of the crystallographic lattice was constantly reassured by many diffraction experiments with different radiation sources.

The first indication that the periodic symmetry can be broken was observed in 1927 by Dehlinger [10]. The additional lines in the Debye-Scherrer pattern could be explained by the periodical perturbation of the atomic positions. The modulation function in the reciprocal space was represented by the supplementary modulation vector required to index all the peaks. The peaks that did not match the periodic structure were called satellite reflections.

Another type of modulation was spotted by Preston in the transitive phase of the AlCu alloy [11] and by Daniel and Lipson in Cu_4FeNi_3 [12]. The displacive modulation did not result in the reproduction

of the diffraction pattern. Only later, Hargreaves proposed the addition of the occupational modulation [13].

All the previous modulation vectors were commensurate with respect to the average structure. The first observation of the incommensurate modulation was made in AuCu alloy by Fujiwara [14]. Later, the incommensurate modulation was observed in the magnetic structure of rare-earth based alloys and since then, modulated structures are frequently found in many inorganic and biological crystals [15].

The breakthrough in the analysis of the incommensurately modulated structures was made by independent research of de Wolff [16] and Janner [17]. They both introduced the concept of the higher-dimensional analysis. The main concept behind it is the existence of the multidimensional space that is periodical. Every modulation vector that is required to index the diffraction pattern increases the dimension of the multidimensional space by one. This mathematical analysis became, and still is, the basic tool for the structure solution of aperiodic crystals, implemented in, e.g. JANA2006 [18] and most recent version JANA2020.

1.1 The discovery of quasicrystals

The first officially known quasicrystal was discovered during a routine investigation of the rapidly cooled AlMn alloy in 1982 [19]. When the sample was scanned using the electron microscope the diffraction pattern exhibiting a 10-fold rotational axis was observed by Dan Shechtman what was meticulously noted in the lab book. Later, the 2-fold and 6-fold axis was also found in the same phase (Fig. 1 b) [19]). The angles under which each rotational axis was perceivable agreed with the icosahedral symmetry (Fig. 1 c) [19]); the odd-rotational symmetry was doubled due to Friedl's law, therefore the sample exhibited 2-, 3- and 5-fold symmetry). Furthermore, the diffraction pattern could not be indexed in any known crystallographic setting. It must be emphasized that the local 5-fold rotational axis is prevalent in crystallography however, it cannot be associated with a long-range order of the crystallographic system if the structure is periodic. Furthermore, the stability tests proved the AlMn alloy was sensitive to the initial composition and the annealing time. When the sample was rapidly cooled only the amorphous phase could be obtained, slow cooling resulted in crystallization of the stable, periodic Al_6Mn phase. The icosahedral phase containing 14% of manganese was metastable.

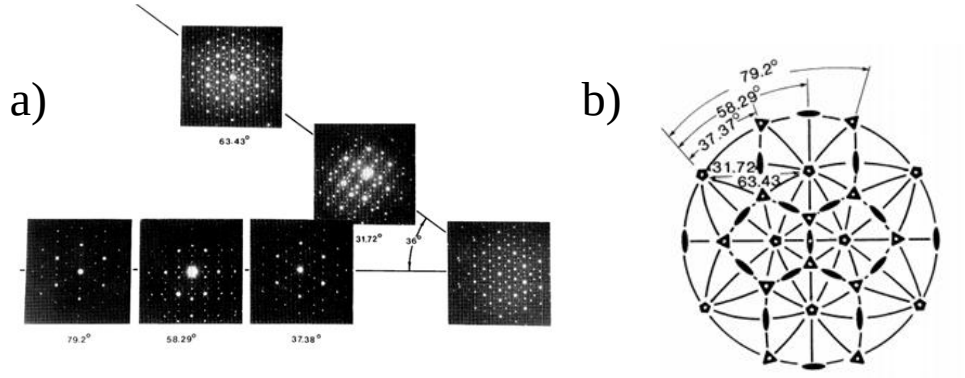

Figure 1. a) The electron diffraction pattern of rapidly cooled AlMn alloy seen at specific orientations of the sample, agreeing with the icosahedral point symmetry. Source: [19]; b) the stereographic projection of icosahedral symmetry. Source: [19]

The publication was accepted in November of 1984 by Physical Review Letters after two years of the fierce battle with referees who rejected the possibility of the global 5-fold rotational symmetry being realized in a crystalline material [19]. It could not happen without the support of crystallographers: Ilan Blech, John Cahn and Denis Gratias who were listed as co-authors of the publication. Five weeks after the publication, Paul Steinhardt and Don Levine reported a geometrical construction, based on the arrangement of two rhombohedral units that realized an icosahedral symmetry [20]. Their work was based on the earlier work of Alan Mackay [21], Robert Ammann [22] and Roger Penrose [23]. In this article, the name *quasicrystal* was used for the first time in reference to crystals with a symmetry forbidden by classical crystallography.

The most fierce opponent of the Shechtman's discovery was Linus Pauling, a two times Nobel Prize nominee. In 1985 he published a model of multiple twins of the cubic crystals that lead to the 5-fold symmetry axis [24]. For the model to work 1000 atoms were included in the unit cell. In the same year, the model was abolished by Bancel *et al.* [25]. Only after 1987, when An-Pang Tsai from Tohoku University discovered the first stable icosahedral quasicrystal in AlCuFe alloy [26], Pauling accepted quasicrystals as a legitimate phase. The famous Pauling's quote best describe his disdains of Shechtman's discovery: "There are no quasicrystals, only quasi-scientists". Ironically, Dan Shechtman was awarded the Nobel Prize in Chemistry in 2011.

After the discovery of numerous examples where periodic symmetry was broken, the International Union of Crystallography [27] announced the rephrasing of the definition of the crystal in 1991 by removing the condition that material displays a periodic symmetry. In the article published in 1992 in Acta Crystallographica A: Foundations and Advances we can read that: " … *by crystal we mean any solid having an essentially discrete diffraction diagram and by aperiodic crystal we mean any crystal*

in which three-dimensional lattice periodicity can be considered to be absent ". The crystal is not defined by its intrinsic properties or morphology but by its ability to create a discreet diffraction pattern.

1.2 The definition of quasicrystal

It is generally accepted that crystal is a solid possessing a long-range positional order. It justifies the decision of the Commission of Aperiodic Crystals, that works under the wings of IUCr, to shift from the microscopic definition of the crystal to a property expressed by the experimental setup [27]. The Bragg peaks are a valid indication of the existence of the long-range order. The definition that was decided to be temporary until a better understanding of the concept of order arises, stays to this day. The current definition is not only consistent with the notion of the long-range order used in condensed matter physics but also it is vague enough to not impose untrue constrains until more thorough research on the issue the realization of order is conducted.

Crystals that possess a periodic symmetry are called *periodic crystals* and all others are called *aperiodic crystals*. There is still a problem of defining what a quasicrystal is. The common practice of associating quasicrystals with structures manifesting a symmetry axis incompatible with a periodic symmetry is wrong. We could go along the definition of *quasicrystal* proposed by Steinhardt and Levine, which is an abbreviation of *quasiaperiodic crystal* following the mathematical definition of quasiperiodicity (which includes periodicity as a special case) [28]. Let's consider a function $\rho(\mathbf{r})$ that can be expanded into a superposition of the countable number of plane waves:

$$\rho(\mathbf{r}) = \sum_{k \in \boldsymbol{V}^*} \rho(\mathbf{k}) \exp(i\mathbf{kr}), \tag{1.1}$$

where $\mathbf{k} = \sum_{i=1}^{D} h_i \mathbf{d}_i^*$, $h_i \in \mathbb{Z}$. If all the wave vectors from the linear space $\mathbf{V}^*$, spanned by base vectors $\mathbf{a}_i^*$, can be represented as the linear combination of D base vectors with integer coefficients, than the function $\rho(\mathbf{r})$ is called *quasiperiodic*. The diffraction pattern of the quasiperiodic crystal can be therefore indexed with D integers. It can be clearly understood from (1.1) that periodic crystal is a subset of all quasiperiodic crystals for which D is equal to the physical dimension d. Only for a periodic crystal, the set of Bragg peaks is truly discreet. For quasiperiodic crystal with $D > d$ the Fourier spectrum is dense – the distance between two wave vectors in a Fourier spectrum in the limit equal to 0. Experimentally, we cannot observe Bragg peaks below a certain threshold therefore the diffraction pattern in essentially discreet.

Among quasiperiodic crystals, there are classes that do not challenge the paradigm of the periodicity and are known for a long time. Incommensurately modulated crystals and incommensurate composite crystals possess an aspect of periodicity. The former is just a periodically perturbed basic

periodic structure. The latter is a system composed of two or more interpenetrating subsystems that are mutually incommensurate. The peaks of the diffraction pattern of such crystals can be divided into two groups: main reflections, that are significantly brighter, describing an average structure and possible to be indexed in the periodic space group and satellite peaks arising from the modulation function. The crystal discovered by Shechtman [19] could not be pictured as the modification of the periodic structure and was intrinsically quasiperiodic due to the existence of the 5-fold symmetry. The term *quasicrystal* is frequently wrongly reserved for crystals with 'non-crystallographic' symmetry to set them apart from modulated structures. It comes from the need for differentiating modulated structures from innate quasiperiodic one. However, the criterion under which modulated and 'intrinsically quasiperiodic' structures could be separated is not easy to find. First of all, the diffraction pattern of modulated structure should manifest clear contrast between strong main reflections and weak satellite reflections but at some point, the discrepancy would fade e.g. when the amplitude of modulation engrossed. It is also evident in the case of modulation functions other than simple harmonic modulation. The simulation shows that by adding higher harmonics there exists a transition from the simple harmonic modulation to sawtooth modulation characteristic for the Fibonacci chain, which is generally referred to as a 1D quasicrystal [29]. The Fibonacci chain has both 'quasicrystalline' and modulated structure features. Namely, it can be viewed as a tiling of two units arranged aperiodically or resulting from substitution rules or be pictured as periodically modulated average periodic structure. It is therefore not evident which structure should be referred to as modulated structures and which as inborn quasiperiodic structures. The argument about the existence of the 'forbidden' crystallographic symmetry is also misguided because there are various examples of tiling models with 'crystallographic' point group symmetry. A very good example of such is a square Fibonacci tiling being a generalization of the Fibonacci chain with a 4-fold rotational symmetry [30]. It has a finite number of tiles with a determined tile frequency and finite number of vertex environments. Recently, it was reported that a square Fibonacci tiling can be used to characterize a distribution of fullerene particles deposited on the quasicrystalline 2-fold plane [31]. It is therefore not only a mathematical construction but a model realizable experimentally.

To conclude the discussion on the definition of quasicrystal, the best yet definition is one given by Steinhardt and Levine i.e. the quasicrystal is a quasiperiodic crystal in a mathematical sense of the word '*quasiperiodic*'. Since the periodic crystal falls into this definition it can be specified that quasicrystal has $D > d$. The definition was suggested by Ron Lifshitz [32, 33] and in my opinion, it is the best since the contrast between modulated and non-modulated structures is currently quantitatively impossible.

In later parts of the thesis I describe only quasicrystal that are incompatible with a periodic symmetry.

1.3 Quasicrystalline strucutres

From the statistical point of view, the quasiperiodic arrangement is rarely encountered in a laboratory environment, not mentioning naturally observed quasicrytsals. The main structural database contains more than 1 200 000 entries for periodic structures among which >188 000 belong to intermetallic/inorganic compounds. In comparison, the Bilbao Incommensurate Structures Database list 152 incommensurate structures[1] (with 24 composites). When it comes to quasicrystals with a forbidden symmetry only ~20 are quantitatively determined among ~50 known stable quasicrystals [34]. All of them are of laboratory provenience but there are quasicrystals discovered in nature. In the samples of mineral khatyrkite presumably coming from the Koryak region encompassing the northern part of the Kamchatka peninsula the AlCuFe icosahedral phase was found [35]. The stoichiometry was reported to be close to the synthetic counterpart. Since 2009 three quasicrystals, two icosahedral in AlCuFe system ($Al_{65}Cu_{20}Fe_{15}$ – phase I and $Al_{62}Cu_{31.2}Fe_{6.8}$ – phase II) [36] and one decagonal in $Al_{71}Ni_{24}Fe_3$ [37], were reported based on the analysis of the rock sample. Even though in the beginning it was assumed that the rock sample was naturally made in a geological process, the evidence unambiguously indicates it is a part of the meteorite [38].

In theory, there is no restriction on what rotational symmetry a quasicrystal can have. However, only selected are realized in nature. In fact only 5-fold and 10-fold symmetry quasicrystals are stable among reported structures [39]. It can be justified by the observation that the icosahedral coordination is the most frequent atomic environment type in intermetallic phases [40]. There are however few reports of the quasicrystals with 8-fold [41] and 12-fold symmetry [42, 43]. However, they are considered metastable or disordered. Sometimes the 1D quasicrystals are also mentioned due to the existence of the characteristic $\tau = (1 + \sqrt{5})/2$ scaling, observable in quasicrystals with forbidden symmetry, but they can be well enough considered as modulated structures, therefore I do not go into their more detailed description.

1.3.1 The icosahedral quasicrystal

The icosahedral quasicrystals are quasiperiodic in all three dimensions of the real space and possess an icosahedral point group symmetry. So far only icosahedral quasicrystals are truly 3D aperiodic. There is a report of the 3D quasicrystal with a crystallographic point group symmetry but it has a well-identifiable lattice of main reflections, therefore it can be analyzed as a modulated structure [44]. The quasicrystal belonging to the icosahedral family was the first synthesized quasicrystal recognized to form an aperiodic structure in 1982 [19]. Surprisingly, many today known quasicrystals were identified before Shechtman's discovery but the researchers did not realize the revelation, e. g. the aluminum-rich part of the Al-Cu-Fe system was studied, with a new phase reported in 1939 [45]. Only

[1] The number of entries checked in the 26th of February 2020

in the late 80s, it was recognized as quasicrystalline [26]. The same applied to Al-Cu-Li [46] which was ironically the first stable quasicrystal ever synthesized [47]. In addition, the first system that forms a binary quasicrystal was obtained in 1971/72 [48, 49] but it had to be rediscovered in 2000 [50, 51].

There are three types of icosahedral quasicrystals based on the prevalent type of the atomic cluster in the structure (Fig. 2). There can be either Mackay or pseudo-Mackay cluster [52], the Bergman cluster [53] and the Tsai cluster [51]. The distinction is not potent since there are examples when two types of clusters are needed to properly account all the atoms. That is principally correct in terms of the face-centered icosahedral Mackay quasicrystal where both Mackay and Bergman clusters are needed for the structure description. It also applies to Tsai primitive icosahedral phase. Even though the structure is packed with Tsai clusters, according to the structure model, within the interstitial part of the structure the Bergman clusters appear. Nevertheless, such a classification of icosahedral quasicrystal types is standard in the literature. The justification for such nomenclature is the point density of one type of cluster, the quasicrystal is classified according to, is dominant.

The Mackay quasicrystals are all based on Al as the main element, Cu or Pd as the second constituent and a transition metal of group 7 or 8 as the third component. The majority of them are face-centered phases. The edge-length of the rhombohedral unit is ranging from $4.5\text{Å} - 4.6\text{Å}$ [54]. One of the most stable quasicrystal forming high-quality monocrystals is belonging to this category of icosahedral quasicrystals. It is AlCuFe phase and as was mentioned before, it is also the first quasicrystal encounter in natural environment.

The Bergman quasicrystals are frequently referred to as Frank-Kasper quasicrystals because their periodical approximant crystals form tetrahedrally close-packed structures [55]. Almost all known Bergman quasicrystals are Zn-Mg based with the third element to be transition metal or rare-earth element. The only exceptions are the first discovered stable quasicrystal Al-Cu-Li [47] and Ti-Zr-Ni [56, 57]. Also, Al-Zn-Mg [58] is exceptional since it contains a *p* group element. Al-Zn-Mg is important for two reasons: it was the first structure investigated with a simple decoration model of the icosahedral structure and recently bulk superconductivity was reported in this system at 40 mK [59]. The rhombohedral edge-length varies from $5\text{Å} - 5.2\text{Å}$ [54].

Last but not least is the Tsai type quasicrystal that was the latest type of the icosahedral quasicrystal to be discovered. The discovery brought a major novelty to the understanding of the quasiperiodic order as Tsai type quasicrystals can exist as stable binary phases including Cd-Ca, Cd-Yb [50] and Zn-Sc [60, 61]. It shown that chemical entropy is not needed for the quasicrystalline phase to be formed. When it comes to the structure solution, the modeling of the atomic structure of the $Cd_{5.7}Yb$ brought the best-known model of the icosahedral quasicrystal that was utilized to solve vast instances of the structures [62]. The existence of only two elements in the structure that differ significantly in terms of the scattering power of the X-ray radiation (The atomic number for Cd is $Z = 48$ and for Yb is $Z = 70$) decreased the degrees of freedom for the strucutre modelling and helped to designate the exact

places where specific atom can be. It is the richest family of quasicrystals and possibly the most varied in terms of types of elements. It is mostly formed by Cd and Zn-Sc based alloys with an edge-length varying from 4.9Å for Zn-Sc based quasicrystal to 5.7Å for Cd-Rare Earth alloys. The family of the Tsai periodic approximant crystal is even greater with numerous 1/1 approximants with a bcc symmetry $Im\bar{3}$.

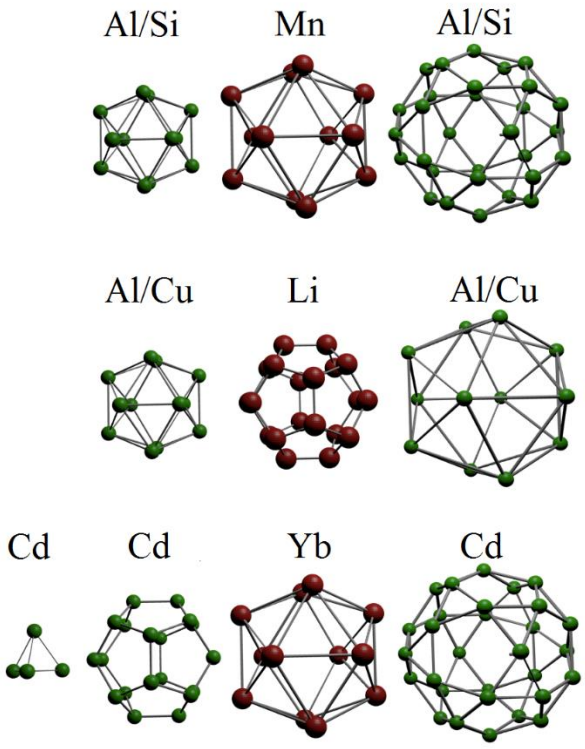

Figure 2. The local atomic clusters that constitute the basic building block of the icosahedral quasicrystals. Top: Mackay cluster in AlSiMn system; Mid: Bergman cluster in AlCuLi system; Bottom: Tsai cluster in *i*-CdYb.

Icosahedral quasicrystals are considered to be Hume-Rothery alloys [63] where the ratio between the number of valance electrons and number of atoms plays a crucial role together with the ratio between valance radius of the atoms [64]. Typically Mackay quasicrystals have $e/a \approx 1.75$, Bergman quasicrystals have $e/a \approx 2.1$ and for Tsai quasicrystals $e/a \approx 2.15$ [65]. In addition, the increase in the valance atomic radii influence the formation of the quasicrystal from a different family what was observed for ternary Zn-Mg based alloys [66].

All known icosahedral quasicrystals are either face-centered or primitive phases. No indication of the body-centered icosahedral quasicrystal occurring in a real system exists. On the other hand. all theoretical simulations of the icosahedral quasicrystal based on a Lenard-Jones-Gauss potential or a

free-energy minimization result in a body-centred icosahedral phase [67, 68]. That is an interesting discrepancy between simulation and experiment but it is possibly caused by simulations being performed upon one-element systems which are proven to prefer a body-centered type of the structure [69].

1.3.2 The decagonal quasicrystal

The first reported metastable decagonal quasicrystal belongs to a rapidly cooled Al-Mn system [70, 71]. Surprisingly, the first stable decagonal quasicrystal was discovered in 1982 in $Al_{10}FeNi_3$but [72] was not identified as such until 1994 [73]. Officially, the stable decagonal quasicrystal was first reported in 1988 in the Al-Cu-Co system with a composition $Al_{65}Cu_{15}Co_{20}$ [74].

The decagonal phase belongs to the class of axial quasicrystal that displays the aperiodic pattern in a 2D plane but is periodic in the third direction, perpendicular to this plane. The characteristic trait of the decagonal phase is the existence of the decagonal diffraction symmetry $10/m$ or $10/mmm$. The 10-fold symmetry axis is parallel to the periodic direction. The decagonal quasicrystal is not periodic from layer to layer but is a stacking of 2, 4, 6 or 8 layers of atoms within one period. All known stable decagonal quasicrystals are ternary alloys with 2-, 4- and 6-layer periodicity. They are Al and Zn based compounds with few instances of Ga based 6-layer periodic metastable phase [75].

The structure of a decagonal quasicrystal is usually solved by arranging atomic clusters in vertices of the quasiperiodic tiling [76, 77, 78]. They are just structural building units that form a favorable local atomic environment including the rules of the constellation. Two clusters can overlap with atomic positions mutually coincide or no, therefore creating a split atomic position providing a space for a so-called phason flip [79, 80]. In most cases, two different clusters are needed to properly recreate the structure of decagonal quasicrystal but there is an example of the structure where only one 20 nm and symmetry $\overline{10}2m$ decagonal cluster is needed [81]. The $Al_{64}Cu_{14}Co_{22}$ phase was identified as a 4-layer disordered phase but modeled with 2-layer periodicity due to the low resolution of the electron micrography. The interesting feature is all the clusters in the structure have the same orientation and there is only one allowed way of overlapping. It is an isostructure to the decagonal Al-Cu-Ir and Al-Cu-Rh phase investigated by Kuczera *et al.* [82]. The X-ray diffraction dataset of Al-Cu-Rh is one of the highest quality obtainable for the decagonal quasicrystal with 2092 symmetrically independent reflections. Currently, it is used to investigate the limits of the decagonal structure modelling by incorporation of phason flips models, phenomenological multiple-scattering effects and new types of phonon corrections that assume uncorrelated local atomic oscillations [83, 84]. So far the best result of the refinement with the data is expressed in the crystallographic R- factor value equal to 6.08%.

1.3.3 The Octagonal quasicrystal

The octagonal phase was discovered in 1987 in rapidly solidified V-Ni-Si and Cr-Ni-Si alloys [85]. Currently, there are only four known octagonal quasicrystals in intermetallic alloys [86, 85, 87, 88]. A detailed model of the $Mn_{80}Si_{15}Al_5$ was derived from HREM images under near-Scherzer defocus condition [89, 90]. The symmetry was determined to be $8_4/mmc$. The screw axis arises as a consequence of the mutual orientation of the second and fourth atomic plane, called *B* and *B'* respectively in the paper, along the periodic direction. Those two planes are rotated with respect to each other by $45°$. In total there are four atomic layers within 6.3 Å period. Only the first layer and the third, which share the same atomic decoration, display the 8-fold symmetry. Layers *B* and *B*' have tetragonal symmetry.

The atomic model of the structure was based on the Ammann-Beenker tiling with an edge-length of 8.2 Å. It is a two-tile tiling with squares and rhombuses with an acute angle of $45°$. The cluster model of the structure with an octagonal cluster covering was proposed by Ben-Abraham and Gähler in 1999 [41]. It was suggested that the formation of the densely packed atomic clusters governs the formation and stabilization of the aperiodic long-range order.

Even though the 8-fold symmetry is not observed frequently in intermetallic compounds it is manufactured in metamaterials to obtain preferable optical properties [91].

1.3.4 The dodecagonal quasicrystal

The dodecagonal 12-fold symmetry was first observed in Ni-Cr small particles and was originally called 'crystalloids' [42, 92]. The size of particles varied from 200 to 2000 Å in diameter. Even though the region of observation was narrow due to the limited size of the quasiperiodic phase, the characteristic square-triangle tiling with a few defects related to $30°$ rhombuses could be observed. The geometry of the dodecagonal quasilattice was originally proposed by Niizeki and Gahler [93, 94] based on the projection method. Similar tiling can be generated by the inflation method with a factor of $2 + \sqrt{3}$ but this method, contrary to the projection method, is not deterministic [95]. The final tiling realizes two possible orientations of dodecagons that corresponds to the phason disorder [96]. The tiling consists of the equilateral triangle, the square and $30°$ thin rhombus but the rhombus is rarely occurring in real quasicrystals, therefore the occupation domain that generates the tiling must be engineered to create a correct rhombus-to-other prototiles ratio [94].

The second examples of the dodecagonal quasicrystals were rapidly solidified Vi_3Ni_2 and $Vi_{15}Ni_{10}Si$ alloys. Even though the region of quasicrystal was larger in the second case, still the thin rhombus was the occasional defect. The periodicity along the 12-fold direction was equal to 4.5 Å [97].

The first stable dodecagonal quasicrystal was synthesized in 1995 in $Ta_{1.6}Te$ [98]. It has a 20.79 Å period along the 12-fold direction and well-corresponds to the square-triangle tiling in the

aperiodic plane. It is regarded as a random tiling structure with a second generation tiles with an edge length of 20 Å.

One of the latest dodecagonal quasicrystals is Mn-rich Mn-Cr-Ni-Si alloy synthesized with an electric arc melting technique and later annealed in 700°C [99]. The symmetry of the quasicrystal is $12/mmm$. The atomic model of the quasicrystal was based on the hexagonal approximant phase co-existing in this system. The comparison of the calculated electron diffraction pattern and measured one was in a good agreement.

Currently, the hot topic when it comes to dodecagonal quasicrystals in the observation of the first oxide quasicrystal derived from $BaTiO_3$ [43]. Later the family of oxide quasicrystals was extended for $SrTiO_3$ and its periodic approximants [100]. The atomic positions derived from HRTEM images correspond well with an ideal Niizeki-Gahler tiling showing the abundance of three tiles: the square, the equilateral triangle and thin rhombus in almost ideal frequency [101]. The recent study of the orientational distribution of each of the tiles shows an almost ideal agreement with the Niizeki-Gahler tiling presenting only 10% deviation from the homogeneous orientational distribution of squares, indicating the phasonic disorder in not significant, being a good candidate to investigate by the analytical model of phason flips [83].

1.4 Motivation and aim of the thesis

The thesis addresses a very important missing piece in the study of the structure of the icosahedral quasicrystal. So far the detailed structure of quasicrystals belonging to two families is known i. e. the Mackay and Tsai type quasicrystals. The model of the Tsai-type quasicrystal was introduced for binary Cd-Yb in 2007 by Takakura *et. al.* [62] and extends the cluster shells by the rhombic triacontahedral shell becoming a part of a basic building block of the structure with two rhombohedral units filling the interstitial structure. The model of Mackay quasicrystal was proposed by Katz and Gratias in 1993 for Al-Cu-Fe [102] and is currently modified for the F-type Al-Cu-Ru quasicrystal to also encompass the cluster description. Even though the models of icosahedral quasicrystals are so successful, the attempt to model the Bergman type quasicrystal with the same principle did not result in a reliable model. The most problematic aspect of the structure seems the atomic decoration of the rhombohedra in the interstitial part is not unique and depends on the local vertex environment. Independent models of the Bergman quasicrystal appeared in the late 80s and early 90s but all faced the same issue – the chemical mixing between atomic elements was not physically substantiated [103, 104]. As consequence, models were too defected to be considered valid. The motivation was to develop a new model that presents a high-quality reliable atomic structure of the Bergman quasicrystal.

My work introduces two major novelties. First of all, the structure of the P-type Zn-Mg-Tm icosahedral Bergman quasicrystal is solved using an innovative theoretical description within the framework of the tiling-and-decoration approach [55, 105]. The Ammann-Kramer-Neri tiling [106] is

used to find a unique decoration of rhombohedral units that correspond to *ab initio* structure solution by SUPERFLIP software [107]. The very good agreement with the experimental X-ray diffraction was achieved. The key point is the higher-dimensional approach was not used in calculations and the refinement was fully conducted in the physical space of the crystal. A similar approach has already been used for decagonal phases before but is the first instance such an approach was ventured for the icosahedral quasicrystal. It is hardly a simple generalization of the approach for 3D quasicrystals because both differ in a long-range order.

Further research is dedicated to the local structure of the F-type Zn-Mg-Hf Bergman quasicrystal. This quasicrystal has never been obtained before in a quality adequate for the X-ray single-crystal diffraction, therefore my study is the first carried out on a high-quality sample with a synchrotron radiation. Even though the thesis does not present a final, infinite structure model of the F-type Bergman quasicrystal, I point out several observations of the local structure that can be used I the future as a guide for the development of the complete model.

The calculations were performed in a self-written code prepared in MATLAB software environment. To my knowledge, it is the only existing code, beside QUASI07_08 software [108, 109], that allows to solve and refine the structure of the icosahedral quasicrystal.

2. The mathematical description of quasicrystals

The structural analysis of aperiodic crystals is a challenging task on the grounds of the mathematical apparatus required to carry out the calculations. It is not different in a way it tries to replace the kinematical approximation of the diffraction. The reflection intensity is still the square of the crystal structure factor calculated for the scattering vector of the reflection. The problem is how to obtain a structure factor formula. There are two complementary and yet fundamentally diverse approaches: The higher dimensional (nD) approach [110, 111, 112, 113] and the Average Unit Cell (AUC) approach, also called the statistical approach [114, 115, 116].

2.1 The higher-dimensional approach

Following the definition of the quasicrystal introduced in section 1.2 and formula (1.1), the electron density of the quasicrystal can be expressed as a Fourier Transform on a $\mathbb{Z}$-module. The number of basis vectors required in the Fourier spectrum is equal to D. In the kinematical approach, the structure factor is a Fourier Transform of the crystal lattice, therefore the number of basis vectors required to index the diffraction pattern is equal to the rank D of the quasicrystal. Each vector $\mathbf{k}$ of the reciprocal space is equal to the linear combination of the basis vectors with integer coefficients: $\mathbf{k} = \sum_{i=1}^{D} h_i \mathbf{d}_i^*$, $h_i \in \mathbb{Z}$. Each basis vector $\mathbf{d}_i^*$ in a Fourier spectrum of the quasicrystal can be lifted to the nD space, spanning the $\mathbf{V}^*$ space. The higher-dimensional approach is therefore based on reciprocal space information provided by the diffraction experiment. The direct space $\mathbf{V}$ can be constructed assuming a known relation between vectors of a direct and reciprocal space: $\mathbf{d}_i^* \mathbf{d}_j = 2\pi\delta_{ij}$. The direct space $\mathbf{V}$ is spanned by vectors $\mathbf{d}_j$ and has a dimension D equal to the dimension of the reciprocal space. The linear combination of basis vectors $\mathbf{d}_j$ forms a periodic lattice $\mathbf{L}$ embedded in the nD space.

The nD approach restores all symmetries and correlations of the quasicrystal. The number of possible space groups in the nD space is enormous. Even for $n = 4$ there are 4894 space groups with 271 point groups [117]. Not all the space groups are practically important. The orientation of the symmetry elements in the nD is defined by the isomorphism of the 3D and the nD point group. For instance, there are only two point groups for quasicrystals with an icosahedral symmetry: $m\bar{3}\bar{5}$ of order 120 and 235 of order 60. Table 1. shows all 11 6D space groups that leave the hypercrystal invariant, the point group of which are isomorphous to the two possible icosahedral point groups. So far all known quasicrystals were identified to have a $Pm\bar{3}\bar{5}$ and $Fm\bar{3}\bar{5}$ symmetry. Complementary space groups exist for other types of quasicrystals as well, but since the thesis focuses on the icosahedral quasicrystals detail for other classes of aperiodic structures are not presented.

Table 1. 3D point groups of order k corresponding to 6D space groups with icosahedral symmetry [118, 119].

3D point group	$\boldsymbol{k}$	6D space group	Reflection conditions
$\boldsymbol{m\bar{3}\bar{5}}$	120	$Pm\bar{3}\bar{5}$	none
		$Pn\bar{3}\bar{5}$	$h_1h_2\bar{h}_1\bar{h}_2h_5h_6$: $h_5 - h_6 = 2n$
		$Im\bar{3}\bar{5}$	$h_1h_2h_3h_4h_5h_6$: $\sum_{i=1}^{6} h_i = 2n$
		$Fm\bar{3}\bar{5}$	$h_1h_2h_3h_4h_5h_6$: $\sum_{i\neq j=1}^{6} h_i + h_j = 2n$
		$Fn\bar{3}\bar{5}$	$h_1h_2h_3h_4h_5h_6$: $\sum_{i\neq j=1}^{6} h_i + h_j = 2n$ $h_1h_2\bar{h}_1\bar{h}_2h_5h_6$: $h_5 - h_6 = 2n$
235	60	$P235$	none
		$P235_1$	$h_1h_2h_3h_4h_5h_6$: $h_1 = 5n$
		$I235$	$h_1h_2h_3h_4h_5h_6$: $\sum_{i=1}^{6} h_i = 2n$
		$I235_1$	$h_1h_2h_3h_4h_5h_6$: $\sum_{i=1}^{6} h_i = 2n$
		$F235$	$h_1h_2h_3h_4h_5h_6$: $\sum_{i\neq j=1}^{6} h_i + h_j = 2n$
		$F235_1$	$h_1h_2h_3h_4h_5h_6$: $\sum_{i\neq j=1}^{6} h_i + h_j = 2n$ $h_1h_2h_3h_4h_5h_6$: $h_1 = 5n$

The symmetry groups that serve the purpose of the structural description of quasicrystals are inherently related to the 3D space, because of the isomorphism condition. The knowledge about the structure in 3D is essential. Even though the nD approach allows restoring periodicity we cannot forget the nD embedding is just a mathematical construction and it does not directly translates to the 3D space description, even though the relationship can be found. First of all, the space $\mathbf{V}^*$ can be separated into two orthogonal subspaces, preserving the point group symmetry: $\mathbf{V}^* = \mathbf{E}^{*\parallel} \oplus \mathbf{E}^{*\perp}$, where $\mathbf{E}^{*\parallel}$ is called

a parallel space and $\mathbf{E}^{*\perp}$ is called a perpendicular space (see Fig. 3 for visualization, assuming **V** space is 2D). The parallel space is also called the external space or the physical to stress its connection with a real space. The parallel space, also called inner or phasonic space, is a space orthogonal to parallel space that extends it to restore periodicity. The real space scattering vectors are projections of the nD vectors on the parallel space. The same applies to the direct space but the projection mechanism to obtain a quasiperiodic tiling is a little more ambiguous. In general, the projection scheme for the direct space is the following. Let **V** be *a D* dimensional linear space. The structure in the d dimensional physical space $\mathbf{E}^{\parallel}$ is obtained by projecting a lattice **L** embedded in the space **V**. The lattice **L** is spanned by the D dimensional vectors $(\mathbf{a}_1, \dots, \mathbf{a}_D)$, in addition let γ_D be a unit cell of the lattice **L**. Subspace $\mathbf{E}^{\parallel} \subset \mathbf{V}$ does not contain any point of a lattice, except the origin. Let $\mathbf{S} = \mathbf{E}^{\parallel} + \gamma_D$ be an open strip in **V**, achieved by shifting γ_D along $\mathbf{E}^{\parallel}$. The union of all the $D - d$ dimensional facets, fully contained inside a strip **S** constitutes a $D - d$ dimensional surface, called the atomic surface (occupation domain, projection window), which projected onto $\mathbf{E}^{\parallel}$ creates an aperiodic tiling. The space $\mathbf{E}^{\perp}$ is an orthogonal completion of the space $\mathbf{E}^{\parallel}$. By orthogonal, the following condition is understood: if $\mathbf{e} \in \mathbf{E}^{\parallel}$ and $\mathbf{e}' \in \mathbf{E}^{\perp}$ than the inner product $\mathbf{e} \cdot \mathbf{e}' = 0$. If the aperiodic tiling is considered canonical, the projection **K** of the strip **S** onto $\mathbf{E}^{\perp}$ is the projection of γ_D. As it was stated, $\mathbf{E}^{\parallel} \cap \mathbf{L} = 0$, therefore a direct correspondence between vertices of quasiperiodic tiling and points in $\mathbf{E}^{\perp}$ exists. The projection **K** is injective, therefore each vertex of the tiling is unambiguously related to one point in the space $\mathbf{E}^{\perp}$. The condition $\mathbf{E}^{\parallel} \cap \mathbf{L} = (0)$ means the slope of the projection strip **S** is irrational. Apart from its consequence in the projection being injective, there is also another issue. Let $\mathbf{E}^{\parallel} \cap \mathbf{L} = \boldsymbol{\alpha}$, where $\boldsymbol{\alpha}$ is the arbitrary point in the superspace. For two different $\boldsymbol{\alpha}$s two different distributions of points in the parallel space will be retrieved. However, all the tilings that are projected for the parallel space at different perpendicular space position are locally isomorphic, therefore possess identical diffraction patterns. The shift in the superspace is the same as if a common global phase was ascribed to each amplitude of the structure factor. Since the diffraction intensity is proportional to the squared structure factor, the global phase cancels out. More about the local isomorphism for the icosahedral tiling is in §3. In general, the projection of the parallel space does not have to be done on the basis of the strip defined by the unit cell γ_D. In general, the shape of the atomic surface can be arbitrary, realizing a different local isomorphism. A great example is the Penrose tiling that is generated by a projection from a 5D space with the atomic surface being four pentagons. If for the same 5D space four pentagons will be replaced by five polygons: 2 pentagons and 3 decagons the General Penrose Tiling, not belonging to Penrose Local Isomorphism, can be generated [120, 121] (Fig. 4 [122]). The shape of the occupation domain is in this case defined by the section of five planes, perpendicular to the $z_\perp$ direction, through the rhombicosahedron embedded in a perpendicular space of the 5D space. If cutting planes pass through its vertices a simple Penrose Tiling is generated. However, when the section planes are shifted along the $z_\perp$ a whole class of Generalized tilings is constructed. Only

one parameter, a shift parameter distinguishes all the tilings. The shift parameter is usually given as normalized to be in the region $[0, 1)$.

The projection method, described above, is equivalent to the section method [113]. In every point of the lattice **L**, the atomic surface, embedded in the space $\mathbf{E}^{\perp}$, is located. The aperiodic tiling is constructed by points of the intersection of the parallel space $\mathbf{E}^{\parallel}$ with the atomic surface. Both methods are complementary but the section method is more intuitional to be utilized in practice. It is best explained by the following example of the nD embedding of the CdYb icosahedral quasicrystal. In Fig. 3 the section, containing 5-fold axes, through a 6D electron density map of the CdYb quasicrystal is shown (two perpendicular directions: [1000000] and [011111] define figure axes). Three occupation domains are presented: vertex-, edge- and body-centered (respectively marked *V*, *E*, and *B* in the figure). In the section method whenever parallel space $\mathbf{E}^{\parallel}$ is intersected by the occupation domain, it corresponds to an atom in the physical space. It can be specifically known which atom is generated by which occupation domain. In the projection method, the information about the origin of the atomic position is lost because all the occupation domains are basically projected onto the $\mathbf{E}^{\perp}$ forming one, big occupation domain. In addition, the information about the location of each occupation domain in the superspace is lost. It is essential to calculate the structure factor. The relative location of each occupation domain with respect to each other introduces a phase to the structure factor that does not cancel out when absolute value is taken. It is not a global phase. For these reasons, the section method is more practical, whereas the projection method is very useful to grasp a basic intuition about the nD approach.

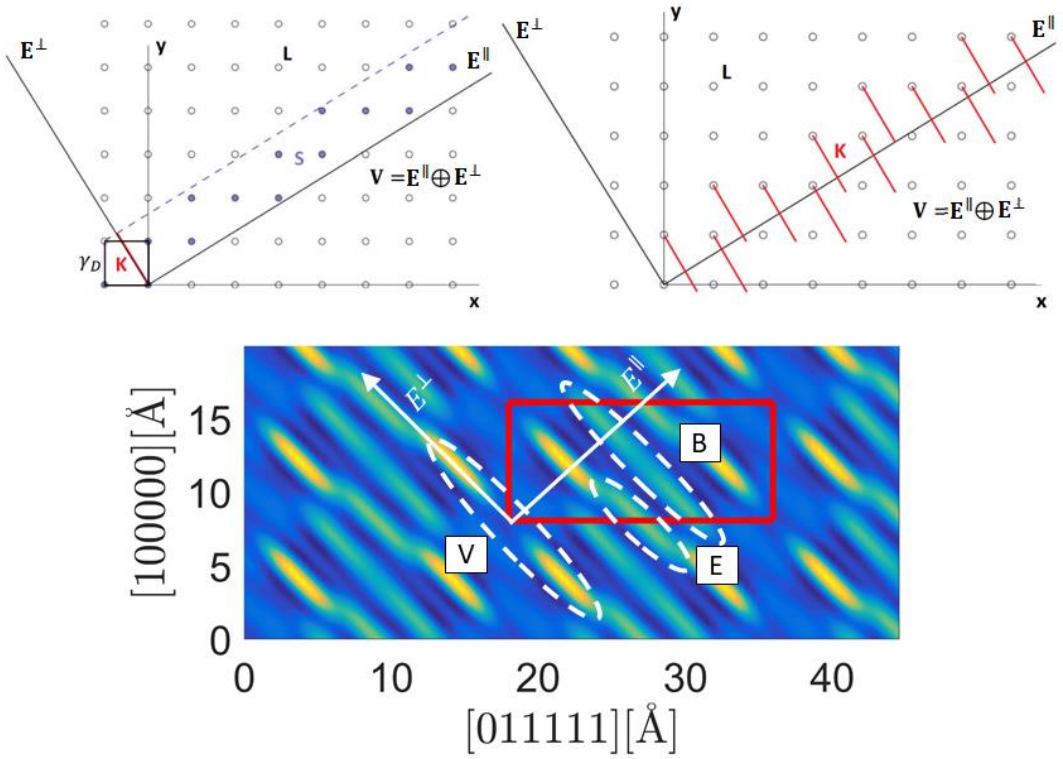

Figure 3. Top: The graphical representation of the projection method (left) and the section method (right). Details are explained in the text. Bottom: The section through the 6D electron density of the *i*-CdYb quasicrystal contaiing 5-fold directions. Three occupation domains marked *V*, *E*, and *B* are highlighted within a 6D unit cell (red rectangle).

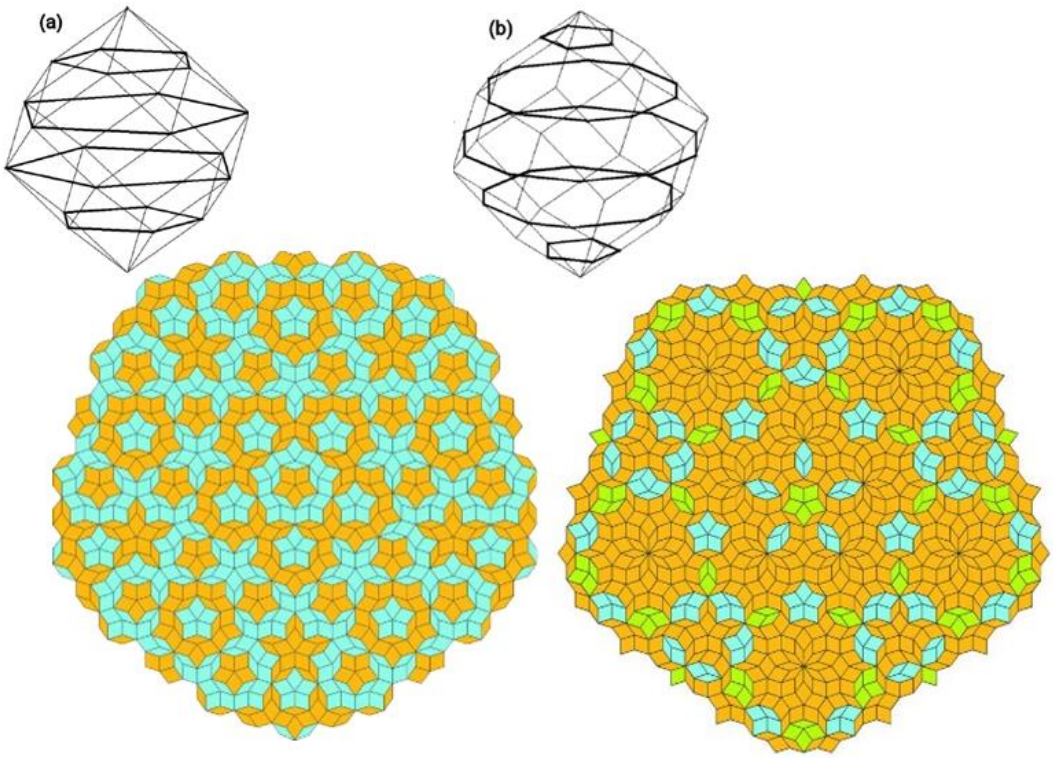

Figure 4. The General Penrose Tiling constructed for the shift parameter equal to 0, that constitutes a simple Pentose Tiling (a)) and for shift equal to 0.5 (b)). The shift parameter defines the position of the section planes through a 3D that is embedded in the perpendicular space of the decagonal quasicrystal. Source: figure based on the images found in [123, 122]

2.2 The Average Unit Cell approach

The first record of the AUC approach dates back to 1991 when Janusz Wolny in his habilitation book briefly proposed an analysis of aperiodic systems in reference to the periodic lattice that was constructed for a selected wave vector of the reciprocal space [116]. It was unfortunately only available in polish language. The first article about AUC, that appeared in an international journal, was published in 1998 [114].

The basic idea of the AUC is very different from the nD approach. The periodicity of the quasicrystal, in the higher dimensional analysis, is restored by lifting the structure to superspace, spanned by the set of basis vectors of the 3D reciprocal space, that form a $\mathbb{Z}$-module. In the AUC the periodicity is imposed by the introduction of the periodic reference lattice. The reasoning standing behind such a construction is the following. Each atom of the quasicrystal occupies a certain position in the physical space. The arrangement is ordered, even though it is incompatible with periodicity. Since it is not ordered periodically it can be enforced by overlaying the structure with a periodic lattice. In general, the vectors that the lattice is built upon do not have to be orthogonal. It is however convenient

when the orthogonal system is chosen. By considering the atomic arrangement within each consecutive unit cell it could seem like there is no pattern and atoms appear to randomly choose the position inside of the unit cell of the reference lattice. The deeper analysis brings different conclusions. On average, the distribution of atomic coordinates within the unit cell forms a pattern dependent on the geometry of the quasicrystal. The arose distribution is called the Average Unit Cell as the information about the structure is not kept in each of the unit cells of the reference lattice, but after reducing all the unit cells into one, that expresses the statistic within the structure.

Just like the occupation domain in the nD approach, the statistical distribution of the atomic coordinates is the mathematical object containing all structural information. The distribution is constructed by projecting atomic coordinated onto the periodic reference lattice, with a lattice constant λ_k related to the length k of the scattering vector $\mathbf{k}$ according to the equation $\lambda_k = 2\pi k^{-1}$. The scattering vector can be arbitrarily selected from the reciprocal space of the quasicrystal but for the distribution to be related to Bragg peaks, the scattering vector also must indicate the Bragg reflection. It is possible to analyze the diffusive component of the Fourier spectrum by choosing the scattering vector away from the Bragg peak but it will be no further discussed. The distribution constructed for the scattering vector $\mathbf{k}$ will allow calculating the structure factor for all scattering vectors equal to $n\mathbf{k}$, where $n \in \mathbb{Z}$. The coordinate u in the reference lattice of the jth atom is denoted as u_j and is calculated using the coordinate x_j:

$$u_j = x_j \bmod \lambda_k. \tag{2.1}$$

The coordinate x_j is calculated in the direct space in the direction given by the vector $\mathbf{k}$. Equation (2.1) simply says that the new coordinate u_j is the distance of the coordinate x_j from the nearest node of the reference lattice (see Fig. 5 for a visualization). The reminder given by modulo operation is exactly this distance. The important point is the coordinates of atoms must be expressed in the basis of the reciprocal space vectors chosen for the construction of the reference lattice. The easiest choice is when selected vectors are collinear with an already existing basis. The coordinates after modulo projection are limited to the region $[-\lambda_k/2, \lambda_k/2)$. Any other region is also correct as long as its length is equal to λ_k. It is similar to the position of the occupation domain in the perpendicular space. The shift of the u coordinates region is only a global phase that is insignificant during the structure factor calculations. The distribution of u_j coordinates in the u space defines the distribution $P(u)$ which gains probabilistic interpretation after the normalization. For quasicrystals, the distribution $P(u)$ is not enough to determine the structure factor. The crystal structure of quasicrystal is a two length-scale structure, therefore each vector of the reciprocal space can be represented as a sum of two vectors: the main $\mathbf{k}_0$ and the modulation vector $\mathbf{q}_0$, therefore $\mathbf{k} = n\mathbf{k}_0 + m\mathbf{q}_0, n, m \in \mathbb{Z}$. Here, the scaling ξ of the crystal structure

is best visible as $k_0/q_0 = \xi$. For icosahedral and decagonal quasicrystals $\xi = \tau = (1+\sqrt{5})/2$. The reference lattice must be constructed both for $\mathbf{k}_0$ and $\mathbf{q}_0$, which are collinear. Coordinates related to the reference lattice constructed for $\mathbf{q}_0$ are customarily denoted as v and the coordinate of the *j*th atoms is v_j. The complete information about the structure with two length-scales is stored in the two-parameter distribution $P(u,v)$. The number of required parameters is equal to the rank of the quasicrystal. In most applications there exist a mutual relation between u and v coordinates that can be expressed by a simple function. It is related to the scaling property between the main and the modulation vector. The existence of the relation $v(u)$ imposes the simplification of the statistical distribution. The distribution is non-zero in a region of the uv space that realizes the $v(u)$ relation which is a set of curves or a single curve in the simplest case. Therefore the distribution $P(u,v)$ can be replaced by the marginal distribution $P(u)$ only with the addition of the scaling relation $v(u)$. What is referred to as the AUC in the statistical description is exactly the marginal distribution. To show the basic idea of the structure factor calculation in the AUC method let's consider a 1D example. Let $\mathbf{k} = n\mathbf{k}_0 + m\mathbf{q}_0, n, m \in \mathbb{Z}$. Since $\mathbf{k}_0$ and $\mathbf{q}_0$ are collinear vectors the notation can be replaced by norms of the vectors: $k = nk_0 + mq_0$. The structure factor formula is:

$$F(nk_0 + mq_0) = \sum_{j=1}^{N} f_j(k) \exp(i(nk_0 + mq_0)\, x_j), \tag{2.2}$$

where $f_j(k)$ is the atomic scattering factor of *j*th atom and *N* is the number of atoms. By using formula (2.1) for the reference lattice with a lattice constant λ_{k0} associated with the vector $\mathbf{k}_0$ and the reference lattice with a lattice constant λ_{q0} linked to the vector $\mathbf{q}_0$ equation (2.2) can be modified. First of all, the coordinate x_j must be derived from (2.1), where x_j is pulled from the equation:

$$x_j = l\lambda_{k0} + u_j, \qquad x_j = p\lambda_{q0} + v_j, \qquad l, p \in \mathbb{Z}. \tag{2.3}$$

The (2.3) cane by used to substitute x_j in a formula (2.2), keeping in mind that $k_0 = 2\pi/\lambda_{k0}$ and $q_0 = 2\pi/q_{k0}$:

$$\begin{aligned} F(nk_0 + mq_0) &= \sum_{j=1}^{N} f_j(k) \exp\left(i\frac{2\pi}{\lambda_{k0}} n(l\lambda_{k0} + u_j) + i\frac{2\pi}{\lambda_{q0}} m(p\lambda_{q0} + v_j) \right). \\ &= \sum_{j=1}^{N} f_j(k) \exp(ink_0u_j + imq_0v_j)). \end{aligned} \tag{2.4}$$

If the number of atoms is large, the summation can be replaced by integration in the region of the AUC for a specific type of atom. If there are g types of atom, than:

$$F(nk_0 + mq_0) = \sum_g f_g(k) \int_{AUC} P(u)_g \exp(ink_0 u + imq_0 v(u)) \tag{2.5}$$

where $P(u)_g$ is the distribution of the g atom. If there is only one atom type in terms of the scattering form factor, then

$$F(nk_0 + mq_0) = f(k) \int_{AUC} P(u) \exp\big(ink_0 u + imq_0 v(u)\big) \mathrm{d}u\,. \tag{2.6}$$

In further formulas I will assume $f(k) = 1$ as it does not change general conclusions. According to formula (2.6), a whole Fourier spectrum can be obtained by the Fourier Transform of the distribution $P(u)$, assuming relation $v(u)$. For icosahedral quasicrystal the $v(u) = -\tau^2 u$ for each reciprocal space vector necessary to obtain a complete statistical distribution. The statistical distribution of the icosahedral quasicrystal is $P(\mathbf{u},\ \mathbf{v})$, where $\mathbf{u} = [u_x, u_y, u_z]$ and $\mathbf{v} = [v_x, v_y, v_z]$, therefore three main and three modulation vectors are needed.

If the linear scaling relation $v(u) = -\tau^2 u$ is used in (2.6), then

$$\begin{aligned} F(nk_0 + mq_0) &= \int_{AUC} P(u) \exp(ink_0 u - imq_0 \tau^2 u) \mathrm{d}u \\ &= \int_{AUC} P(u) \exp(ik_0 (n - \tau m) u) \mathrm{d}u = \int_{AUC} P(u) \exp(iwu) \mathrm{d}u \\ &= F(w) \end{aligned} \tag{2.7}$$

Formula (2.7) shows that (n, m) the Fourier mode of the structure can be calculated as the Fourier Transform of the distribution $P(u)$ for the vector $w = k_0(n - \tau m)$. The vector w is called a reduced vector and is used to plot the so-called envelope function (Fig. 5). The distribution $P(u)$ is a dense, uniform distribution for quasicrystalline tilings, therefore its Fourier Transform has a shape of the sine cardinal function. All the peaks from the diffraction pattern can be collapsed to this envelope function in the same way as all the atoms of the structure can be collapsed to one AUC. The envelope

function is very useful to show the effect of disorder on the diffraction pattern in quasicrystals or even to find the phases of the experimental diffraction peaks.

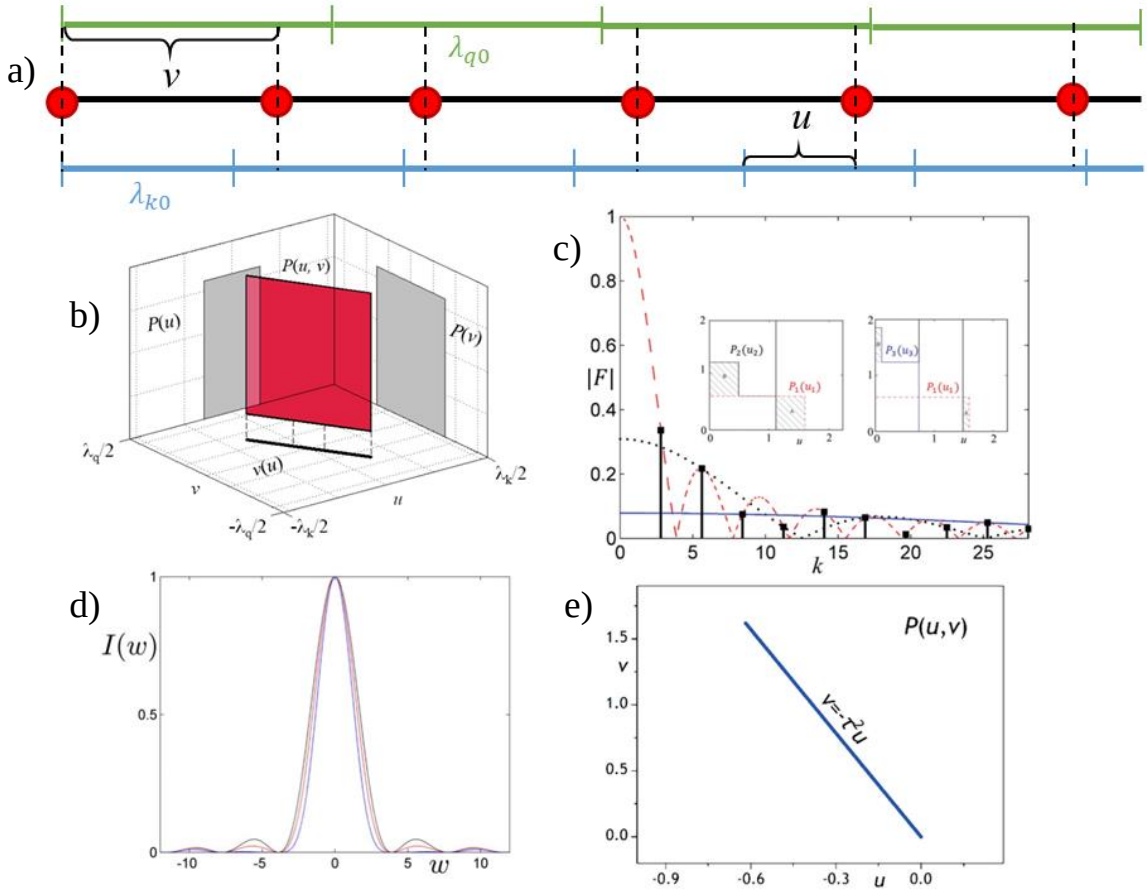

Figure 5. a): The visualization of the projection scheme of the atomic coordinates onto the periodic reference lattice. Two lattices: one corresponding to vector $\mathbf{k}_0$ and the second to $\mathbf{k} = \mathbf{q}_0$ are shown; b) The $P(u, v)$ distribution of the 1D quasicrystals. It is a uniform distribution along a straight line in a uv space. Marginal distributions $P(u)$ and $P(v)$ are also plotted; c) The envelopes plotted upon the diffraction peaks. It can be seen that the envelope is generated by only the part of the distribution that does not touches the boundaries of the reference lattice; d) the envelope function of the uniform distribution – sine cardinal function. The intensity varies with the introduciton of the phason disorder, therefore the shape of the envelope function can be used to distinguis strucutres with different magnitude of disorder; e) the $v(u)$ relation frequently encountered in quasicrystals with a frobidden symmetry.

The AUC approach was used to find the structure factor of simple 1D quasicrystal [124], modulated structure [29], the Penrose tiling [125] and also the Ammann-Kramer-Neri tiling [126]. Several decagonal quasicrystals were solved based on the AUC approach by assigning the atomic decoration to rhombuses constituting the aperiodic tiling [127, 82]. In addition, thanks to the

probabilistic interpretation of the distribution function in the AUC, the new approach to the phason disorder was developed, assuming a statistical character of phason rearrangement in the tiling [128, 129, 130]. The statistical analysis of quasicrystals is a powerful tool that requires more attention.

2.3 The Correspondence between the AUC and the *n*D approach

The nD approach is the most frequently used method to construct the model of the quasicrystal. The role of an atom in this approach is played by the occupation domain – a multidimensional object that is extended in the perpendicular space. In the physical space, it is represented by a single point. This point becomes an atom in the projected structure if the occupation domain crosses the parallel space. Due to the finite resolution of the experiment, the occupation domain in the section through the electron density map shows some smearing along the parallel space. The occupation domain can be, in general, placed in any position within the unit cell of the nD periodic lattice. As a consequence, similarly to periodic structures, apart from a primitive lattice also face-centered and body-centered lattices are possible, even though only a primitive and face centered are experimentally proven.

It can be shown that the AUC is an oblique projection of the atomic surface onto the physical space. For that reason, the occupation domain acquires a physical interpretation, which states that the occupation domain is a probability distribution $P(u)$ lifted up to higher dimensions. As long as the multidimensional superspace exists for a given system, the two approaches are equivalent. This is true, for instance for model structures like the Penrose tiling or Fibonacci chain. On the other hand, there are numerous systems where multidimensional analysis cannot be used, however the AUC still can be constructed. The simple case is a structure disordered by phonons or a Thus-Morse sequence with a singular-continuous Fourier Spectrum. The higher dimensional approach works only for the Bragg peaks and sinc the Thus-Morse sequence does not have them, it cannot be utilized [131]. The AUC can be constructed for an arbitrary scattering vector, therefore the method does not cease to be applied.

The proof that the AUC is a projection of the occupation domain is simple and now will be carried out for a 1D structure with a τ scaling, which is lifted to 2D superspace. The following relation is true:

$$G \cdot r = k_{\parallel} x_{\parallel} + k_{\perp} x_{\perp} = 0, \qquad (2.8)$$

where $G = [k_{\parallel}, k_{\perp}]$ and $r = [x_{\parallel}, x_{\perp}]$. The relation (2.8) uses the orthogonality condition between vectors of the direct and reciprocal space. Let's now expand the parallel components of equation (2.8) using formula (2.1) and in the same time $k_{\parallel} = nk_{0\parallel} + mq_{0\parallel}$, $k_{\perp} = nk_{0\perp} + mq_{0\perp}$:

$$k_{\parallel}x_{\parallel} = nk_{0\parallel}(l\lambda_{k0\parallel} + u) + mq_{0\parallel}(l\lambda_{q0\parallel} + v). \tag{2.9}$$

Let's use the relation between the lattice constant and the length of the scattering vector:

$$k_{\parallel}x_{\parallel} = nk_{0\parallel}u + mq_{0\parallel}v. \tag{2.10}$$

Any component of (2.10) that gave the integer multiplicity of 2π was removed as it is irrelevant when it comes to the structure factor calculation (i.e. it does not change the exponent). Let's substitute (2.8) with (2.10) and group components with respect to the peak index:

$$\begin{aligned} nk_{0\parallel}u + mq_{0\parallel}v + nk_{0\perp}x_{\perp} + mq_{0\perp}x_{\perp} \\ = n(k_{0\parallel}u + k_{0\perp}x_{\perp}) + m(q_{0\parallel}v + q_{0\perp}x_{\perp}) = 0. \end{aligned} \tag{2.11}$$

The relation (2.11) must be true for all the indices, therefore each bracket must be equal to 0:

$$\begin{aligned} k_{0\parallel}u + k_{0\perp}x_{\perp} = 0 \rightarrow u = -\frac{k_{0\perp}}{k_{0\parallel}}x_{\perp}, \\ q_{0\parallel}v + q_{0\perp}x_{\perp} \rightarrow v = -\frac{q_{0\perp}}{q_{0\parallel}}x_{\perp}. \end{aligned} \tag{2.12}$$

From (2.12) it is evident, that coordinates in the AUC approach are proportional to corresponding coordinates in the nD (see Fig. 6 [132]). The proportionality coefficients $\frac{k_{0\perp}}{k_{0\parallel}}$ and $\frac{q_{0\perp}}{q_{0\parallel}}$ define a slope of the line along which the projection of the perpendicular coordinate onto the physical space is performed. The value of the coefficient is not unique and depends on the scattering vector chosen for the construction of the reference lattice. As a consequence, even though the shape of the occupation domain is uniquely determined for a particular structure, there exists an infinite family of probability distributions associated with the structure.

Equation (2.12) can be also used to prove the scaling relation $v(u) = -\tau^2 u$. The proof starts by combining equations (2.12) for u and v by deriving $x_{\perp}$:

$$v = \frac{k_{0\parallel}}{k_{0\perp}}\frac{q_{0\perp}}{q_{0\parallel}}u. \tag{2.13}$$

It was already stated that the scaling between the main vector and the modulation vector is equal to τ, therefore $k_{0\parallel}/q_{0\parallel} = \tau$. Now we have to derive $q_{0\perp}/k_{0\perp}$. It is done as follows. The reciprocal space vector G is equal to:

$$G = \begin{pmatrix} k_{\parallel} \\ k_{\perp} \end{pmatrix} = \overbrace{\begin{pmatrix} k_{0\parallel} & q_{0\parallel} \\ k_{0\perp} & q_{0\perp} \end{pmatrix}}^{\mathbf{G}_{\mathrm{m}}} \begin{pmatrix} n \\ m \end{pmatrix}. \qquad (2.14)$$

There are two row vectors in the projection matrix $\mathbf{G}_{\mathrm{m}}$: $(k_{0\parallel}, q_{0\parallel})$ and $(k_{0\perp}, q_{0\perp})$. Since they scan the reciprocal space their inner product must be equal to 0 (for orthogonal basis):

$$(k_{0\parallel}, q_{0\parallel}) \cdot (k_{0\perp}, q_{0\perp}) = k_{0\parallel}k_{0\perp} + g_{0\parallel}q_{0\perp} = 0 \rightarrow \frac{k_{0\parallel}}{g_{0\parallel}} = -\frac{q_{0\perp}}{k_{0\perp}} = \tau. \qquad (2.15)$$

By substituting (2.15) to (2.13):

$$v = -\tau^2 u. \qquad (2.16)$$

Equation (2.16) expresses the scaling relation $v(u)$ used in equation (2.7). That concludes the proof.

The equivalence of the AUC and the nD approach creates a possibility to exploit the best properties of each approach at the same time [133]. The AUC approach is not useful to construct the aperiodic tiling since it is constructed for an already existing structure. However, it provides a necessary interpretation of the occupation domain in the context of the physical space, namely it represents a probability of finding atoms in a specific environment. The probabilistic interpretation of the occupation domain helps to analyze the statistic of the structure, which is the only feature derived in the diffraction experiment and the study based on the Bragg peaks. After the aperiodic tiling is generated with the direct projection method from the superspace, the obtained positions in the physical space do not need to be additionally projected onto the reference lattice of the AUC to carry out the statistical analysis. The occupation domain, as equivalent to the distribution function, can be used without losing any necessary information.

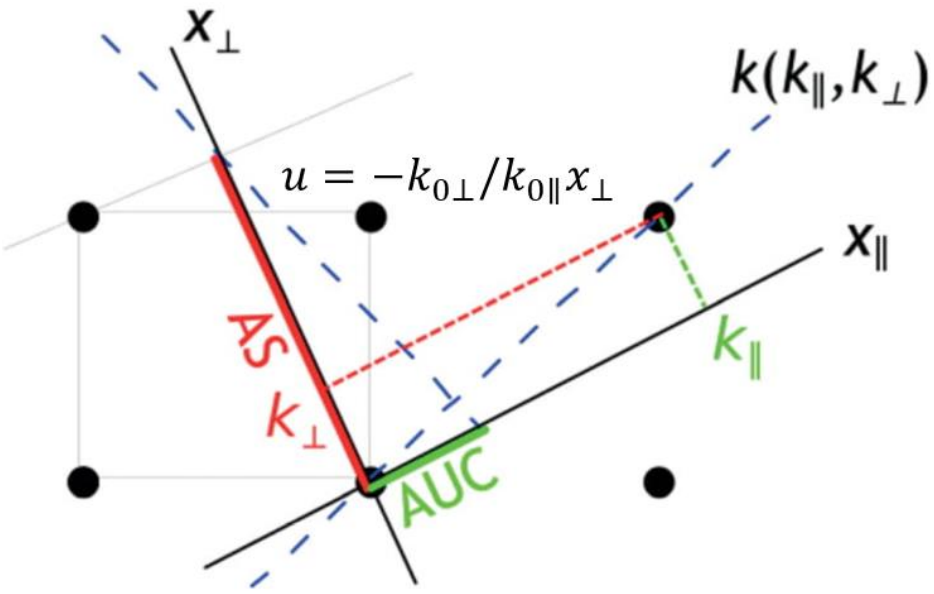

Figure 6. The relation between the occupation domain (atomic surface, denoted as AS) and the AUC. The AUC can be considered as a projection of the AS onto the physical space. The projection is defined by the choice of the reciprocal space vector for which the reference lattice is construcuted. The figure clearly shows the relations between u and $x_\perp$ coordinates. Source: [132]

3. The Ammann-Kramer-Neri tiling

Currently, only one 3D tiling is used as a quasilattice for the icosahedral quasicrystal. The tiling is frequently called a 3D Penrose tiling, even though Sir Roger Penrose was not involved in its construction nor study. It is due to their similarities: both manifest the same τ scaling, where τ is a golden mean ratio; both are built of two units, geometrically very similar and finally, the section through the 3D Penrose tiling, perpendicular to 5-fold axis, gives the Penrose tiling. The 3D Penrose tiling is also called Ammann tiling or nowadays Ammann-Kramer-Neri tiling (AKNt), which is a name adapted for the thesis, to honor original researchers involved in the studies of the tiling [106]. Among tilings with icosahedral symmetry, there is also a so-called Socolar-Steinhardt tiling [134] that originally was shown to be generated by the generalized dual method [135] that is related with a grid projection method by de Bruijin [136]. Recently a recursive growth procedure based on the inflation rules that were used to construct quasiperiodic tiling from the very beginning [20], was proposed [137], that allows calculating the structure factor [138]. That makes it a valid alternative for the superspace approach. However, now the Socolar-Steinhardt tiling is not explored as a quasilattice for icosahedral structures explicitly, as standard methods are enough successful.

The AKNt is composed of two kinds of prototiles: a prolate and an oblate rhombohedron with equal edge length a_r (Fig. 7). The faces of rhombohedra have the shape of a rhombus with an acute angle $\theta = \mathrm{atan}(2) = 63.44°$. The volumes of both units (V_p for prolate and V_o for oblate) are: $V_p = \frac{4}{5}a_r^3 \sin\frac{2\pi}{5}$ and $V_o = \frac{4}{5}a_r^3 \sin\frac{\pi}{5}$. The ratio between the volumes $V_p/V_o = \tau$. As it was already mentioned, $\tau = \left(1+\sqrt{5}\right)/2$ is equal to the golden mean ratio, being a characteristic scaling for decagonal and icosahedral quasicrystals. Some 1D aperiodic structures are classified as quasicrystals instead of modulated structures just because they exhibit τ scaling. It signifies the importance of the scaling in the structural analysis. Another important property, associated with scaling, is the relative frequency of each unit to appear in the tiling. The prolate-to-oblate rhombohedron ratio is also equal to τ. As a consequence, the point density D_p, which is equal to number of vertices (atoms) in the tiling divided by the volume is equal to $D_p = \frac{\tau+1}{\tau V_p + V_o} = \frac{\tau}{a_r^3}\sin\frac{2\pi}{5}$. The point density is used in the structure analysis as a space-filling parameter that indicates whether some atoms are missing in the structure model.

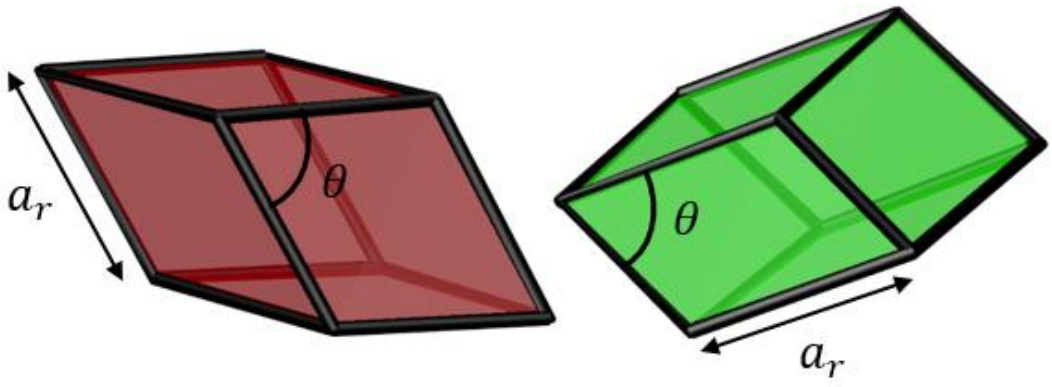

Figure 7. Two units of the AKNt: prolate (red) and oblate (green) rhombihedron.

In order to construct any aperiodic tiling, the rule of assembling units must be known. Such rules are called matching rules and indicate the most favorable local configurations. There is a rule of connecting to rhombohedra, discovered by Robert Ammann [22]. However, the rules are known to be at least weak matching rules that enforce a quasicrystalline order [139]. Whether they are perfect matching rules, i.e. enforce a single local isomorphism class, is still not rigorously proven, even though they can be used in force growth of the perfectly ordered icosahedral quasicrystal when seeded with a cluster [140].

The question of a local isomorphism has both a mathematical and a physical significance. The quasicrystal packings belonging to two different local isomorphism classes have a different local arrangement of unit tiles. Structures obtained as a decoration of the unit tiles will have different local atomic environment. In addition, two tilings belonging to different local isomorphism class can have diffraction peaks in the same positions of the reciprocal space but different intensities. Last but not least, they differ by the free-energy. Since the entropy of the quasicrystal depends on the number of units rearrangements it must be counted in the same local isomorphism. Two tilings are locally isomorphic if any finite region in either tiling exists somewhere in the other.

The perfect matching rules are proven for the Socolar-Steinhardt tiling, associated with Ammann tilings, built of four zonohedra and not two rhombohedra. Those four zonohedra are: rhombic triacontahedron, rhombic icosahedron, rhombic dodecahedron and prolate rhombohedra (Fig. 8). Each shape comes from ascribing a unit cell to each singularity type occurring in a Fibonacci hexagrid obtained by a grid-projection method. Each plane of the hexagrid is defined by the equation $\mathbf{re}_n = N + \alpha_n + 1/\tau\lfloor N/\tau + \beta_n \rfloor$, where $\mathbf{e}_n$ are vectors of the icosahedral setting and $\alpha_n = \frac{1}{\tau}, \beta_n = -1/2, N \epsilon \mathbb{Z}$. The singular point of the hexagrid is a point where more than three planes intersect. The cell dual to a singularity is composed of vertices that are generated by points dual to open regions in a grid space, that surrounds the singularity. In a hexagrid there exist a sixfold singularity. The dual shape is exactly a

rhombic triacontahedron. A rhombic icosahedron is related to a fivefold singularity, whereas a rhombic dodecahedron comes from a dual to a fourfold singularity. The prolate rhombohedra are generated by non-singular intersections. The infinite tiling of zonohedra can be constructed by assembling units along hexagrid planes, called Ammann planes in the context of the Ammann tiling, or by decomposition rules (inflation/deflation rules). The decoration of each zonohedron by Ammann planes is simple, i.e. there exists only one, unique decoration. The matching rules for zonohedra come from the demand that two neighboring units match face to face and the planes that decorate each zonohedron continue along the same plane across the interface.

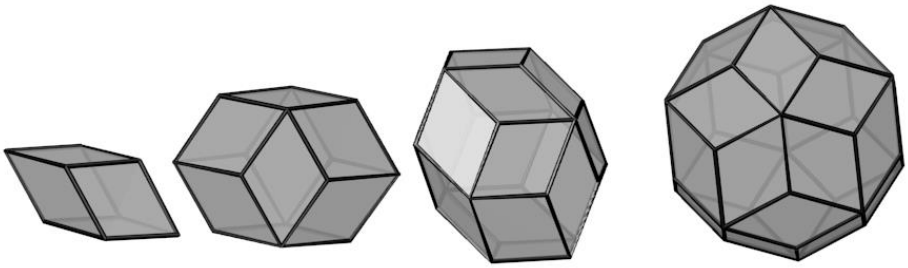

Figure 8. Four zonohedra in the Socolar-Steinhardt tiling. From left: prolate rhombohedron, rhombic dodecahedron, rhombic icosahedron and rhombic triacontahedron.

The tiling with zonohedra as units do not have an oblate rhombohedron among them. However, each zonohedron is a polyhedron that can be decomposed into fundamental rhombohedra: prolate and oblate. Rhombic triacontahedron is built out of 10 oblate and 10 prolate rhombohedra, rhombic icosahedron out of 5 prolate and 5 oblate rhombohedra and finally rhombic dodecahedron require two units of each type. Such a decomposed tiling can be obtained by a projection method. The Ammann plane decoration of zonohedra can be viewed therefore as a decoration of oblate and prolate rhombohedra. There is one problem with finding such a decoration. For instance, two prolate rhombohedra, depending on a local environment can be decorated in a different way by Ammann planes, therefore there is no one, single rule of decomposing rhombohedra or assembling them into the infinite tiling. It is directly connected to the decomposition of the zonohedra into rhombohedra. Namely, the decomposition can be done in numerous ways. Let's consider a rhombic dodecahedron, that is generated by the fourfold singularity. It can be decomposed into two prolate and two oblate rhombohedra. At the same time, rhombic dodecahedron is the basic geometry that produces a phason flip site. Phason flip is a shift of one site, that changes the inner pattern of the geometry but leaves the exterior intact. In Fig. 9 the position *A* can be shifted to the position *A*'. Even though the faces of the rhombic dodecahedron stay intact the interior arrangement of rhombohedra is an inversion of original with respect to the geometric center of the rhombic dodecahedron. Therefore the decomposition of it can be done in two ways, that brake local order. It is known that phason flip changes the intensities of the diffraction pattern, therefore

the zonohedra tiling can, in general, be decomposed into tilings that can be distinguished by their diffraction pattern. The Socolar-Steinhardt tiling, even though belongs to the class of Ammann tilings is not locally isomorphic to the tiling obtained by the projection method.

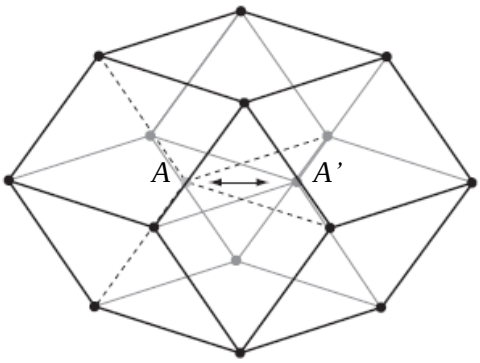

Figure 9. The rhombic dodecahedron that constitutes a basic phason flip geometry in the icosahedral lattice. The flip of the postion *A* to position *A'* leaves the outer shape intact but changes an inner configuration of the rhombohedra.

3.1 The reciprocal and direct space of the icosahedral quasicrystal

The AKNt is a tiling with icosahedral symmetry therefore, it can serve as a quasilattice for the structure solution of the icosahedral quasicrystal. The diffraction pattern of the icosahedral quasicrystal can be indexed with a sextet of integers, therefore each diffraction vector $\mathbf{G} = \sum_{i=1}^{6} h_i \mathbf{a}_i^*$, $h_i \in \mathbb{Z}$ and $\mathbf{a}_i^*$ are the vectors in a 3D reciprocal space that form a $\mathbb{Z}$-module. There are several indexing schemes in use, therefore one has to keep in mind the used indices can refer to different indexation schemes.

Elser's indexation scheme is among the most popular [112]. In this setting the reciprocal basis vectors $\mathbf{a}_i^*$ are directed from the center toward the vertices of icosahedron:

$$\begin{gathered} \mathbf{a}_1^* = a^*(0 \quad 0 \quad 1), \\ \mathbf{a}_i^* = a^*(\sin(\theta)\cos(2\pi i/5) \quad \sin(\theta)\sin(2\pi i/5) \quad \cos(\theta)), \\ i = 2, \dots, 6, \end{gathered} \tag{3.1}$$

with $\tan\theta = 2$, where θ is the angle between two adjacent axes, $a^* = |\mathbf{a}_i^*|$. Vectors $\mathbf{a}_i^*$ can be considered parallel space projections of the basis vectors $\mathbf{d}_i^*$ of the 6D reciprocal space $\mathbf{V}^*$:

$$\mathbf{d}_1^* = 2\pi a^* \begin{pmatrix} 0 \\ 0 \\ 1 \\ 0 \\ 0 \\ 1 \end{pmatrix},\ \mathbf{d}_i^* = 2\pi a^* \begin{pmatrix} s\theta\cos(2\pi i/5) \\ s\theta\sin(2\pi i/5) \\ 1 \\ -s\theta\cos(4\pi i/5) \\ -s\theta\sin(2\pi i/5) \\ -c\theta \end{pmatrix}, i = 2, \dots, 6, \tag{3.2}$$

where $s\theta \equiv \sin\theta$ and $c\theta \equiv \cos\theta$. Each vector $\mathbf{d}_i^*$ has parallel and perpendicular space components: $\mathbf{d}_i^* = \left(\mathbf{a}_i^{*\parallel},\ \mathbf{a}_i^{*\perp}\right)$. Here $\mathbf{a}_i^{*\parallel} \equiv \mathbf{a}_i^*$; the '$\parallel$' was written to emphasize that the first three coordinates of the vector $\mathbf{d}_i^*$ always represent the parallel space components of the 6D vector and three last elements belong to the perpendicular space. It is also valid for the direct space notation. The direct 6D basis can be obtained as a result of the orthogonality condition:

$$\mathbf{d}_1 = a_r \begin{pmatrix} 0 \\ 0 \\ 1 \\ 0 \\ 0 \\ 1 \end{pmatrix},\ \mathbf{d}_i = a_r \begin{pmatrix} s\theta\cos(2\pi i/5) \\ s\theta\sin(2\pi i/5) \\ 1 \\ -s\theta\cos(4\pi i/5) \\ -s\theta\sin(2\pi i/5) \\ -c\theta \end{pmatrix}, i = 2, \dots, 6, \tag{3.3}$$

where $a_r = \frac{1}{2a^*}$ is the length of the edge of the rhombohedral unit. The direct and reciprocal lattice parameters are:

$$\begin{aligned} |\,\mathbf{d}_i^*| &= a^*\sqrt{2}, \alpha_{ij} = 90°, i, j = 1, \dots, 6 \\ |\,\mathbf{d}_i| &= a^*\sqrt{2}, \alpha_{ij} = 90°, i, j = 1, \dots, 6 \end{aligned} \tag{3.4}$$

The angle α_{ij} between each of two basis vectors of the direct and the reciprocal space is equal to 90° therefore the 6D unit cell is a hypercube. The volume of the hypercube is:

$$V = a_{6D}^6 = |\,\mathbf{d}_i|^6 = \left(\frac{1}{a^*\sqrt{2}}\right)^6 = \left(a_r\sqrt{2}\right)^6, \tag{3.5}$$

where a_{6D} is a lattice constant of the 6D lattice. It is evident that $a_{6D} = a_r\sqrt{2}$.

Alternatively, there exists another common setting of the reciprocal basis [108]. The same six-star of reciprocal basis vectors is used, however in a different orientation. It is a Cartesian coordinate system oriented along twofold axes of the icosahedron:

$$\mathbf{W}_p^* = \frac{2\pi a^*}{\sqrt{\tau+2}}\begin{pmatrix} 1 & \tau & \tau & 0 & -1 & 0 \\ \tau & 0 & 0 & 1 & \tau & 1 \\ 0 & 1 & -1 & -\tau & 0 & \tau \\ \tau & -1 & -1 & 0 & -\tau & 0 \\ -1 & 0 & 0 & \tau & -1 & \tau \\ 0 & \tau & -\tau & 1 & 0 & -1 \end{pmatrix}, \tag{3.6}$$

where each column of the matrix $\mathbf{W}_p^*$ represents one vector $\mathbf{d}_i^*$ expressed in the coordinate system oriented along twofold axes. It must be stated once more, that the indices used in this setting are exactly the same as in the former setting; only the orientation of the coordinate system has changed. The projection matrix $\boldsymbol{M}$ between those two coordinates system is the following:

$$\boldsymbol{M} = \begin{pmatrix} \cos\pi/10 & \sin\pi/10 & 0 \\ -\cos\theta/2\sin\pi/10 & \cos\theta/2\cos\pi/10 & \sin\theta/2 \\ \sin\theta/2\sin\pi/10 & -\sin\theta/2\cos\pi/10 & \cos\theta/2 \end{pmatrix}, \tag{3.7}$$

where the column vector must be multiplied from the right side of the matrix $\boldsymbol{M}$ to obtain the coordinates of the vector in the new setting.

Another indexation scheme is based on a cubic basis, according to Cahn's basis [141]. In this scheme not only the coordinate system is chosen along twofold axes but also the basis vectors do not point toward the corners of icosahedron but are collinear with the twofold axes. Let's call new vectors $\mathbf{f}_i^*$. They can be constructed as a linear combination of vectors $\mathbf{d}_i^*$:

$$\begin{pmatrix} \mathbf{f}_1^* \\ \mathbf{f}_2^* \\ \mathbf{f}_3^* \\ \mathbf{f}_4^* \\ \mathbf{f}_5^* \\ \mathbf{f}_6^* \end{pmatrix} = \frac{1}{2}\begin{pmatrix} 0 & \bar{1} & 0 & 0 & 0 & 1 \\ 0 & 0 & \bar{1} & 0 & 1 & 0 \\ 1 & 0 & 0 & \bar{1} & 0 & 0 \\ 0 & 1 & 0 & 0 & 0 & 1 \\ 0 & 0 & 1 & 0 & 1 & 0 \\ 1 & 0 & 0 & 1 & 0 & 0 \end{pmatrix}\begin{pmatrix} \mathbf{d}_1^* \\ \mathbf{d}_2^* \\ \mathbf{d}_3^* \\ \mathbf{d}_4^* \\ \mathbf{d}_5^* \\ \mathbf{d}_6^* \end{pmatrix}. \tag{3.8}$$

The same transformation applies to the indices in both settings:

$$\begin{pmatrix} h \\ h' \\ k \\ k' \\ l \\ l' \end{pmatrix} = \frac{1}{2}\begin{pmatrix} 0 & \bar{1} & 0 & 0 & 0 & 1 \\ 0 & 0 & \bar{1} & 0 & 1 & 0 \\ 1 & 0 & 0 & \bar{1} & 0 & 0 \\ 0 & 1 & 0 & 0 & 0 & 1 \\ 0 & 0 & 1 & 0 & 1 & 0 \\ 1 & 0 & 0 & 1 & 0 & 0 \end{pmatrix}\begin{pmatrix} h_1 \\ h_2 \\ h_3 \\ h_4 \\ h_5 \\ h_6 \end{pmatrix}, \tag{3.9}$$

where primed index refers to τ larger vector, when projected onto the parallel space.

3.2 The projection method for the AKNt

The AKNt is a so-called canonical tiling, generated by a canonical projection from a 6D space. Every tiling for which the occupation domain is a projection of the 6D unit cell is called canonical. It should not be confused with canonical cells that are used to express the atomic arrangement in periodic approximants of the quascirystals [142].

The 6D unit cell has 64 vertices, among which 32 constitute the vertices of the occupation domain and the rest are contained within the occupation domain. The shape of the occupation domain of the AKNt is a rhombic triacontahedron, manifesting full icosahedral point symmetry, with an edge-length equal to the edge-length of the rhombohedral unit. The nodes of the AKNt can be found by projecting 6D lattice points onto the perpendicular space with the use of the projection matrix **W** built of columnar vectors $\mathbf{d}_i$:

$$\mathbf{W} = a_r \begin{pmatrix} 0 & s\theta\cos\frac{4\pi}{5} & s\theta\cos\frac{6\pi}{5} & s\theta\cos\frac{8\pi}{5} & s\theta & s\theta\cos\frac{2\pi}{5} \\ 0 & s\theta\sin\frac{4\pi}{5} & s\theta\sin\frac{6\pi}{5} & s\theta\sin\frac{8\pi}{5} & 0 & s\theta\sin\frac{2\pi}{5} \\ 1 & c\theta & c\theta & c\theta & c\theta & c\theta \\ 0 & -s\theta\cos\frac{8\pi}{5} & -s\theta\cos\frac{2\pi}{5} & -s\theta\cos\frac{6\pi}{5} & -s\theta & -s\theta\cos\frac{4\pi}{5} \\ 0 & -s\theta\sin\frac{8\pi}{5} & -s\theta\sin\frac{2\pi}{5} & -s\theta\sin\frac{6\pi}{5} & 0 & -s\theta\sin\frac{4\pi}{5} \\ 1 & -c\theta & -c\theta & -c\theta & -c\theta & -c\theta \end{pmatrix}. \tag{3.10}$$

The point $\mathbf{r}_\mathrm{L}$ of the 6D lattice **L**, projected via matrix **W** has coordinates:

$$\begin{gathered} \mathbf{r}_\mathrm{V} = \mathbf{W} \cdot \mathbf{r}_\mathrm{L}, \\ \mathbf{r}_\mathrm{V} = (\boldsymbol{x}_\parallel, \boldsymbol{y}_\parallel, \boldsymbol{z}_\parallel, \boldsymbol{x}_\perp, \boldsymbol{y}_\perp, \boldsymbol{z}_\perp), \\ \mathbf{r}_\mathrm{L} = \sum_{i=1}^{6} \alpha_i \mathbf{e}_i \,, \alpha_i \in \mathbb{Z}, \end{gathered} \tag{3.11}$$

where $\mathbf{e}_i$- vector with an *i*th element equal to 1 and the rest elements equal to 0.

If the perpendicular space coordinates of the projected point (indicated with a subscript '⊥') are contained within the rhombic triacontahedron, its projection onto the parallel space corresponds to the node of the AKNt (Fig. 10). If the projected point is not part of the rhombic triacontahedron, it is rejected from further calculations. In order to check whether a point belongs to the volume defined by the rhombic triacontahedron, the following condition must be satisfied. If **n** is a normal to the face of

rhombic triacontahedron and $\mathbf{r}_V^{\perp}$ is a projection of the point $\mathbf{r}_L$ onto the perpendicular space, then point $\mathbf{r}_V^{\perp}$ belongs in the occupation domain if

$$\begin{aligned} \mathbf{n} \cdot \left(\mathbf{r}_V^{\perp} - \mathbf{r}_p\right) \leq 0, \\ \mathbf{r}_p = \mathbf{r}_V^{\perp} - \mathbf{n} \cdot \left(\mathbf{n} \cdot (\mathbf{r}_V^{\perp} - \mathbf{r})\right), \end{aligned} \tag{3.12}$$

where $\mathbf{r}$ is an arbitrary point belonging to the face of rhombohedron and $\mathbf{r}_p$ is a point of the projection of $\mathbf{r}_V^{\perp}$ onto the face of rhombohedron. The condition (3.12) must be valid for every face of the rhombic triacontahedron. From the point of view of numerical calculations, there can be a problem of a calculation precision for the points belonging to the surface of the triacontahedra. It is better to make an inequality condition stronger to avoid points that are incorrectly assigned as belonging to AKNt.

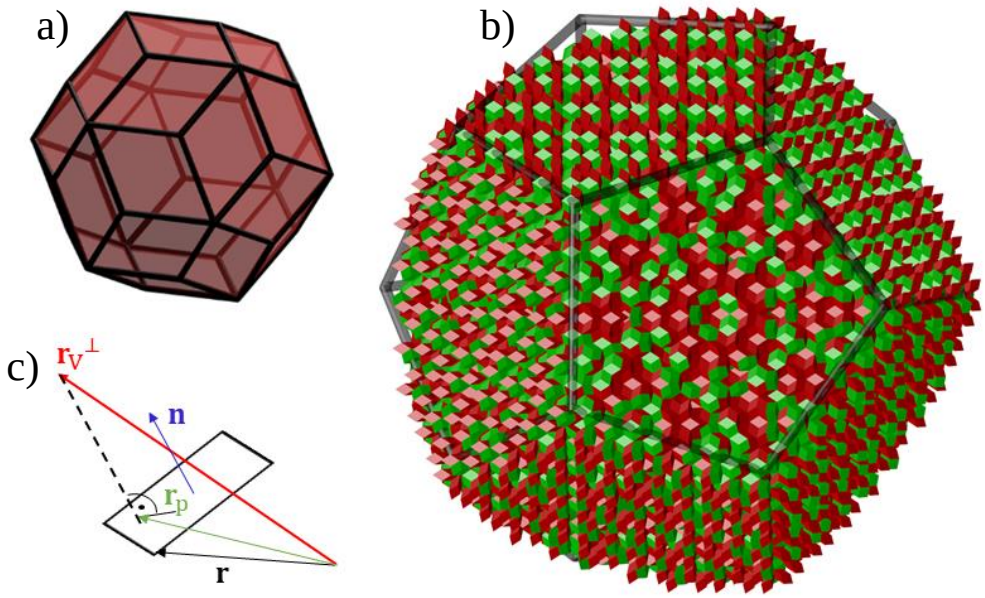

Figure 10. a) The rhombic triacontahedron as a projection window for the AKNt; b) The generated AKNt with the prolate (red) and oblate (green) rhombohedra distinguished. The outline of the dodecahedral shape is given; c) the graphical representation of the condition (3.12), which allows to select nodes of the 6D lattice that form the AKNt. Source: part b) taken from [143]

The AKNt is composed of two rhombohedral units called prolate and oblate. The other frequently used names are acute and obtuse rhombohedra, respectively. Two rhombohedra are spanned

by vectors of the icosahedral setting, in which vectors are directed to the corners of the icosahedron. Each rhombohedron is spanned by three vectors (Fig. 11 [143]).

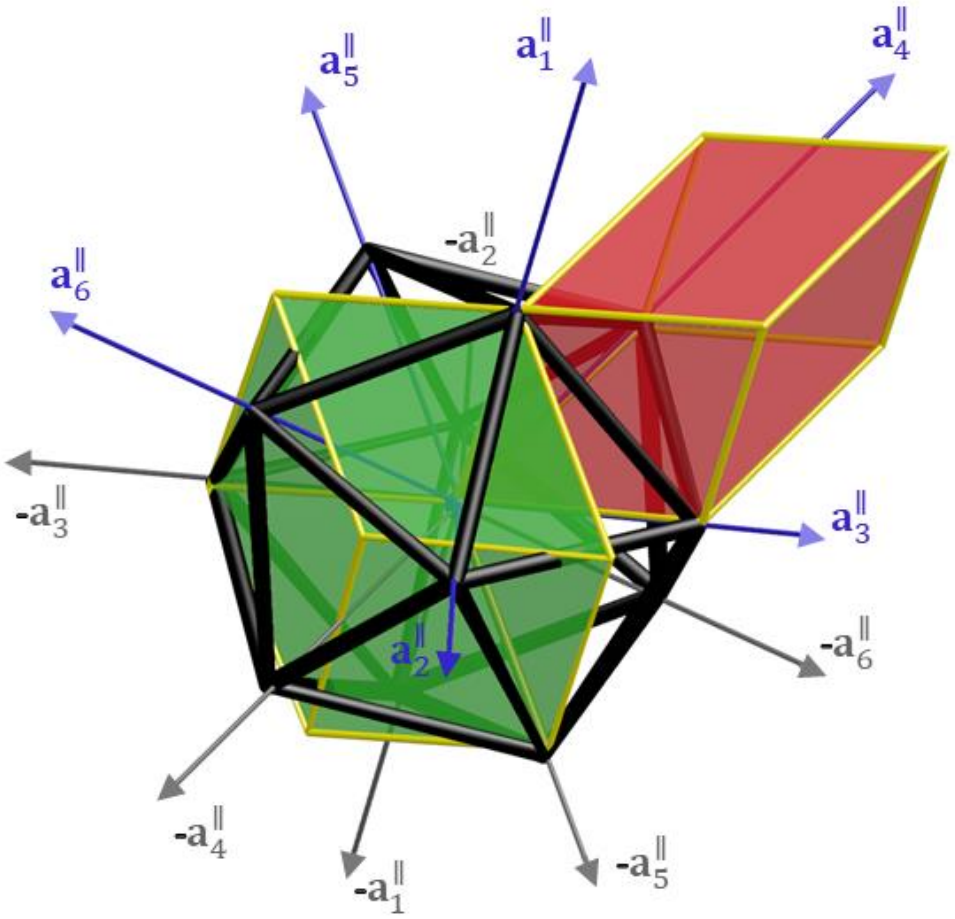

Figure 11. Two rhombohedra as spanned by vectors of the icosahedral setting. Source: [143]

The prolate rhombohedron is spanned by vectors pointing toward vertices of icosahedron constituting one of its twenty faces. The long body-diagonal of the rhombohedron is collinear with a 3-fold direction, going through the middle of the triangular face. It is more difficult to visualize the oblate rhombohedron being spanned by vectors of the icosahedral setting because those three vectors do not point toward vertices of the same face of the icosahedron. However, it is still true that the body-diagonal, this time the short one, is collinear with a 3-fold axis. In an icosahedron there are twenty 3-fold axes however, half of them are related to remaining by the inversion symmetry. The number of symmetry independent 3-fold axes, when corresponded to long and short-body diagonals of rhombohedra determine how many possible orientations of each rhombohedron can be found in the AKNt. Since there are ten 3-fold axes, that means there are ten orientations for each rhombohedron. Each of two types of rhombohedra can be additionally divided into two classes. Within the same class, rhombohedra are symmetrically dependent with respect to the rotation around 5-fold axis, which is directed along the *z*-

axis (along the vector $\mathbf{a}_i$). Such a subdivision is very convenient with respect to the structure factor calculations.

Within the occupation domain, the region representing each of the rhombohedrons can be distinguished (Fig. 12). It was already mentioned that the occupation domain is a perpendicular space representation of the points in the physical space. Even more, each local arrangement of points in the physical space has a certain shape within the occupation domain. At this moment I will focus on the distribution of the reference vertex of each type of rhombohedra within the occupation domain.

All the nodes of the AKNt form a rhombic triacontahedron but a subset of those points will form a different polyhedron that is contained within the rhombic triacontahedron. A rhombohedron has eight vertices. If I choose one of those vertices as a reference vertex, the geometry of a rhombohedron is uniquely determined by vectors originating from this vertex. In the first step, I am interested in what is the shape of rhombohedron in the perpendicular space. The perpendicular space rhombohedron is spanned by exactly the same vectors but their perpendicular space components. It is easy to find that the oblate rhombohedron has the shape of a prolate rhombohedron in the perpendicular space and the prolate rhombohedron has the shape of an oblate rhombohedron. Now, by shifting the perpendicular space rhombohedron within the boundaries defined by the rhombic triacontahedron a perpendicular space representation of the reference vertex draws a pattern in the perpendicular space. None of the vertices of rhombohedron can cross the rhombic triancontahedron, because that would mean the vertex is generating a position in the parallel space that is not a part of the AKNt. The shape defined by all the possible positions of the reference vertex is once again a rhombohedron. For the oblate one, the distribution has the shape of an oblate rhombohedron and for the prolate one, a prolate rhombohedron. All the distributions of the reference vertex, for two types of rhombohedra in 10 orientations each, are shown in Fig. 12.

The following naming convention helps to uniquely define what is the type and the orientation of the rhombohedron. The prolate rhombohedron can be denoted as L and the oblate one as S. Such a notation is usually used to denote two possible bonds in the Fibonacci chain that serves as a toy model for many investigations done for quasicrystals. In this context, L stands for 'long' and S stands for 'short', which is rather intuitional. Also, such a notation is used to denote two rhombuses in the Penrose tiling, where a thick rhombus is called L and a thin is called S. The same notation can be adapted for the AKNt since only two units, among which one is τ larger in volume than another, are necessary to construct the tiling. The unit is characterized not only by its type but also the orientation. The orientation of the unit is given by three vectors originating from one of its vertices and are spanning the rhombohedron. For instance, the prolate rhombohedron shown in Fig. 11 is founded on vectors: $\mathbf{a}_1$, $\mathbf{a}_3$, $\mathbf{a}_4$. Therefore the rhombohedron can be called L_{134}. The type and the orientation is uniquely determined is such a notation. The order of indices in the subscript does not matter due to the threefold symmetry. The reference vertex of the rhombohedron is also automatically known, since there is only

one vertex where vectors in such an orientation are originating. For instance, the notation $L_{\overline{134}}$ refers to the rhombohedron of the same type and orientation as L_{134} but the reference vertex is the vertex laying on the opposite side of the long body-diagonal.

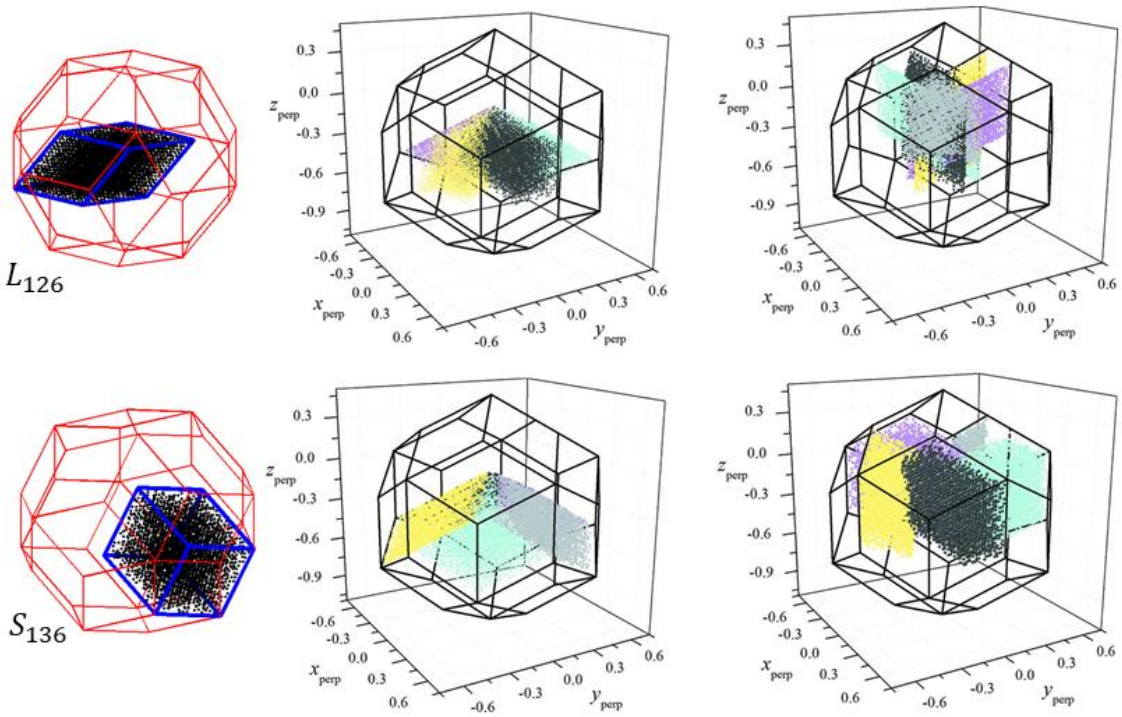

Figure 12. The distribution of the reference vertices of the prolate and oblate rhombohedron. On the left-hand side exemplary distributions are given, whereas on the right-hand side all the distributions are plotted, divided into symmetrically related with respect to the 5-fold axis. Source: the righhand side taken from [126].

The AKNt has two unique properties associated with the 6D representation that have consequences in further calculations. First, let's consider the generators of the symmetry operations of the 6D space group isomorphic with a 3D icosahedral point group: $\Gamma(5), \Gamma(3), \Gamma(2), \Gamma(\bar{1}), \Gamma(m)$. The fivefold symmetry is particularly important. It's matrix representation is:

$$\Gamma(5) = \begin{pmatrix} 1 & 0 & 0 & 0 & 0 & 0 \\ 0 & 0 & 0 & 0 & 0 & 1 \\ 0 & 1 & 0 & 0 & 0 & 0 \\ 0 & 0 & 1 & 0 & 0 & 0 \\ 0 & 0 & 0 & 1 & 0 & 0 \\ 0 & 0 & 0 & 0 & 1 & 0 \end{pmatrix}. \tag{3.13}$$

Matrix (3.13) can be block-diagonalized by the similarity operation with the matrix **W** to give the irreducible representation in the orthogonal, parallel and perpendicular subspaces:

$$\Gamma(5)_{\mathbf{W}} = \mathbf{W}\Gamma(5)\mathbf{W}^{-1} = \begin{pmatrix} \cos\frac{2\pi}{5} & \sin\frac{2\pi}{5} & 0 & 0 & 0 & 0 \\ -\sin\frac{2\pi}{5} & \cos\frac{2\pi}{5} & 0 & 0 & 0 & 0 \\ 0 & 0 & 1 & 0 & 0 & 0 \\ 0 & 0 & 0 & \cos\frac{4\pi}{5} & \sin\frac{4\pi}{5} & 0 \\ 0 & 0 & 0 & -\sin\frac{4\pi}{5} & \cos\frac{4\pi}{5} & 0 \\ 0 & 0 & 0 & 0 & 0 & 1 \end{pmatrix} = \begin{pmatrix} \Gamma^{\parallel}(5)_{\mathbf{W}} & 0 \\ 0 & \Gamma^{\perp}(5)_{\mathbf{W}} \end{pmatrix}. \tag{3.14}$$

From (3.14) it is evident that a $\frac{2\pi}{5}$ rotation around a fivefold axis in the parallel space corresponds to a $\frac{4\pi}{5}$ rotation in the perpendicular space. That means the distributions of reference vertices of rhombohedra L_{126} and L_{123}, which are symmetric with respect to a rotation $\frac{2\pi}{5}$ along a vector $\mathbf{a}_1$, are symmetric to each other in the perpendicular space with respect to the rotation along a $\mathbf{a}_1^{\perp}$ about angle $\frac{4\pi}{5}$.

Another important property is the Bravais hyperlattice **L** is invariant under the action of the scaling matrix:

$$S = \frac{1}{2}\begin{pmatrix} 1 & 1 & 1 & 1 & 1 & 1 \\ 1 & 1 & 1 & \bar{1} & \bar{1} & 1 \\ 1 & 1 & 1 & 1 & \bar{1} & \bar{1} \\ 1 & \bar{1} & 1 & 1 & 1 & \bar{1} \\ 1 & \bar{1} & \bar{1} & 1 & 1 & 1 \\ 1 & 1 & \bar{1} & 0 & 1 & 1 \end{pmatrix}. \tag{3.15}$$

The matrix S can be block-diagonalised with the matrix **W**, by a similarity operation, to give components of the scaling operations in two subspaces:

$$S_{\mathbf{W}} = \begin{pmatrix} \tau & 0 & 0 & 0 & 0 & 0 \\ 0 & \tau & 0 & 0 & 0 & 0 \\ 0 & 0 & \tau & 0 & 0 & 0 \\ 0 & 0 & 0 & -\frac{1}{\tau} & 0 & 0 \\ 0 & 0 & 0 & 0 & -\frac{1}{\tau} & 0 \\ 0 & 0 & 0 & 0 & 0 & -\frac{1}{\tau} \end{pmatrix} = \begin{pmatrix} S_{\mathbf{W}}^{\parallel} & 0 \\ 0 & S_{\mathbf{W}}^{\perp} \end{pmatrix}. \tag{3.16}$$

After the inflation, the parallel space becomes τ times larger, but the perpendicular space components are compressed τ times and additionally, they are inversed. The P lattice is invariant not after the single action of the matrix S but S^3 [144]. Therefore the rhombohedra in the inflated AKNt have τ^3 longer edge-length, and the perpendicular space distribution shrinks $(-1)^3\tau^3$ times. The F lattice can be inflated just by the matrix S. In conclusion, primitive icosahedral quasicrystals exhibit τ^3 scaling, whereas face-centered icosahedral quasicrystals exhibit τ scaling. It affects both the direct space and the reciprocal space.

3.3 The structure factor

The structure factor formula is the basic mathematical tool to compare the atomic structure with the experimental diffraction data. The structure factor is the Fourier Transform of the electron density in the crystal, no matter whether the crystal is periodic or not. The atomic structure can be pictured as a convolution of the lattice and the atomic decoration of the unit cell in the case of periodic crystal. Even though the notion of periodicity is invalid for a quasicrystal (at least in the physical space) the lattice-and-decoration approach still can be used. In this case, the periodic lattice is replaced by the aperiodic tiling which serves as a quasilattice. For a tiling to be quasiperiodic, at least two tiles are necessary. The electron density ρ in an aperiodic crystal with two units: L and S can be expressed as a sum over all their possible orientations:

$$\rho = \sum_{o} \left(\rho_{Lo} * \rho_{Lo}^{atomic} + \rho_{So} * \rho_{So}^{atomic} \right), \tag{3.17}$$

where o enumerates all possible orientations of the units L and S. $\rho_{L\alpha}(\rho_{S\alpha})$ is a subset of the nodes form a tiling that corresponds to reference vertices of all the tiles of the type $L(S)$ in the orientation o. The atomic decoration of the tile can be orientation-dependent, in general, but usually the symmetry of the crystal imposes the same decoration for a particular type of the tile, independently on the orientation. In the AKNt each type of the tile occurs in ten possible orientations, therefore the sum in (3.17) runs from one to ten. The Fourier Transform of (3.17) yields [126]:

$$\begin{aligned} F(\mathbf{k}) = \sum_{o=1}^{10} \left(F(\mathbf{k})_o^L \sum_{j=1}^{N_1} f_j(\mathbf{k}) \alpha_j p_j e^{2\pi i \mathbf{k} \mathbf{r}_j} \right) \\ + \sum_{l=1}^{10} \left(F(\mathbf{k})_o^S \sum_{j=1}^{N_2} f_j(\mathbf{k}) \alpha_j p_j e^{2\pi i \mathbf{k} \mathbf{r}_j} \right), \end{aligned} \tag{3.18}$$

where $F(\mathbf{k})_o^L$ ($F(\mathbf{k})_o^S$) is the Fourier Transform of the reference points of rhombohedron $L(S)$ in the orientation o, $N_{1(2)}$ – number of atoms decorating rhombohedron $L(S)$, $f_j(\mathbf{k})$ – atomic form factor of the jth atom, α_j – part of the atom laying within rhombohedron and p_j – a probability that a site j is occupied (often called site of fraction parameter (SOF)) and $N_{1(2)}$ – the number of atoms in the unit $L(S)$. For now, the corrections for atomic disorder, except for SOF, are not taken into account. The position of the jth atom $\mathbf{r}_j$ is calculated with respect to the reference vertex of the rhombohedral unit, from which the spanning vectors are originating. It is best to express the coordinates of the vector $\mathbf{r}_j$ in the basis of vectors spanning the rhombohedral unit: $\mathbf{r}_j = x\mathbf{f}_1^{\parallel} + y\mathbf{f}_2^{\parallel} + z\mathbf{f}_3^{\parallel}$, where $x, y, z \epsilon [0,1]$ (Fig. 13). Let's consider for instance the rhombohedron L_{126} with $\mathbf{f}_1^{\parallel} = \mathbf{a}_1^{\parallel}, \mathbf{f}_2^{\parallel} = \mathbf{a}_2^{\parallel}, \mathbf{f}_3^{\parallel} = \mathbf{a}_6^{\parallel}$. By representing the atomic vector in reduced coordinates, the symmetry equivalent positions can be easily found. For instance if $x = y = z$ that means the site lays on a long body-diagonal of a rhombohedron, being collinear with a vector $\mathbf{a}_1^{\parallel} + \mathbf{a}_2^{\parallel} + \mathbf{a}_6^{\parallel}$. If $x = 0$ then site lays on the face spanned by vectors $\mathbf{a}_2^{\parallel}$ and $\mathbf{a}_6^{\parallel}$. Also in this form, the coordinates are independent on the orientation of rhombohedron and do not have to be transformed to calculate the atomic component of the structure factor. In order to reconstruct vector $\mathbf{r}_j$ for the rhombohedron in the other orientation, the vector $[x, y, z]$ must be multiplied by corresponding vectors that span the other rhombohedron.

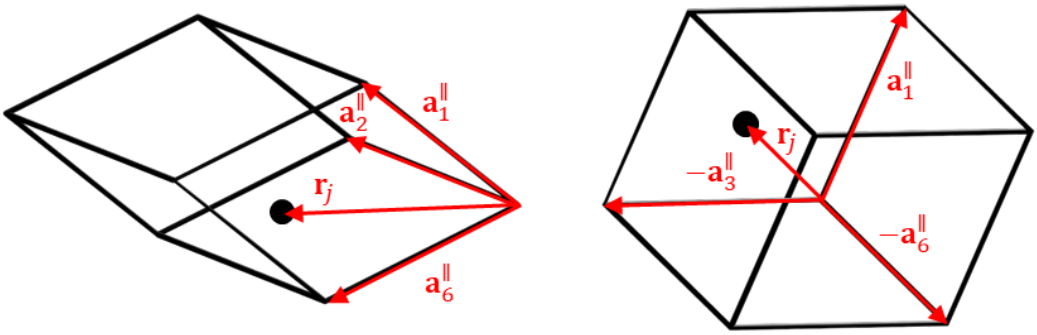

Figure 13. The atomic position vector $\mathbf{r}_j$ can be represented in the basis of vectors spanning two rhombohedral units. The coefficients of the linear combination are within $[0,1]$ region and allow to easily find symmetry-dependent special positions in a thombohedron. Spanning vectors of each type of rhombohedron are shown.

3.3.1 The geometric structure factor

The geometric part of the structure factor is associated with the Fourier Transform of the reference vertices positions of structure units in the tiling. The calculation is the easiest to be conducted in the nD or the AUC space. In the real space, the set of projected 6D lattice points is discrete and

unbound. The $F(\mathbf{k})_o^{L(S)}$ component, which is the part of the structure factor related to the lattice of quasicrystal, is equal to:

$$F(\mathbf{k})_o^{L(S)} = \sum_{i=1}^{\infty} \exp\left(i\mathbf{k}\mathbf{r}_i^{\mathrm{ref}}\right), \tag{3.19}$$

Where $\mathbf{r}_i^{\mathrm{ref}}$ is the position of the reference vertex of the ith rhombohedron in the quasilattice. It is an infinite sum over all the rhombohedral units. In the perpendicular space, the set of projected nodes is also discrete but it is bound to the shape of rhombohedron as it is shown in Fig. 12. The set of projected points is dense, meaning between two, arbitrarily chosen points there always exists the third point. It is, therefore, possible to change the infinite sum into an integral over a bounded region, keeping in mind that $\mathbf{k}\mathbf{r}_i^{\mathrm{ref}} = -\mathbf{k}_\perp \cdot \mathbf{r}_{i\perp}^{\mathrm{ref}}$, what comes from (2.8):

$$F(\mathbf{k})_o^{L(S)} = \int_{\Delta L(S)_o} P(\mathbf{r}_\perp^{\mathrm{ref}}) \exp\left(-i\mathbf{k}_\perp \cdot \mathbf{r}_\perp^{\mathrm{ref}}\right) \mathrm{d}\mathbf{r}_\perp^{\mathrm{ref}}, \tag{3.20}$$

where $\Delta L(S)_o$ corresponds to the shape of the distribution in the perpendicular space generated by reference vertices of rhombohedra $L(S)_o$ and $\mathbf{r}_\perp^{\mathrm{ref}}$ is the coordinate of the reference vertex in the perpendicular space. The $\mathbf{k}_\perp$ is a perpendicular space vector obtained as a projection of the 6D reciprocal space vector $\mathbf{G} = \sum_{i=1}^{\mathbf{6}} \boldsymbol{h}_i \mathbf{d}_\mathbf{i}^*$ onto the perpendicular space. It is easy to see that (3.20) has a similar form to (2.7), even so, the former is written in the nD coordinates and the latter is written in the AUC units. The equivalence of those two approaches is once again evident.

The integral (3.20) can be easily solved in the oblique coordinates setting [145]. The region $\Delta L(S)_o$ has the shape of rhombohedron that is spanned by three vectors, for now let's name them $\mathbf{f}_1^\perp, \mathbf{f}_2^\perp, \mathbf{f}_3^\perp$, originating from the same vertex. Those three vectors define the oblique basis. Every point $\mathbf{r}_\perp^{\mathrm{ref}}$ of the distribution $\Delta L(S)_o$ can be obtained as a linear combination of those three vectors: $\mathbf{r}_\perp^{\mathrm{ref}} = x\mathbf{f}_1^\perp + y\mathbf{f}_2^\perp + z\mathbf{f}_3^\perp, x, y, z \in [0, 1]$. Coordinates x, y, z become the new integration variables. The coordinates of the $\mathbf{k}_\perp$ must also be expressed in the oblique basis: $\mathbf{k}_\perp = q_1\mathbf{f}_1^{\perp *} + q_2\mathbf{f}_2^{\perp *} + q_3\mathbf{f}_3^{\perp *}$, where $q_i = \mathbf{k}_\perp \cdot \mathbf{f}_i^\perp$ and $\mathbf{f}_i^{\perp *} \cdot \mathbf{f}_j^\perp = 2\pi\delta_{ij}, i, j = 1, 2, 3$. Formula (3.20) in the oblique basis $\mathbf{f}_1^\perp, \mathbf{f}_2^\perp, \mathbf{f}_3^\perp$takes the form:

$$F(\mathbf{k})_o^{L(S)} = V\exp(-\mathrm{i}\mathbf{k}_\perp\mathbf{r}_{\mathrm{or}}^\perp) \int_0^1 \mathrm{d}x \int_0^1 \mathrm{d}y \int_0^1 \exp(-i[q_1, q_2, q_3\,] \cdot [x, y, z])\mathrm{d}z\,, \tag{3.21}$$

where $\mathbf{r}_{\mathrm{or}}^{\perp}$ is the position of the vertex from which the oblique basis vectors originate and $V = \left|\mathbf{f}_1^{\perp} \cdot (\mathbf{f}_2^{\perp} \times \mathbf{f}_3^{\perp})\right|$. After the integration, the result is:

$$F(\mathbf{k})_o^{L(S)} = \frac{iV\exp(-\mathrm{i}\mathbf{k}_{\perp}\mathbf{r}_{\mathrm{or}}^{\perp})}{q_1 q_2 q_3}[\exp(-iq_1) - 1][\exp(-iq_2) - 1][\exp(-iq_3) - 1], \tag{3.22}$$

where $V = \left|\mathbf{f}_1^{\perp} \cdot (\mathbf{f}_2^{\perp} \times \mathbf{f}_3^{\perp})\right|$. The integral (3.22) must differentiated with respect to certain values of q_i:

if $q_3 = 0, q_1 = q, q_2 = p/q_2 = 0, q_1 = q, q_3 = p/q_1 = 0, q_2 = q, q_3 = p$:

$$F(\mathbf{k})_o^{L(S)} = \frac{-iV\exp(-\mathrm{i}\mathbf{k}_{\perp}\mathbf{r}_{\mathrm{or}}^{\perp})}{qp}[\exp(-iq) - 1][\exp(-ip) - 1]; \tag{3.23}$$

if $q_3 = 0, q_1 = 0, q_2 = q/q_2 = 0, q_1 = 0, q_3 = q/q_2 = 0, q_3 = 0, q_1 = q$:

$$F(\mathbf{k})_o^{L(S)} = \frac{-iV\exp(-\mathrm{i}\mathbf{k}_{\perp}\mathbf{r}_{\mathrm{or}}^{\perp})}{q}[\exp(-iq) - 1]; \tag{3.24}$$

if $q_1 = 0, q_2 = 0, q_3 = 0$:

$$F(\mathbf{k})_o^{L(S)} = V\exp(-\mathrm{i}\mathbf{k}_{\perp}\mathbf{r}_{\mathrm{or}}^{\perp}). \tag{3.25}$$

In Table 2 the information about vectors spanning each distribution of the rhombohedron and the origin of the oblique basis is given. Numbers '1' and '2' define two classes within which rhombohedra are symmetric to each other with respect to the rotation around the fivefold axis directed along the vector $\mathbf{d_1}$ (for the icosahedral setting 1). All the distributions can be recovered by applying the rotation symmetry to each of the spanning vector. The one must remember the rotation $2\pi/5$ in a real space corresponds to a rotation $4\pi/5$ in a perpendicular space.

Table 2. The vectors spanning the distribution of the reference vertex in a perpendicular space. To obtain all the distributions, a rotation along $\mathbf{d}_1^{\perp}$ 5-fold axis must be made.

	$\mathbf{f}_1^{\perp}$	$\mathbf{f}_2^{\perp}$	$\mathbf{f}_3^{\perp}$	$\mathbf{r}_{\mathbf{or}}^{\perp}$
Prolate 1 (L_{126})	$\mathbf{d}_3^{\perp}$	$\mathbf{d}_5^{\perp}$	$\mathbf{d}_4^{\perp}$	$[0,0,0]$
Prolate 2 ($L_{\bar{4}62}$)	$\mathbf{d}_3^{\perp}$	$\mathbf{d}_5^{\perp}$	$-\mathbf{d}_1^{\perp}$	$\mathbf{d}_1^{\perp} + \mathbf{d}_4^{\perp}$
Oblate 1 ($S_{1\bar{3}\bar{6}}$)	$\mathbf{d}_2^{\perp}$	$\mathbf{d}_4^{\perp}$	$\mathbf{d}_5^{\perp}$	$\mathbf{d}_3^{\perp} + \mathbf{d}_6^{\perp}$

Oblate 2 ($S_{25\bar{6}}$)	$\mathbf{d}_3^{\perp}$	$-\mathbf{d}_1^{\perp}$	$\mathbf{d}_4^{\perp}$	$\mathbf{d}_6^{\perp} + \mathbf{d}_1^{\perp}$

3.3.2 The SOF and site occupancy

Not every atomic site must be fully occupied with the probability equal to one. Due to the atomic disorder happening in the structure some sites can be partially occupied. It must be remembered that the structure solution obtained from the X-ray diffraction with the use of Bragg reflections is the average structure. If the atomic arrangement in the structure allows for certain atoms to maneuver in a structure what can be obtained by the diffraction is the average position, resulting in split atomic positions. In quasicrystals, the natural cause of partially occupied sites is the phason disorder. As it was shown in Fig. 9 the flip of the atom from site *A* to *A'* makes each site partially occupied by an atom, therefore in the model, the probability that each site is occupied must be assigned. In the structure refinement the parameter p_j in equation (3.18) is a free parameter that is adjusted by the optimization algorithm.

Apart from partially occupied sited the chemical mixing between atomic elements can occur, i.e. one atomic site can be occupied by two or more different atomic elements. For a particular atomic site, that is chemically disordered, an average scattering form factor $f_{av}(\mathbf{k})$ can be introduced:

$$f_{av}(\mathbf{k}) = \sum_{i=1}^{N} p_{ei} f_i(\mathbf{k}) \,, \sum_{i=1}^{N} p_{ei} = 1, \tag{3.26}$$

where $f_i(\mathbf{k})$ is a scattering form factor of the ith element occupying a certain site. Sum of all probabilities p_{ei} has to add up to one since an atomic site cannot be occupied by more than one full atom. It can, however, be the partially occupied site, therefore a total probability, apart from probabilities of chemical mixing, can be lower than one. The parameter p_j in the equation (3.18) is meant to represent the partially occupied site, therefore it should not be confused with p_{ei} in equation (3.26) that represents chemical mixing probability. It is differentiated purposely to distinct those two situations.

Apart from the action of disorder, some positions in the atomic model are high-symmetry sites. For instance, an atom on the face of the unit, that is used as a building block of the structure, is shared with an adjacent unit. Therefore the part of an atom that lays within a unit is half of the full atom. In addition, when an asymmetric part of the unit is used for calculations to reduce the number of parameters in the model, only a fraction of an atom lays within the asymmetric unit on the high-symmetry sites. The fractions must be taken into account otherwise one atom would be taken multiple times during calculations. In the formula (3.18), it is dealt with by adding a parameter α_j. It says what part of an atom exists within the structure unit. The high-symmetry sites can be classified into three groups: face-sites, edge-sites and vertex-sites. When an atom in on the face of the unit, the fraction $\alpha_j = 0.5$. For the edge-

sites the fraction of an atom can be calculated with the use of an angle between two faces that intersect to create an edge. The angle can be extracted using the inner product between normal vectors of the faces. If $\mathbf{n}_1$ is the normal vector of the first face and $\mathbf{n}_2$ is the normal vector of the second face, than

$$\alpha_j = \frac{\pi - \operatorname{acos}\left(\frac{\mathbf{n}_1 \cdot \mathbf{n}_2}{\|\mathbf{n}_1\|\|\mathbf{n}_2\|}\right)}{2\pi}. \tag{3.27}$$

Both vectors $\mathbf{n}_1$ and $\mathbf{n}_2$ must point outward the center of polyhedron in order for formula (3.27) to be valid. When the fraction site is calculated for a vertex-site the following formula can be used [146]:

$$\alpha_j = \frac{2}{4\pi} \operatorname{atan}\left(\frac{|(\mathbf{a} \times \mathbf{b}) \cdot c|}{\|\mathbf{a}\|\|\mathbf{b}\|\|\mathbf{c}\| + (\mathbf{a} \cdot \mathbf{b})\|\mathbf{c}\| + (\mathbf{a} \cdot \mathbf{c})\|\mathbf{b}\| + (\mathbf{b} \cdot \mathbf{c})\|\mathbf{a}\|}\right), \tag{3.28}$$

where $\mathbf{a}$, $\boldsymbol{b}$, $\boldsymbol{c}$ are vectors pointing out of the vertex in which the fraction site is calculated. In (3.28) the division with 4π, whereas in (3.27) the division with 2π is made. It is due to the fact, that in (3.27) the fraction of the full planar angle (2π is a full angle) is calculated, whereas in (3.28) the fraction of a solid angle (4π is a full angle) is calculated. In Table 3 the values of fractions are given with the label presented in Figure 14.

Table 3. The list of all fraction parameters α_j, depending on the type of rhombohedron and the position of an atom within the rhombohedral unit.

	SITE	**1**	**2**	**3**	**4**	**5**	**6**
PROLATE	Edge-site	0.1	0.25	0.3	0.25	0.1	1/6
	Vertex-site	1/120	0.075	0.75	1/120	-	-
OBLATE	Edge-site	0.2	0.25	0.1	0.25	0.2	1/6
	Vertex-site	7/120	1/4	1/4	7/120	-	-

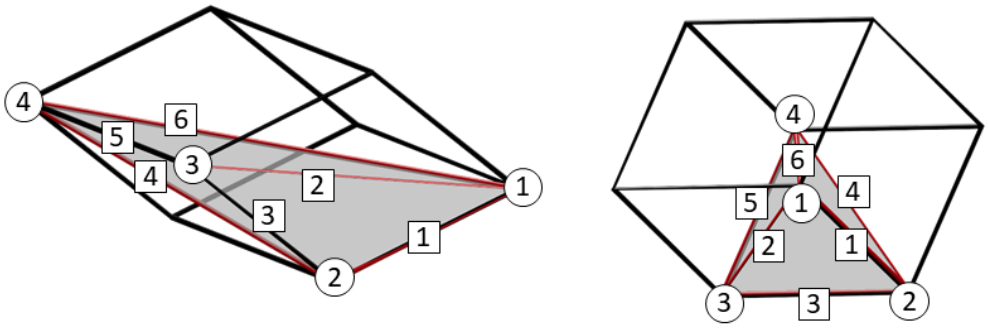

Figure 14. Labels corresponding to site number in Table 3. Squares correspond to edge-sites and circles correspond to vertex-sites.

3.3.3 Phason and phonon disorder

This chapter will describe the deviations of the atomic structure from the idealized mathematical model. Two types of disorder, directly affecting the calculation of the structure factor and in some way correlated with each other, are particularly important - phononic and phasonic disorder. The first applies to both periodic and aperiodic structures. The second is characteristic of aperiodic structures and is closely related to the spatial arrangement of atoms.

3.3.3.1 Phonons

The correlated movement of atoms resulting from the thermal excitation of atoms is called a phonon. Atoms can vibrate in a complicated manner in many of the available modes. The analysis of possible vibration modes is carried out using the fact of the lattice periodicity, thanks to which the number of possible vibration modes of the structure is finite. The situation is quite different in quasicrystals. Lack of translational symmetry means that there can be many oscillating states of atoms. In order to theoretically describe the vibrations of the quasicrystalline structure, the existing hydrodynamic model for periodic crystals was used and extended to quasicrystals [79, 147] by using the superspace approach. Unfortunately, the level of knowledge is still not enough to clearly determine how atoms behave in the quasicrystal under the influence of thermal excitation. The existence of an acoustic branch for quasicrystals is well confirmed, both experimentally and in simulations carried out for large quasicrystalline periodic approximants [148, 149]. Therefore, according to the theory of acoustic vibrations, it should be right to apply an exponential correction to the intensity of diffraction peaks in the form of the Debye-Waller formula. However, the same research shows the existence of optical modes as strong as the acoustic modes, but it is difficult to find dispersion relations in them. Optical modes are highly localized and dispersive, which has been confirmed for a number of quasicrystals [150]. This undermines the validity of the exponential amendment for the analysis of atomic vibrations

in an uncorrelated manner, subjected to the action of local potential. Therefore, one may be tempted to apply the amendment assuming local harmonic vibrations, which are independent of the environment. In the average unit cell model, it is possible to take into account an atom deflection associated with local vibrations. All that is needed is an additional component in (2.1), associated with the atom's deflection from the equilibrium position for the reference lattice associated with the main vector k and the modulation vector q (u_p and v_p):

$$\begin{aligned} x &= n\lambda_k + u + u_p, \\ x &= m\lambda_q + v + v_p. \end{aligned} \tag{3.29}$$

Let $u_{new} = u + u_p$ and $v_{new} = v + v_p$. Thus, the new variables in the AUC are the sum of statistical variables: positions resulting from geometry and atomic deflections from the equilibrium position. They cause that the probability distribution, previously homogeneous and non-zero along the v(u) curve, becomes smeared (Fig. 15 [84]). The new probability distribution, taking into account the average structure, becomes smeared at the edges, and the linear relation v(u) becomes invalid. It is necessary to use a general probability distribution, which is a convolution of the undisturbed distribution of atomic positions and the distribution of vibrations in the structure. The convolution is only possible if the atom's deflection from the equilibrium position is independent of this position, which is true for localized modes. It can be shown that the quasicrystalline structure factor can be written as the product of the factor responsible for atomic vibrations $F_{\mathrm{p}}(k)$, and the part related to quasicrystalline geometry $F_0(k)$ [65]:

$$\begin{aligned} F(k) &= \int_0^{\lambda_k} P(u)\mathrm{e}^{\mathrm{i}k_0(n-\tau m)u}\,\mathrm{d}u \int_0^{\lambda_k} G(u_{\mathrm{p}})e^{ik_0(n+m/\tau)u_{\mathrm{p}}}\,\mathrm{d}u_{\mathrm{p}} \\ &= F_0(k)F_{\mathrm{p}}(k), \end{aligned} \tag{3.30}$$

where $G(u_{\mathrm{p}})$ is a distribution function of atomic fluctuations around an equilibrium. The rest of the variables are the same as in (2.6). If the assumption that atomic vibrations are harmonic and are locally independent, than:

$$G(u_{\mathrm{p}}) = \frac{1}{\pi A}\frac{1}{\sqrt{1-\left(\frac{u_{\mathrm{p}}}{A}\right)^2}}, \tag{3.31}$$

where A – the amplitude of oscillation. The Fourier Transform of (3.31) is a Bessel function of the first kind rank 0.

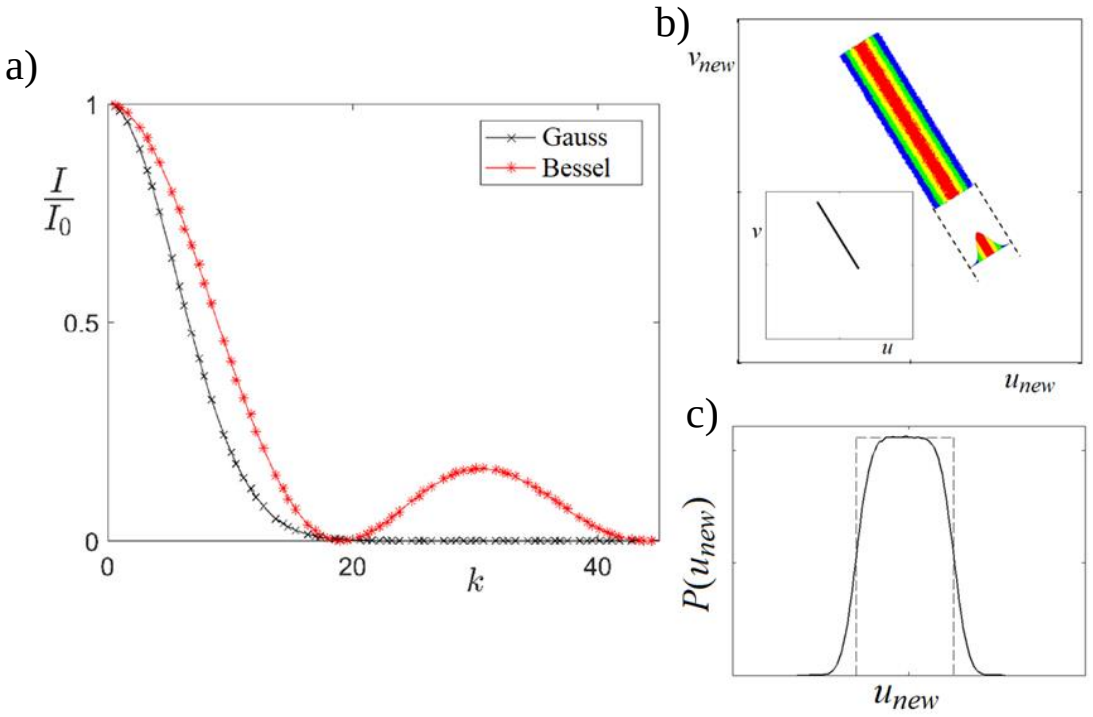

Figure 15. The influence of tha atomic vibrations on the diffraction pattern (a)) and the shape of the atomic distribution function in the AUC scheme (b) and c)). It is evident that for the similar magnitude of atomic vibrations, for short k vectors the Gaussian Debye-Waller factor and the Bessel correction is the same, however for localized modes a bump in the intensities is expected for a high values of the k vectors. In a) the vector k is normalized by the norm of the (1, 0) vector; b): the $v(u)$ relation is no longer linear but is smeard along a [1, 1] direction in the vu space; c): the marginal distribution stops being a uniform distorbution. Source: [84]

3.3.3.2 Phasons

Phase disorder is an intrinsic feature of the quasicrystalline structures [151]. In the nD model, phason can be identified with a wave of disturbances propagating only in the perpendicular space [152]. In the physical space, this wave causes the atom to jump to energetically equivalent positions, as seen in Fig. 9. Phasons are speculated to play an important role in understanding why quasicrystals are stable [153]. The *in situ* observation of the growth of quasicrystals clearly shows that the growth takes place by adding successive atomic layers, strongly defective, followed by the process of structure relaxation (Fig. 16 [154]). The arrangement of atoms is similar or ideally as it would appear from a computer-

generated mathematical model of structure [154]. However, there are cases when the structure remains strongly defective in terms of phonon disorder, i.e. a random type structure is created [155].

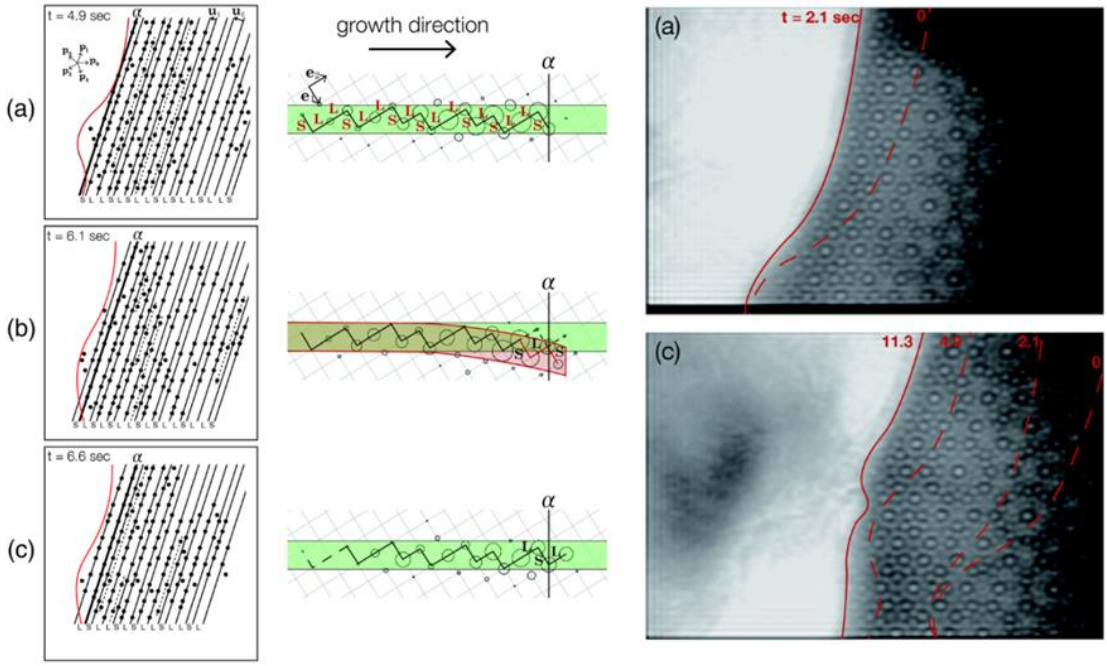

Figure 16. Growth $Al_{70.8}Ni_{19.7}Co_{9.5}$ as seen by HRTEM at 1183 K. Model planes (left) were obtained from electron microscopy images. The distances between the planes form a series of long "L" and short "S" distances, forming a Fibonacci sequence. This sequence spoils, as shown in (b), after which, due to the relaxation of the structure, it rebuilds through phase shift (C). The order of the layers becomes consistent with the mathematical formula of the Fibanacci sequence. Source: [154]

An important issue is the effect of phase jumps on the diffraction pattern (Fig. 17). As the number of phase jumps increases, the intensity of the diffraction peaks changes (Fig. 17 b)). This issue is so important that with the current models it is impossible to obtain a correct quasicrystalline structure model without the presence of a correction for this effect. The larger the disorder, the more defective the structure, leading to an amorphous structure (Fig. 17 d)). However, the conditions for which a random type structure is created instead of an energetically stabilized ordered structure with a small number of phonon defects are unknown. The main reason is the lack of refinement of the phonon disorder. The only existing correction for phase disorder is the generalization of the Debye-Waller function to the perpendicular space. It is a Gaussian correction depending on the square of the length of the perpendicular component of the wave vector [152]:

$$D_{phas}(\mathbf{k}) = \exp\left(-\frac{1}{16\pi^2}\mathbf{k}_{\perp}^2 b_{phas}^2\right). \tag{3.32}$$

However, the condition of its operation is the presence of a large phase disorder, on the border of the existence of an ordered structure. In any other case, it is not justified. After all, the Gaussian model is often used, giving the opportunity to refine the phason disorder. It is not true in the whole disorder range (Fig. 17 c) [130]), because only for large phason disorder the probability distribution of atomic positions begins to resemble the Gaussian distribution [130]. What is interesting, even so the distribution function of the tiling with phasosn flips become Gaussian, the diffraction peak scaling with the size of the sample is still Bragg-like, i.e. $I \sim N^2$, where I – intensity of the diffraction peak (Fig. 17 c)). Only after the disorder become even more significant, the scaling indicate the amorphic strucutre is formed.

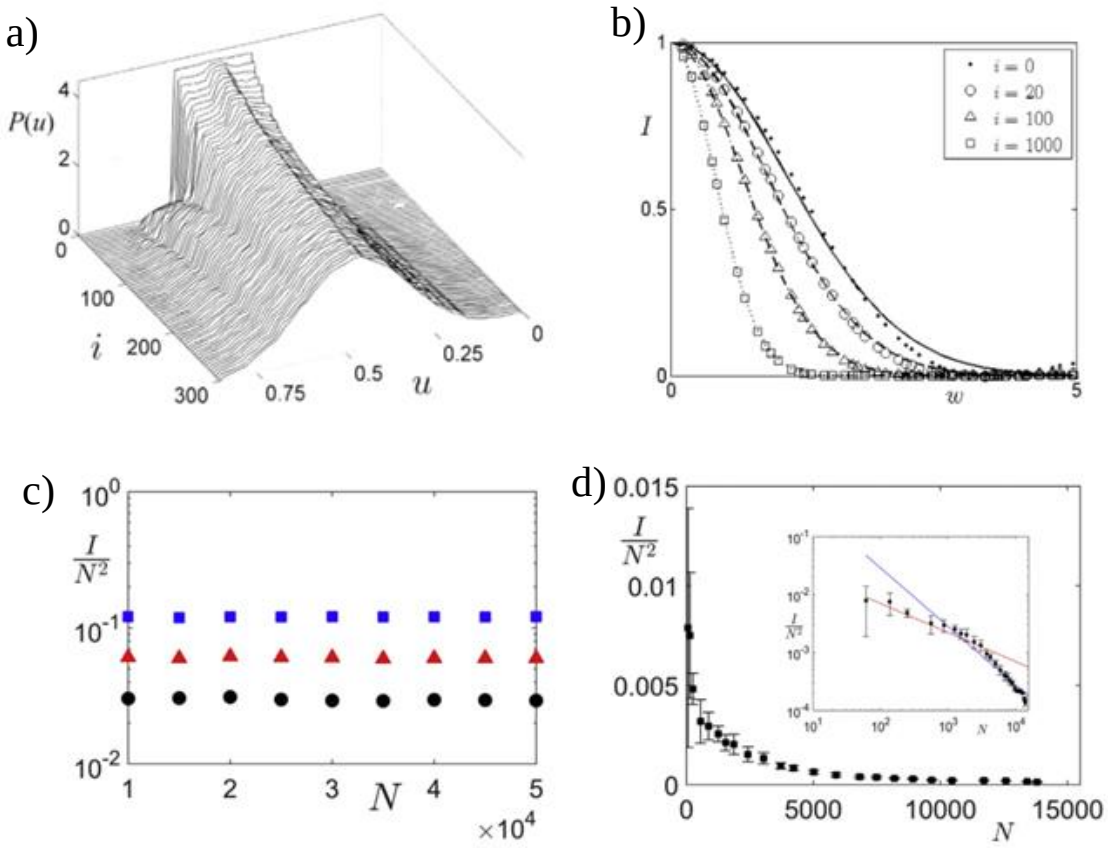

Figure 17. The role of the phason disorder in the diffraction pattern analysis. After a series of the consecutive phason flips (a)) the distribution becomes gaussian-like, influencing the envelope function that becomes narrower and resemble a normal curve. However, even for the gaussian-like atomic distribution, the scaling of the diffraction peaks is Bragg-like (c)), being proportional to N^2. Only after thousands of phsaon flips the scaling of the diffraction peak becomes amorphic (d)), where $I \sim N$. Source: [130]

4. The structure of the Bergman ZnMgTm icoshaedral quasicrystal

This chapter is a republication of the article published in Acta Cryst. A**76**, (2020), 180-196 [143], available online: http://journals.iucr.org/a/issues/2020/02/00/ae5079/index.html. The first paragraph of the article was excluded as the introductory part about the icosahedral quasicrystals was done in chapter 1 and 2 of this thesis.

4.1 The review on the Bergman iQC

The interest in icosahedral Frank-Kasper phases (FK) [55, 105] rose with the discovery of the face centered icosahedral (FCI) AlMgLi [156] and AlMgPd [157]. Their structure is built out of the Bergman cluster which is formed of the dense packing of tetrahedra. After the report by Luo *et al.* [158] that iQC is formed in ZnMgY many iQC phases were found in the ZnMgRE (RE – rare earth element) ternary alloys. The first to be grown were FCI phases with Y, Tb, Dy, Ho and Er [159]. After series of investigations, primitive icosahedral (PI) phases were also grown by rapid solidification with Nd, Sm, Gd, Tb, Ho, Er, Tm, Yb, Lu and Y [160]. Apart from the iQC, the decagonal QC is also found in ZnMgM (M=Y, Dy, Ho, Er, Tm and Lu) [161]. The atomic diameter was shown to play a role in the stabilization of the decagonal phase. Similar mechanism was observed for ZnMg based alloys with a third, trivalent element [66]. The larger the atomic radius, the higher the concentration of the trivalent element in the QC. What is more, for atomic radius ~1.65 Å the PI phase is preferred, rather than the FCI phase, that is formed for the atomic radius ~1.75 Å.

The atomic structures of both PI and FCI Bergman QC were studied in AlCuLi [104] and AlMgLi [162] system respectively. The structure of AlCuLi was first investigated by Elswijk *et al.* [103] constituting a so-called EHSB model based on the simple decoration scheme [163]. The simple decoration scheme assumes the atomic decoration of two original rhombohedra in vertices and mid-edges. The AR is additionally decorated with two atoms on a longer body-diagonal, dividing it in a proportion $\tau/1/\tau$, where τ is the golden ratio. The next take on the structure was made by Yamamoto who introduced major modifications to the EHSB model by removing mid-edges atoms form the AR and replacing them with edge-off center positions [104]. Additionally, the positions of the 12-fold vertices were left unoccupied as they created short distance with edge-off center atoms. The decoration was settled to reflect the local atomic arrangement in the R-AlCuLi cubic approximant as the strong affinity of QC and periodic approximant was known. The same decoration was proposed to explain the structure of the cubic AlZnMg [58]. Based on the local information derived from the approximant crystal, the 6D model of the QC could be constructed. The model is not reliable due to strong mixing of Al, Cu, Li atoms. Later, the model of the FCI AlMgLi was proposed [162]. The same decoration as for the PI

AlCuLi was used, but the reproduction of the superlattice reflections required two icosahedral lattices, with even- and odd-parity nodes.

The more recent model of the Bergman QC was proposed for the PI ZnMgHo QC [164]. The model was based on the result of the *ab initio* phasing of the diffraction amplitudes with LDEM (low density elimination method) [165, 166], implemented in *lodemac* [165] and known structures of the FK approximants [167, 168]. The model was founded on the same framework as the model of the CdYb iQC [62]. Instead of Tsai, Bergman clusters are assumed to occupy the subset of the 12-fold vertices of the AKNt. The additional shell of the rhombic triacontahedron (RTH), that encompasses the so-called "gluing" atoms is considered among traditional shells of the Bergman cluster. The same cluster expansion was originally proposed for Tsai-type QCs approximants. A whole model was set in a 6D space. The three ODs: vertex-centered (OD_V), body-centered (OD_B) and edge-centered (OD_E) are created from the archetype truncated triacontahedron generating the 12-fold vertex environment of the AKNt. The choice of such an archetype OD ensures, that only two types of links between clusters are possible: the *b*-linkage along a 2-fold direction and the *c*-linkage along a 3-fold direction. The *a*-linkage along a 5-fold direction is excluded as it is not observed in approximant crystals and is said to create short interatomic distances. Unfortunately, the model by Takakura *et al.* [164] of the Bergman QC does not include the interstitial atoms, that are atoms outside of the cluster. In the Tsai-type QC the space between clusters is filled with OR and AR decorated according to the simple decoration scheme observed in 1/1 and 2/1 cubic approximants [169, 170]. In the Bergman QC, a unique decoration of two rhombohedra does not exist. It is a local-environment dependent, therefore the complete shape of the OD is difficult to obtain.

The present work on the structure of Bergman QC was motivated by two major factors. Firstly, the Zn-Mg-Rare-Earth QCs are still investigated with respect to the magnetic properties and the search for the long-range magnetic order [171]. The rare-earth ions provide the well-localized magnetic moments originating from the 4*f* electrons. The problem of moment interaction in the quasilattice could be therefore resolved. So far only the spin-glass-like behavior at the low temperature was observed with no magnetic long-range-order. Existing model of the rare-earth atoms distribution in the FCI Bergman phase does not explain the moment's frozen state [172].

Secondly, our research is driven by the deep desire to acquire reliable model of the Bergman QC especially now, when recently the superconductivity in AlZnMg iQC was discovered [59]. That discovery fascinated not only researchers in the area of aperiodic crystals but also the community working in strongly correlated electron systems. This is an ideal time to extend the potential application of the QCs and explore their peculiar properties. The knowledge about the structure of the Bergman QC will play in this venture a major role.

4.2 Experimental details

Single grains of ZnMgTm iQC were grown by a solution growth technique [173]. High purity elements of Zn (Nilaco, 99.99%), Mg (Nilaco, 99.99%) and Tm (Rare Metallic co ltd., 99.9%) with the nominal composition of $Zn_{62.8}Mg_{33.6}Tm_{3.6}$ were put in an alumina crucible and sealed inside a silica ample together with 1/3 atm of argon. The elements in the crucible were melted at 1023 K for 5 h and cooled down to 863 K with a cooling rate -2 K/h using a muffle furnace. After holding at this temperature for about 50 h, the silica ample was quenched in water. The grains of Zn-Mg-Tm iQC, which have a shiny fracture surface, were embedded in a solidified solution. The chemical composition of the iQC was determined to be $Zn_{69.5}Mg_{20.9}Tm_{9.6}$ by a wavelength dispersive X-ray spectroscopy (WDX) on an electron probe micro analyser (EPMA: JEOL, JXA-8530F).

The single crystal X-ray intensity data were collected on a single crystal diffractometer [174] with Mo$K\alpha$ (λ = 0.71073 Å) radiation at ambient temperature. The specimen with a size of 0.07×0.06×0.04 mm^3, which was cut out from a large single grain, was used. The intensity data set was processed using the software package CryAlisPro [174]. Totally 1190808 reflections which were reduced to a data set of unique 3953 reflections, assuming the space group P$m\bar{3}\bar{5}$, indexed with sextet integers with R_{int} = 0.062 were observed. Of these 3010 reflections meet the condition for $F_o > 3\sigma(F_o)$. The icosahedral lattice constant a was determined to be equal to $5.128(3)$ Å. The list of all diffraction reflections is available as a supportive information to the publication [143].

4.3 The ab initio structure solution

The derivation of the initial model for the refinement of aperiodic crystals, especially QCs lacking the average, periodic structure, became much more convenient since the algorithm for the phase retrieval of diffraction amplitudes was invented. There are two iterative algorithms serving the purpose: LDEM [165] implemented in a QUASI07_08 package [109, 108] and charge flipping algorithm [175] used in the *Superflip* software [107]. The *ab initio* phase retrieval allows to obtain a value of the crystallographic *R*-factor around 14-18 % in most cases, what helps immensely to construct an atomic model of the structure. The phase retrieval could not be so accurate unless the high-quality diffraction data weren't accessible. Fortunately, modern detectors allow to collect hundreds of thousands of diffraction peaks with a high-precision.

The 3010 symmetrically independent reflections were used in a phase retrieval and subsequently used to calculate the electron density. The *ab initio* structure solution with *Superflip* resulted in an $R = 14.5\%$ what allows us to consider the electron density calculated with the retrived phases of the diffraction peaks approximates well a real structure. At this stage the preliminary analysis of the structure began.

The standard practice is to calculate the 2D high-symmetry sections through the electron density in the 6D space. From the sections, the general information on the atomic distribution in the structure can be obtained. In Fig. 18 a) the section containing two perpendicular 5-fold axes: [100000] and [011111] is presented. Three ODs are manifested: OD_V (marked V), OD_B (marked B) and OD_E (marked E). Those three ODs are known from the previous study of the ZnMgHo [164], which is isotructural to ZnMgTm. Contrary to the Tsai-type iQC, where cluster centers are generated by the OD_B, in this structure the OD_V, enclosed in the red dashed ellipsoid, spawns the positions of the 12-fold vertices of the AKNt. The empty electron density, manifested in the center of the OD_V, means the cluster center sites should be unoccupied. In addition, the electron density in the OD_V is relatively small, meaning rare-earth elements do not occupy those positions. Tm atoms are expected to occupy the positions generated by the OD_B, as a high concentration of the electron density is located there. Furthermore, in the same figure the white dashed circle shows the overlay of the OD_E and the OD_B. That is the possible phason flip site that occurs along a 5-fold direction in the 3D real space.

In Fig. 18 d) the section through the cluster center in the electron density in 3D real space is shown. The image is perpendicular to a 2-fold axis. The characteristic pattern formed by all the five shells of the Bergman cluster is presented. The shells are the following: small icosahedron, large icosahedron, dodecahedron, soccer-ball polyhedron and the rhombic triacontahedron. The classical Bergan cluster's shells are expanded by considering the rhombic triacontahedron shell as a part of the cluster. Each of the high electron density sites in Fig. 18 d) is related to its corresponding place in Fig. 18 e) showing the 3D shape of each shell. The highest concentration of the electron density occurs at the nodes of the #5 shell. It means that the rare-earth elements occupy all the vertices of the last shell of the RTH cluster.

In Fig. 18 d) no splitting of atomic sites can be perceived but in the sections a)-c) the markers, indicating such a splitting occurs, are detected. In Fig. 18 b) and c) the white arrow shows the splitting of the electron density along a 2-fold and a 3-fold direction, along the perpendicular space component of the 6D space. Additionally, the electron density is shifted along a parallel space direction. That means, in the atomic model, that split-atomic positions are highly expected. Even more, the splitting of the atoms along a 2-fold direction occurs perpendicularly to a radial in the cluster as a radial direction is always directed along a 3-fold and a 5-fold axis.

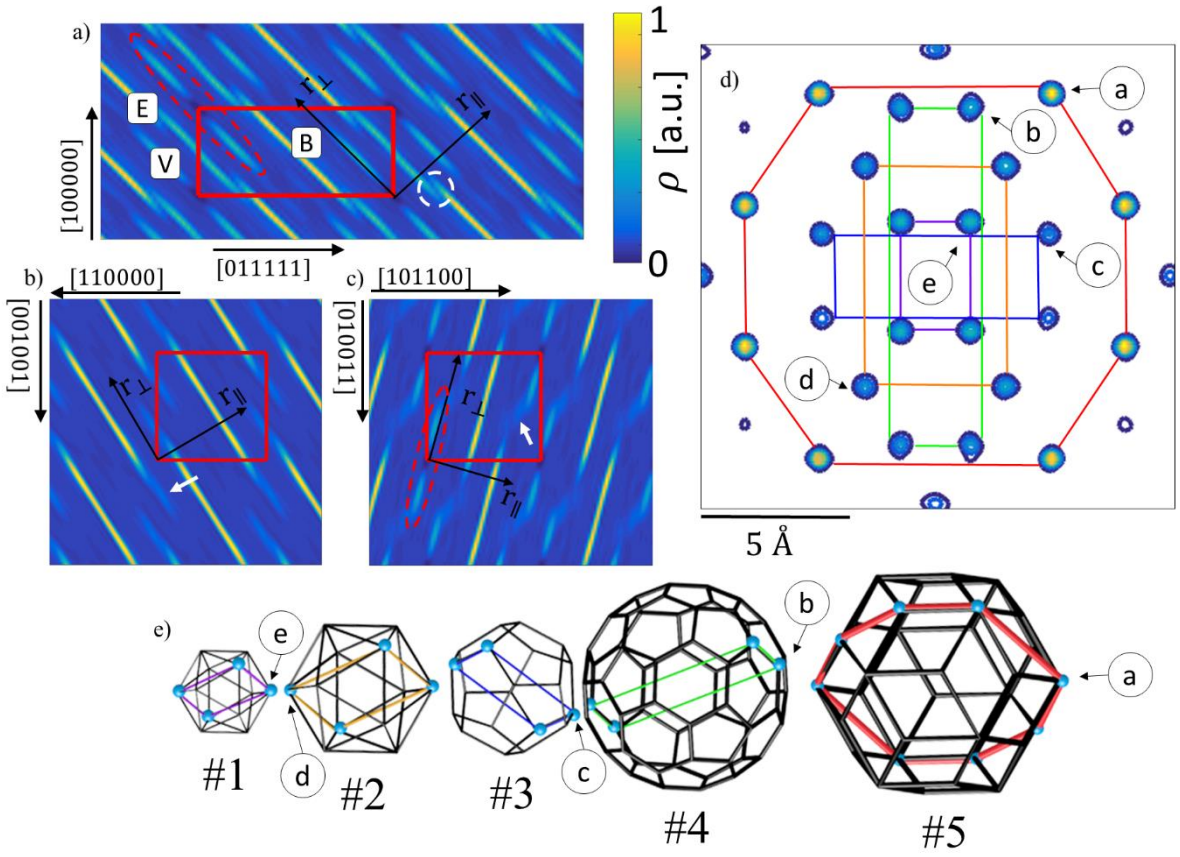

Figure 18. The 2D high-symmetry sections through the 6D electron density, obtained by the phase retrieval, containing a) 5-fold, b) 2-fold and c) 3-fold axes both in parallel space ($\mathbf{r}_{\parallel}$) and perpendicular space ($\mathbf{r}_{\perp}$); d) the section through the RTH cluster centre showing the pattern characteristic for the Bergman cluster. All the five shells are shown in e) as a 3D object. The plane section through each shell is marked with the same colour in d) and e) for a guidance.

In order to further explore the *ab initio* structure solution, an extended 2D section through the 3D electron density is presented (Fig. 19). The area of 90×90 Å^2 was calculated perpendicularly to one of the 2-fold axis. Such an orientation of the section allows to find the location of clusters easily. Three patches of the electron density were selected and magnified for the further discussion.

The top patch 1. in Fig. 19 shows a very clear, undistorted electron density distribution. The high concentration of the density occurs at the sites corresponding to the nodes of the #5 shell of the RTH cluster. Those are the Tm atom positions. Inner shells are also occupied by rather heavy element like Zn or Zn/Tm mixed atom. The cluster center in this case is empty, confirming the result of the ZnMgHo [164].

The patch 2. shows two clusters, 'A' and 'B' linked together by the short *b*-linkage with a length of 8.9 Å. The intersection of two RTH clusters along the short *b*-linkage forms a rhombic dodecahedron

with small pyramids on top and bottom, represented in Fig. 19 both in the form of 2D section and a 3D visualization. Such a linkage is not observed in the approximant crystals and does not appear in a set of the 12-fold sphere packing vertices, therefore the traditional model that constituents the cluster approach that was used for the Tsai-type CdYb iQC cannot incorporate such a linkage. Interestingly, the cluster center in both clusters is not empty and a rather heavy atom is occupying this site. It is however not the feature of the short *b*-linkage, but those two presented clusters form also the *a*-linkage that is shown in the patch 3. The presence of the central atom caused a deformation of the inner sites generated by the small icosahedron (#1 shell) along a 5-fold direction. Site 'a' of the cluster 'A' is generated by the OD_E, which was shown to intersect with the OD_B in Fig. 18 a) along a 5-fold direction, leading to the phason flip. The site 'a' is co-shared with the neighboring cluster 'B'. This site in the cluster 'B' is part of the #5 shell which is generated by the OD_B. That is exactly the phason flip site from Fig. 18 a) marked with a white dashed circle. The same reasoning applies to the site 'b'.

In the last patch 3., the *a*-linkage along a 5-fold direction is shown. The intersection of two RTH clusters forms a rhombic icosahedron. The formation of the *a*-linkage is visualized in 3D. The *a*-linkage appears in the 12-fold vertices of the AKNt, but according to the standard practice it is removed from the cluster model as it creates too short interatomic distances and has not been seen in approximant crystals. Indeed, the position, which is created by the #5 shell of the cluster 'D' and by the #1 shell of the cluster 'C' are very close to each other but do not overlay (position 'c' ('d')). Consequently, the distortion of the electron density along a 5-fold direction is created. What interesting is that once again the centres of the clusters connected via the *a*-linkage is occupied by rather heavy atom. This atom can be both interpreted as a central atom or the atom occupying the node of the #2 icosahedral shell of the neighbor cluster. The other interesting position is the site 'e' occupied by a heavy atom. It can be interpreted as the position generated by the node of the triacontahedron 'C' or the node belonging to the #3 dodecahedral shell from the cluster 'D'. That means that the Tm element can be found either on the #5th triacontahedral shell or on the #3 dodecahedral shell.

A separate figure is dedicated to the *b*- and *c*-linkages (Fig. 20). Due to the existence of the *a*-linkage Tm elements were said to occupy the #3 dodecahedral shell. However, it is not the only reason. As it was pointed out in Fig. 20 a) the *c*-linkage (12.2 Å) also contribute to co-sharing atoms from the #5 triacontahedral shell with #3 dodecahedral shell. Atoms 'a' and 'b' are mutually exchanged between two clusters forming the *c*-linkage. Contrary to the *a*-linkage the positions overlay ideally, and no atomic splitting is generated. Nevertheless, it can be concluded that Tm atoms are occupying both #3 shell and #5 shell as a by-product of the *c*- and *a*-linkages.

Interestingly, the *b*-linkage (14.1 Å) also causes a small atomic disorder in the structure. The atomic sites 'c' in Fig 20 b) are part of the #4 shell of the cluster 'D'. The same atoms should appear in the cluster 'C'. However, due to the short distance, they are absent. What remains is a weak electron

density enclosed with a dotted line. We can expect the atomic sites ‘c’ to form a split atomic position as well. Positions ‘d’ are co-shared by clusters, but no disorder is created.

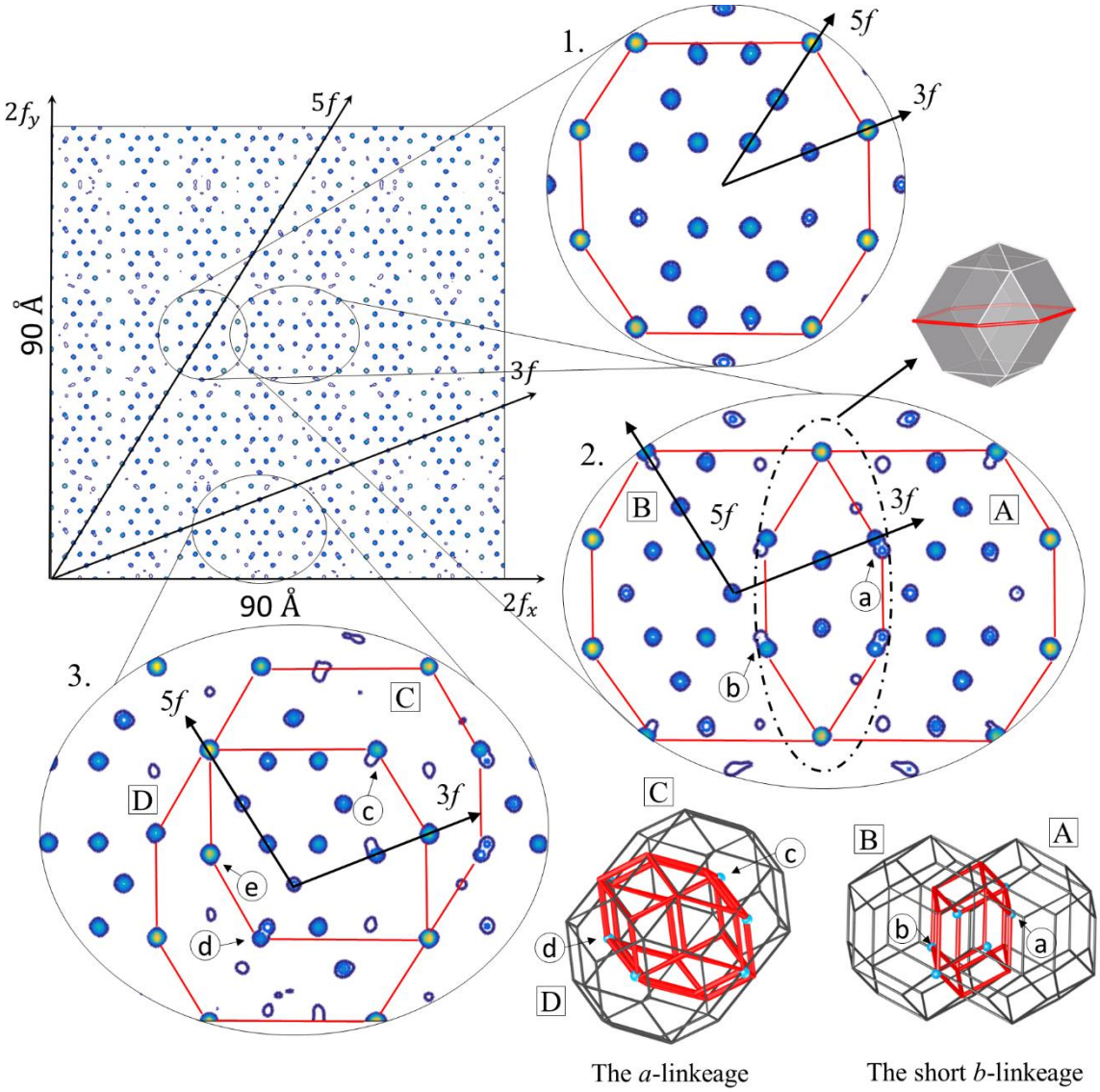

Figure 19. The 2D section through the 3D electron density. The area of 90×90 Å^2, calculated in the plane perpendicular to a 2-fold direction is shown. Three patches are highlighted: 1. - the undistorted Bergman cluster; 2. - the short *b*-linkage; 3. – the *a*-linkage. The 3D visualization of both linkages is also presented.

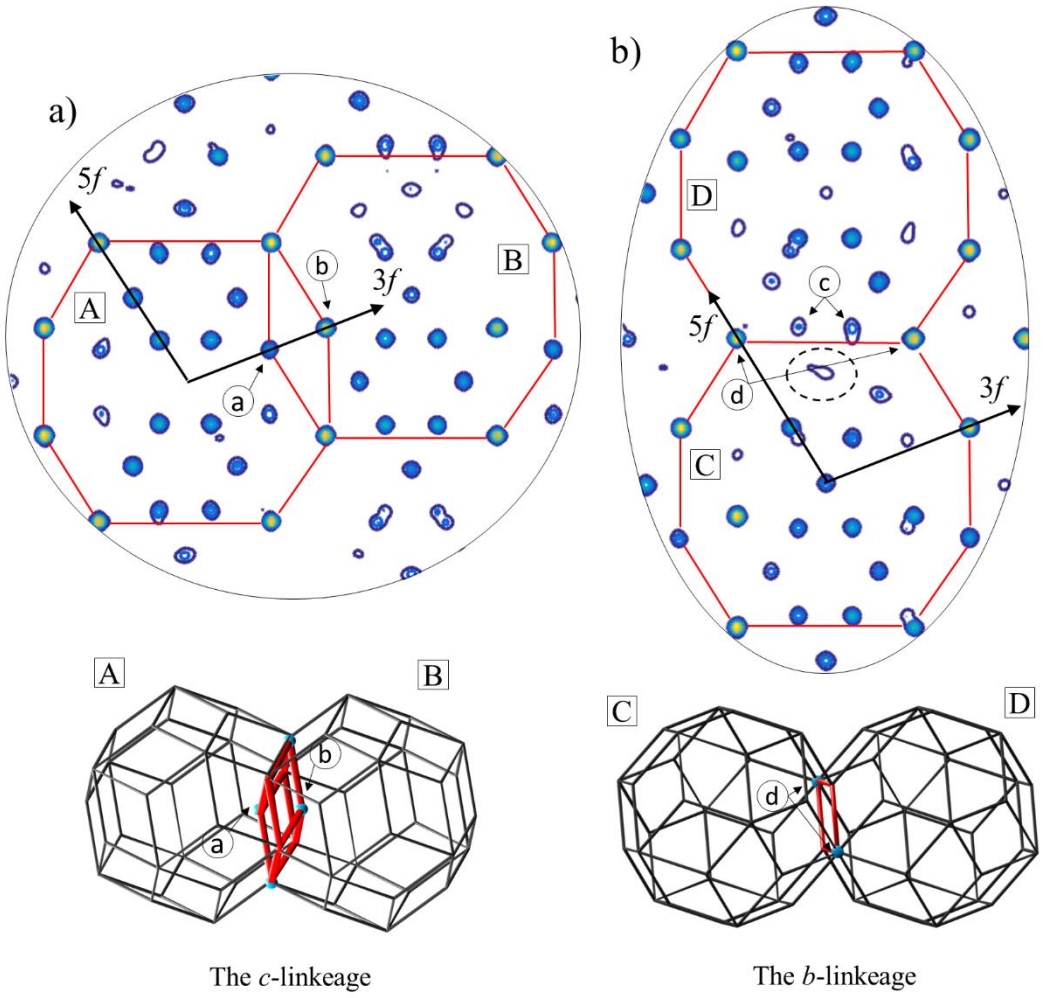

Figure 20. a) The section through the *c*-linkage occurring in the structure of i-ZnMgTm with RTH clusters marked with a red line. The 3D visualization is provided. Atoms 'a' ('b') are co-shared by the #5 shell of cluster 'B' ('A') and #3 shell of cluster 'A' ('B'); b) The section through the *b*-linkage occurring in the structure. The indication of the split atomic sites 'c' is made.

In order to show the splitting of the atomic sites along a 3-fold and a 2-fold direction, the isosurface with a contour plot were calculated (Fig. 21). In Fig. 21 a) the splitting of the one of atoms belonging to the #3 dodecahedral shell is shown. The site 'a' is located on a 3-fold axis directed from the center of the cluster, which part is shown in the picture (red line). Fig. 21 b) presents the top view of the contour plot, along a 5-fold axis. The splitting is shown to occur along a 2-fold axis, perpendicularly to the radial direction of the cluster. Since the OD_B generates the positions on the nodes of the dodecahedron, this splitting corresponds to the situation indicated by the white arrow in Fig. 18 b). Fig. 21 c) shows the splitting of the atomic site 'b', belonging to the #2 icosahedral shell. In Fig. 21 d) the

splitting is shown to occur along a 3-fold axis. This is the splitting indicated by the white arrow in Fig. 18 c), occurring for the OD_V, which generates the positions on the #2 icosahedral shell.

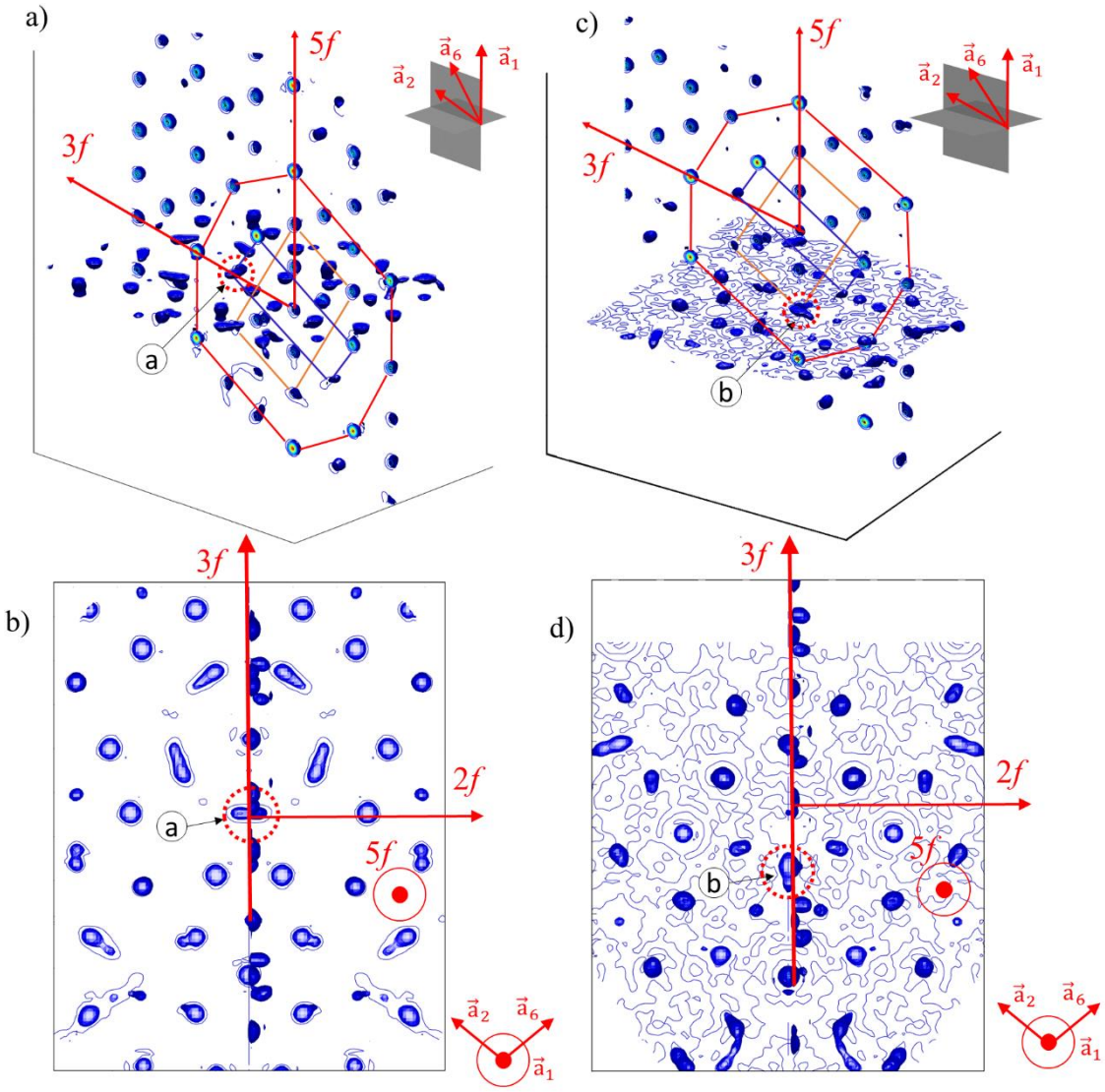

Figure 21. The isosurface plot in two perpendicular planes with the contour slice plot (in the vertical plane) for the 3D electron density map. a) The isometric view with the position 'a' indicated by an arrow and dotted circle and recognised as the split atomic site on the dodecahedron (section through the dodecahedron marked with dark blue line). The splitting occurs perpendicularly to the cluster's radial direction which is a 2-fold direction and corresponds to the position indicated by the white arrow in Fig. 18 b). The outline of the RTH cluster is drawn with the red line. Additionally, the outline of the outer icosahedron is marked with an orange line b) the top view of a); c) The isometric view with the position 'b' recognised as the split atomic site on the outer icosahedron along a 3-fold direction. Such a split position corresponds to that indicated by the white arrow in Fig. 18 c). The contour of the RTH cluster

is drawn with the red line alongside the contour of the #2 icosahedron that is marked with an orange line and the contour of the #3 dodecahedral shell marked with a dark blue line; d) the top view of c). The specific directions are indicated with red arrows. The positions of the planes in which the electron densities are calculated in the isometric views in a) and c) are pictured with grey planes together with the orientation of the vectors in the icosahedral setting.

4.4 The structure model

The infinite structure model of the Bergman ZnMgTm iQC was constructed by ascribing the atomic decoration to two golden rhombohedra in the AKNt. Even though, the AKNt is indirectly used in all the models of iQC i.e. provides the 12-fold vertex environment and defines the atomic decoration of the interstitial part, it has never been utilized as a quasilattice for which the prototiles are building blocks of the structure. The main reason why it was never used is the unique decoration of rhombohedra cannot be determined in real structures [176, 177, 178]. To our knowledge, the latter statement has never been tested, nor proven for the inflated tiling. PI QCs obey the τ^3 scaling rule [144]. Therefore, the edge-length of the golden rhombohedra can be inflated from a regular 5.13 Å to 21.7 Å. We faithfully decided to try this approach and carry out the structure modelling. Of course, we worked with a strong assumption that the structure is well modelled by the decorated AKNt, which is τ^3 inflated.

To find the decoration of the inflated rhombohedra, the electron density in randomly selected rhombohedra of the AKNt was calculated (Fig. 22). The electron density is subjected to small discrepancies between selected rhombohedra due to the limited amount of diffraction data and the phase retrieval, which although is very satisfying, cannot be considered complete. The complete reconstruction would be possible only with the infinite number of diffraction peaks and that is impossible for obvious reasons. In order to minimalize the electron density variations, the average electron density was calculated over chosen rhombohedra. That helped to obtain a good approximation of the atomic distribution inside rhombohedral units. It must be stated, that the decoration of each rhombohedron was repeatable. Therefore, the τ^3 scaled rhombohedra can be considered as proper building blocks of the structure. The maxima in the electron density correspond to the real space atomic positions. Approximately 800 positions were determined for AR and 500 for OR. Such a large number of atoms in the building blocks of the structure would be impossible to refine as only 3010 diffraction reflections are at disposal. The number of parameters was reduced by using the symmetry of each rhombohedron. By applying the 3-fold rotation and mirror symmetries the volume of rhombohedron, which is considered independent in a course of the structural refinement, was reduced by the factor of six. For the final model 148 atomic positions in AR and 104 for OR were used.

The last information required to finish the preparation of the initial model is the elements distribution in the rhombohedra. Fortunately, Zn, Mg and Tm differ significantly in term of the atomic

scattering factor for X-rays therefore they can be rather clearly distinguished in the electron density map. In Fig. 22 we have plotted histograms of the calculated electron density for the found maxima. For both AR and OR three Gaussian-like distributions can be found. Each one corresponds to the specific element that is: the first Gaussian, closest to the origin, counts instances of Mg, which is the lightest element with the atomic number $Z = 12$. The next broad distribution is assigned to zinc with $Z = 30$. It is also the largest distribution as the content of Zn in the iQC is around 69%. The smallest distribution belongs to Tm, which is also the heaviest element in the structure with $Z = 69$. The histogram is normalized. Three Gaussian functions were fitted to the histogram plot. The type of atom is assigned to each site by the condition of the intensity in this position. If its intensity lies within 2σ from corresponding Gaussian function's maximum the element is ascribed unambiguously and is not subjected to the further refinement. If the intensity lies between distributions corresponding to particular elements this position is left as mixed site and the ratio of occupation is refined. That procedure led to the initial composition of $Zn_{68}Mg_{24}Tm_8$, which is in a good agreement with the experiment.

The crystallographic *R*-factor of the starting model is equal to 35%. That value, even though large for inorganic crystals, does not negatively verify our model. Firstly, at this stage of investigation the model was not refined. Secondly, the phason disorder is known to be a dominant factor affecting the intensity of the diffraction peak. Lack of the phasonic correction can lead to $R = 27\%$ even though the atomic model of the QC is very good [83].

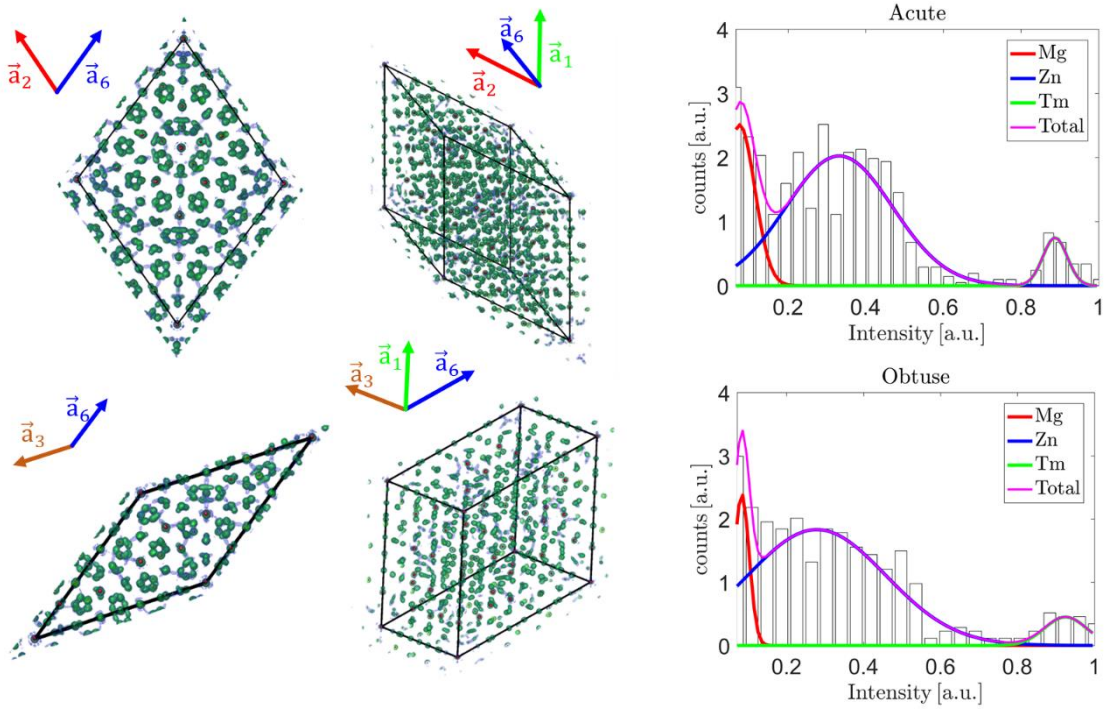

Figure 22. The visualization of the isosurface electron density inside of the prototiles of the AKNt. The green (red) isosurface was plotted for 1/10 (1/3) of the maximal intensity. Two orientation for each

rhombohedron are shown. The orientation is expressed by arrows directing toward base-vectors of the icosahedral setting. The method of finding the atomic sites based on the electron density is shown. The algorithm finds the maxima which are assumed to be the centres of atoms for the initial model of the iQC. The atomic elements are ascribed to each site based on the distribution intensity in this site. Three Gauss distributions correspond to three elements found in the sample of ZnMgTm alloy. The strongest intensity is ascribed to Tm, whereas the weakest is Mg.

4.5 The structure refinement

The structure solution and refinement were based on the real-space modelling of atomic positions. The atomic elements were assigned to specific positions in the rhombohedra and later, by assembling rhombohedral units to form the AKNt, a whole structure in physical space was recreated. The real-space structure refinement, based on the average unit cell (AUC) approach, that is known to work exclusively in the physical space, was previously used for decagonal structures [127, 82]. Its main principle is the construction of the atomic distribution function [132, 179]. The distribution arises from projection of all positions on the periodic, reference lattice. In practical application, only the reference vertex of the rhombohedra must be projected because positions of atoms are related to that chosen site by vector translation. The AUC approach was never used for the structure refinement of the iQC, therefore a whole methodology including the code for the structure refinement had to be developed from scratch.

The refinement of the structure was conducted with the use of the own code written in Matlab software environment. The library *fmincon* was used to optimize the parameter of the structure with the interior-point algorithm as a solver. The chosen solver satisfies bounds at each iteration and does not have to operate on full matrices what saves time, especially for problems with large number of parameters. The structure factor calculation is based on the tiling-and-decoration scheme, where the geometric part of the structure factor is separated from the atomic part [126]. The geometric part is the Fourier transform of the distribution related to one vertex of each rhombohedra, that was selected as a reference site. The atomic positions are given exactly with respect to the coordinates of the reference site. The geometric component is multiplied by the sum of the plane waves scattered over each atom, multiplied by the phononic Debye-Waller factor and the atomic scattering factor.

In the structure refinement, 763 free parameters in total were refined. Those include: atomic coordinates, phononic atomic displacement parameters (ADPs) (isotropic), phasonic ADP in a general Debye-Waller formula [152, 80] (one parameter for a whole structure), extinction parameter [180] and a scale factor between experimental and calculated structure amplitudes. Additionally, for the mixed atoms the partial occupation probability for each element was refined, with the restriction that all have to sum up to 1. Since many atoms of the model are placed on the edges or the faces of the reduced units

of rhombohedra, the coordinate positions of those atoms are fixed and are not subjected to the action of the optimization algorithm. Parameters are refined against 3010 diffraction peaks what makes the reflections-to-parameters ratio ~3.9. The given ratio, however low for an inorganic structure, allows to perform the structure refinement. The number of parameters is quite large due to the large size of rhombohedra. The reduction of the size of rhombohedra is not possible since the model is restrained by the τ^3 scaling and a regular size of rhombohedra cannot be decorated uniquely. The larger size (τ^6 inflated one) would be irrational from the numerical point of view, since the volume of the rhombohedra would grow τ^9 times with respect to already inflated tiles and the number of atoms would grow to tens of thousands.

After the structure refinement, which resulted in a wonderful $R = 9.8\%$ no short atomic distances are observed, except for the high-symmetry sites with partially occupied atomic sites (Fig. 23). We have allowed for only small shift of atom from the original position (< 1Å in each cycle of the refinement program) what restrain the atoms from freely slide within the structure. We can observe a few instances of Zn/Mg mixed occupancies, Zn/Tm and very few where all three elements are found to be mixed, however mostly occupied by Zn/Mg and trace-amounts of Tm. Such mixing is not unusual in Bergman phases and is observed for approximant crystals in ternary ZnMg based alloys [181]. The final composition after the refinement was concluded to be $Zn_{66.7}Mg_{25.1}Tm_{8.2}$ with $e/a = 2.08$ and a point density equal to 0.062 Å^{-3}. It is in an acceptable agreement with the experiment. Nevertheless, there is a significant deviation from the experimental composition, especially considering Zn to Mg ratio, which does not affect e/a ratio. Such a deviation is rather common not only for ZnMg based QCs but also for their approximants. The discrepancy up to 3 at.% is not rare. The question is whether a significant disorder observed in those structures, both positional and chemical in nature, is an intrinsic component that should be accepted [182].

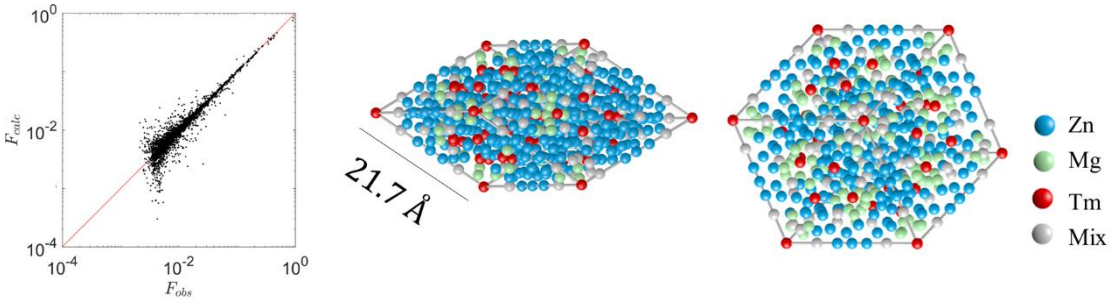

Figure 23. The correlation plot F_{calc}vs F_{obs} (left). The $R = 9.8\%$. The atomic decoration of two rhombohedra of AKNt after the refinement (right). The edge-length is equal to 21.7 Å. Tm atoms are located in the vertices of rhomboidal faces and form a rhombus in the mid of each face. Those are related by τ^3scaling property. Only 1/6$^{\mathrm{th}}$ of each rhombohedron is refined.

4.6 The RTH covering

The structure was refined within the scheme of the atomic decoration of golden rhombohedra forming the AKNt. The standard method of the modelling of the iQC and approximants is the cluster-based approach where the local atomic arrangement is expressed by three known so far families of clusters. It is interesting to see how our refined structure corresponds to the cluster model.

It is intriguing that all the atoms in our model correspond to some sites of the Bergman cluster. In fact, by covering the inflated rhombohedra with RTH clusters, we can assign every single atom to RTH cluster forming a kind of quasiperiodic covering. A covering is usually discussed for decagonal QC e.g. the Gummelt cluster has such property [183] but it was never elaborated nor implied for an iQC. That feat is not possible for the 12-fold sphere packing based model of iQC. If *b*- and *c*-linkages are allowed exclusively, the interstitial part of the structure always arises. In our case such a distinction between RTH cluster sites and interstitial structure is unnecessary. It would be even inappropriate since there is no condition that would allow us to select the clusters that are considered 'proper'. It is caused by the existence of the *a*-linkage along a 5-fold direction and the short *b*-linkage along a 2-fold direction. Those linkages are excluded from the cluster-based approach as they create too-short interatomic distances, what was shown in §4.3 and are never seen in the approximant crystals. The length of each linkage, appears in our model, is the following. The length b of the *b*-linkage is equal to $a(4+8/\sqrt{5})^{1/2}$=14.1 Å. The length c of the *c*-linkage is equal to $b\sqrt{3}/2 = 12.2$ Å. The length of the *a*-linkage is equal to the edge-length of original (not inflated) rhombohedra, that is 5.13 Å. The short *b*-linkage can be calculated from the *b*-linkage by subtracting the original lattice constant, resulting in 8.9 Å.

The short linkages create split atomic positions that have to be dealt with. In our model, for the way the atomic positions were identified by looking for the maxima in the electron density, one of two split atomic maxima can be unoccupied as the algorithm removes one maximum if two are too close to each other. Those positions are e.g. the atoms belonging to the icosahedron from the #2 icosahedral shell of clusters located on the edges of rhombohedra (marked 'a' and 'd' in Fig. 24). That does not worsen the model, but high phononic ADPs for such positions are expected (see §4.8.3). The site 'a' is unoccupied because it would be too close to the site 'b'. The same reasoning applies to the site 'd'. The site 'b' and 'c' exhibit a substantial freedom of movement along a 5-fold direction, that is reflected in the electron density map. That is the phason flip site. Due to the steric condition the site 'a' can be unoccupied, as it is presented, or occupied depending on how far the atom 'b' is from the cluster center. We can see that in the electron density map the site 'a' could be partially occupied or occupied by a light element, but due to the low electron density it remained empty in the model. Contrary to the site 'a', the site 'd' shows no indication of the atom (Fig. 24 right).

There is another site that deserves some attention. The site ‘e’ is shared by the #1 shell of both interacting clusters. The question is whether this site creates short distance that should be filled by a split atom. In the electron density map, there is no trace of the smearing along 5-fold direction. However, due to the maneuverability of the sites ‘c’ and ‘b’, there is a possibility that the site ‘e’ will be able to glide along 5-fold axis. Nevertheless, in the model it is occupied by one atom.

The other intriguing question is that whether the cluster center is occupied by an atom or not. In our model the occupied center site is created by the existence of the *a*-linkage. The atom occupying the node of the icosahedron from the #2 icosahedral shell is located right where the center of the nearby cluster is located. That is very well represented in Fig. 24, both in a refined structure model and an electron density obtained from the *ab initio* phasing. Only the clusters located on the long body-diagonal of the AR are not exhibiting the occupied center as they are connected by the *c*-linkage and do not exhibit any *a*-linkage. However, they are linked by the short *b*-linkage with neighboring clusters.

Our refined model shows all the features that were also found in the *ab initio* structure solution. At this point we would like to state that at the very early stage of the iQC structure solution, there was an attempt of constructing the iQC with two types of the RTH clusters only: small one and big one [184]. The model was derived for the cubic R-Al_5CuLi_3 approximant of the AlCuLi QC. The crucial difference with respect to our approach is we do not include the second, smaller rhombic triacontahedron in-between large RTH clusters. All the shells of RTH covering derived from our model can be seen in Fig. 25 for the asymmetric part of rhombohedra.

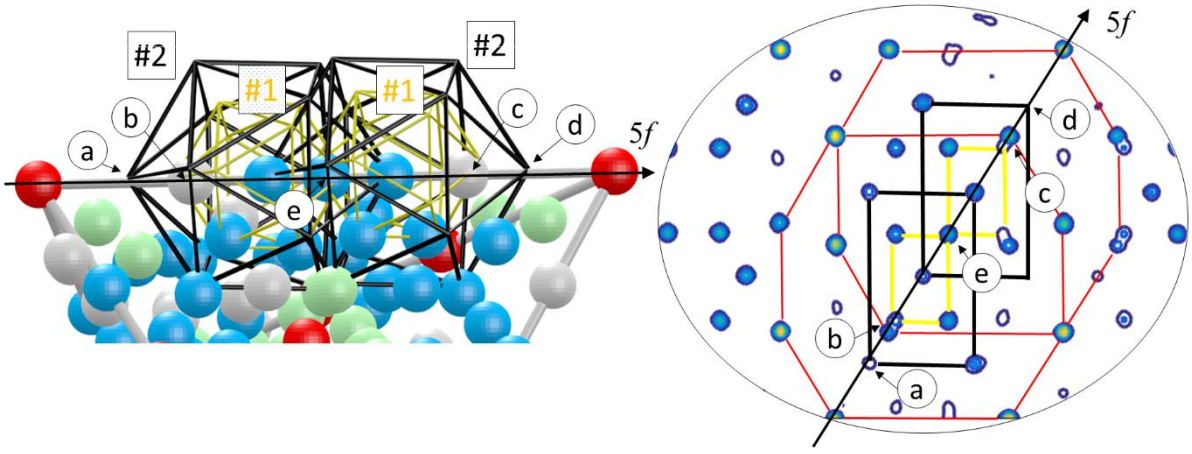

Figure 24. The formation of the *a*-linkage in the asymmetric part of the OR. The #1 shell (yellow line) and the #2 shell (black line) of linked clusters are shown. The position ‘a’ (‘d’) is unoccupied due to the close vicinity of the atom ‘b’ (‘c’). The site ‘a’ shows some non-zero electron density (right) but in the refined model this site is unoccupied. The position ‘e’ is a potential split position created as an overlay of two neighbouring #1 shells. The rhombic triacontahedral shell was not plotted in the atomistic model as it would make a picture indistinct.

10 sites in the asymmetric part of the AR and 7 sites in the OR were found to host the RTH cluster. Those sites are listed in Table 4. To create this list, we have used the known relation for τ-scaling: every number can be expressed as equal to $p + q/\tau$, where $p, q \in \mathbb{Z}$. The list shows (p, q) values of the sites in the rhombohedra.

Table 4. RTH clusters positions in two rhombohedra: AR and OR. The notation gives (p, q) values of the reduced coordinates of cluster centres. For example, the position r of the cluster centre is equal to $r = X\mathbf{f}_1 + Y\mathbf{f}_2 + Z\mathbf{f}_3$, where $\mathbf{f}_1, \mathbf{f}_2, \mathbf{f}_3$ are vectors spanning edges of the rhombohedra. For the AR those vectors are $\mathbf{a}_1$, $\mathbf{a}_2$, $\mathbf{a}_6$ respectively and for the OR $\mathbf{a}_1$, $-\mathbf{a}_3$, $-\mathbf{a}_6$.

Rhombohedron Type	X	Y	Z
AR	(0, 1)	(0, 1)	(0, 1)
	(1, -1)	(1, -1)	(1, -1)
	(0, 1)	(0, 0)	(0, 0)
	(1, -1)	(0, 0)	(0, 0)
	(2, -2)	(2, -3)	(2, -2)
	(-1, 3)	(-1, 2)	(-1, 2)
	(1, 0)	(0, 0)	(0, 1)
	(1, 0)	(0, 0)	(1,-1)
	(1, 0)	(1,-1)	(1, 0)
	(1, 0)	(0, 1)	(1, 0)
OR	(0, 1)	(0, 0)	(0, 0)
	(1, -1)	(0, 0)	(0, 0)
	(1, 0)	(0, 0)	(0, 1)
	(1, 0)	(0, 0)	(1, -1)
	(1, 0)	(1, -1)	(1, 0)
	(1, 0)	(0, 1)	(1, 0)
	(0, 1)	(1, -1)	(0, 1)

To illustrate the refined structure, in Fig. 26 the 2D projections of the atomic arrangement along 2-, 3- and 5-fold directions are shown. The RTH cluster covering and the AKNt are plotted over the generated atomic sites for guidance. Since the cut through the AKNt perpendicularly to a 5-fold direction is known to form a Penrose tiling it is not surprising the 5-fold section exhibits a similar atomic arrangement as the decagonal QCs.

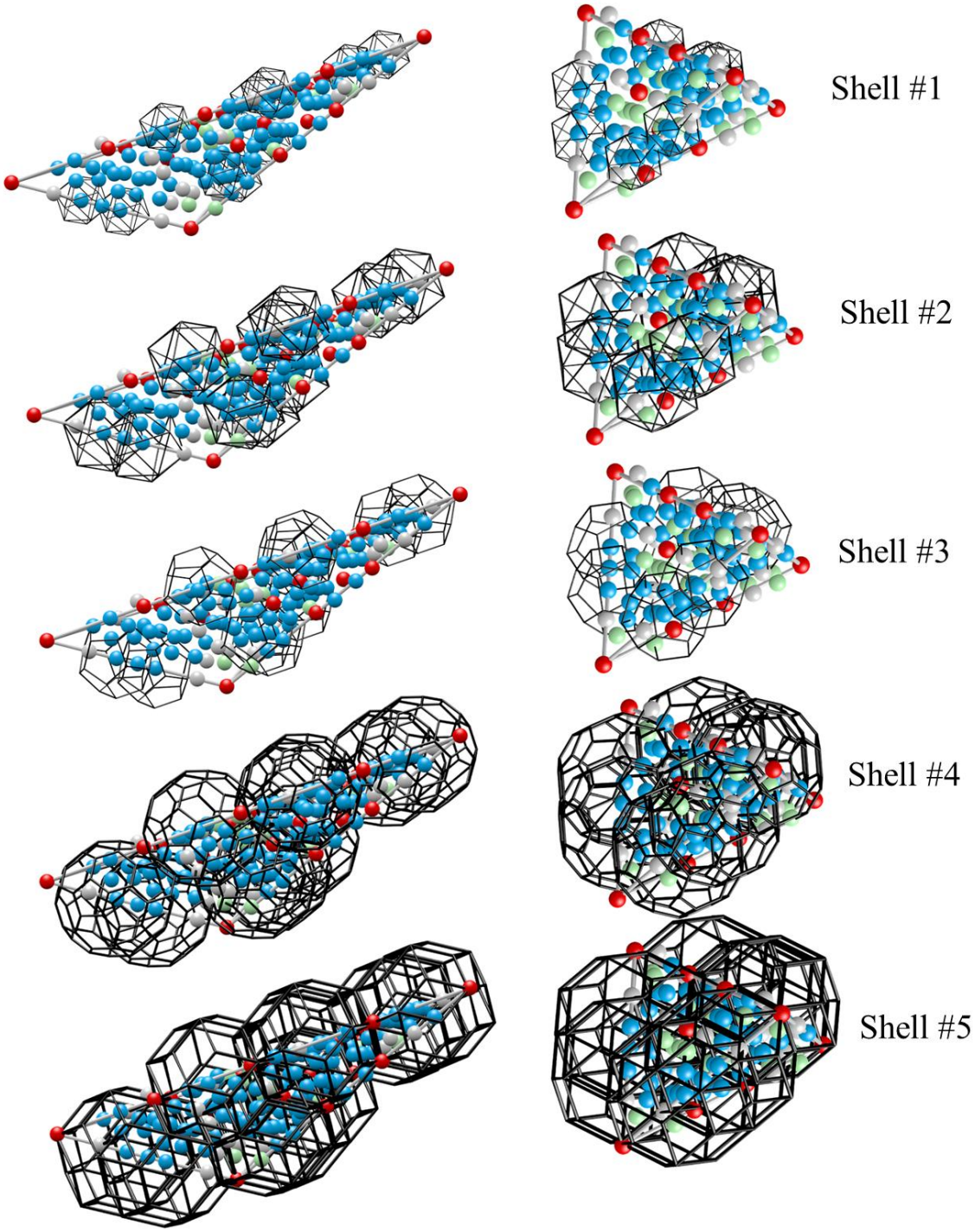

Figure 25. All the shells of the Bergman cluster plotted in reference of the asymmetric part of AR (left) and OR (right). The colours represent atoms the same as in Fig. 23. Each of the atoms belongs to one of the cluster's shell.

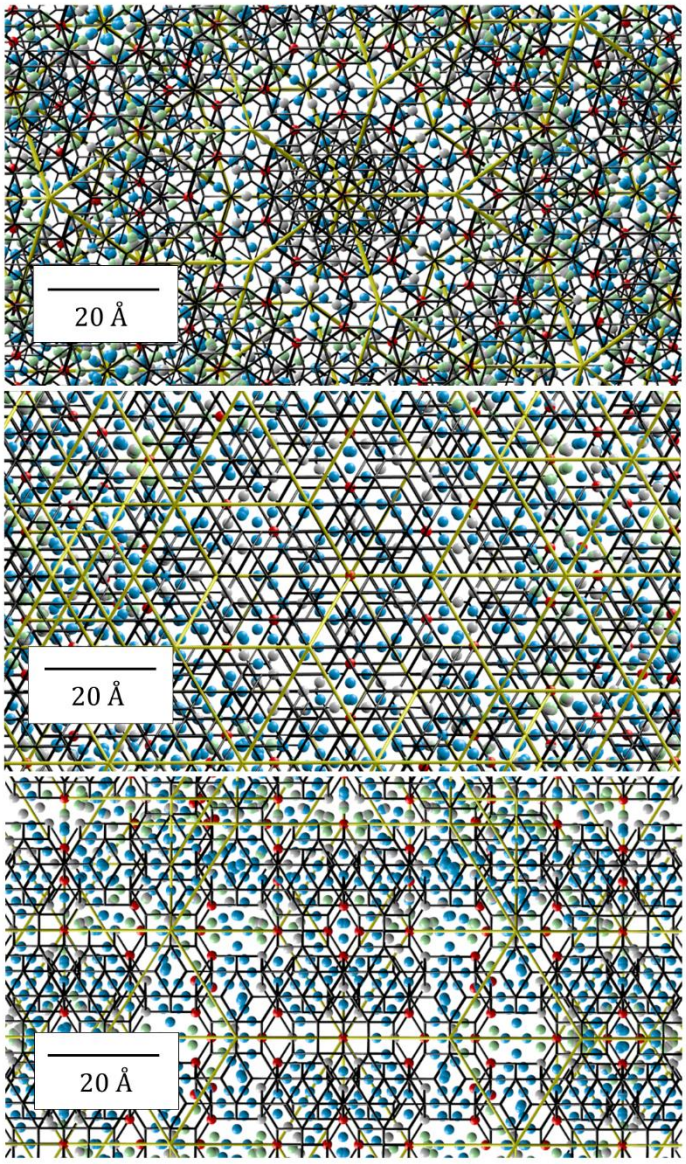

Figure 26. The ZnMgTm iQC structure projected along 5-fold (top), 3-fold (mid) and 2-fold (bottom) directions. The thickness of the projected structure is equal to 2 Å. Black bonds define the frame of the RTH cluster, whereas the yellow bond indicates the edges of the τ^3 inflated rhombohedra in the AKNt.

4.7 The higher-dimensional model

The traditional approach, with nD, involves modeling of the ODs located in the internal space being orthogonal to the physical space. Our model, even though based on the real-space, can be still lifted to the 6D space to compare our result with previous attempt on the Bergman-type QC. In order to lift the structure to 6D the large portion (>500 000) of the atomic positions was generated. All the

positions were represented as 6D vectors, where the physical space coordinates were derived from the structure itself and the internal space coordinates were assigned 0. It is due to the principle of the section method where the physical space coordinate is generated as an intersection of the physical space with the OD. That always occurs for the internal space coordinates equal to 0. After multiplying the 6D vector of each atom by the inverse projection matrix $\mathbf{W^{-1}}$ (inversion of the 3.10), the coordinates in the 6D space were found. The coordinates were then reduced to one 6D unit cell by the modulo 1 operation. Every position of the generated structure was then assigned to the corresponding OD. The assignment is not deterministic because of the phason flip sites that allow for an atom to be ascribed to two different ODs with equal probability. The recreated ODs are plotted in Fig. 27, in comparison to their equivalents coming from the simple-decoration model [163]. The inner part of the OD_B generates Tm atoms in the structure. Tm is only located in that OD what corresponds well with the 5-fold section plotted in Fig. 18. In the OD_V the inner part is empty what also very well corresponds to the plot in Fig. 18 obtained from the *ab initio* phasing procedure. Those positions are related to the cluster centres in the body-diagonal of the AR. The OD_E is located at the low-symmetry site ($\bar{5}m$) what is also recreated in our model. The recreated ODs are resembling to those for the simple-decoration model in terms of size and shape, but the details are different. For instance, we can see unoccupied sites along 3-fold direction in the OD_V and OD_B. That fine structure corresponds to fine-tuning carried out by Yamamoto to solve the structure of AlCuLi iQC [104]. He additionally modified the simple-decoration model by removing the atom form the 12-fold vertices (empty centre in OD_B), and also removing some atoms inside of the rhombic dodecahedron laying on the mid-edges positions and putting atoms in off-edge-centre positions. However, the fine details of the ODs are different, e.g. we observe an aggregation of Mg atoms nearby 5-fold vertices in the OD_V, which does not occur in Yamamoto's model possibly due to its idealized decoration of off-centre mid-edges positions. In addition, our model is significantly more ordered chemically.

The last test of our model was the comparison between the calculated high-symmetry sections through the 6D space. The phases obtained from the refined structure served to calculate the electron density map using the experimental diffraction amplitudes and ones recovered from the model (Fig. 28). By calculating the residual electron density $|\Delta\rho| < 4\%\rho_{max}$ we can conclude that our model does not miss any significant amount of atoms in the structure. The comparison with other Bergman QCs is impossible since no other contemporary model of this QC exists.

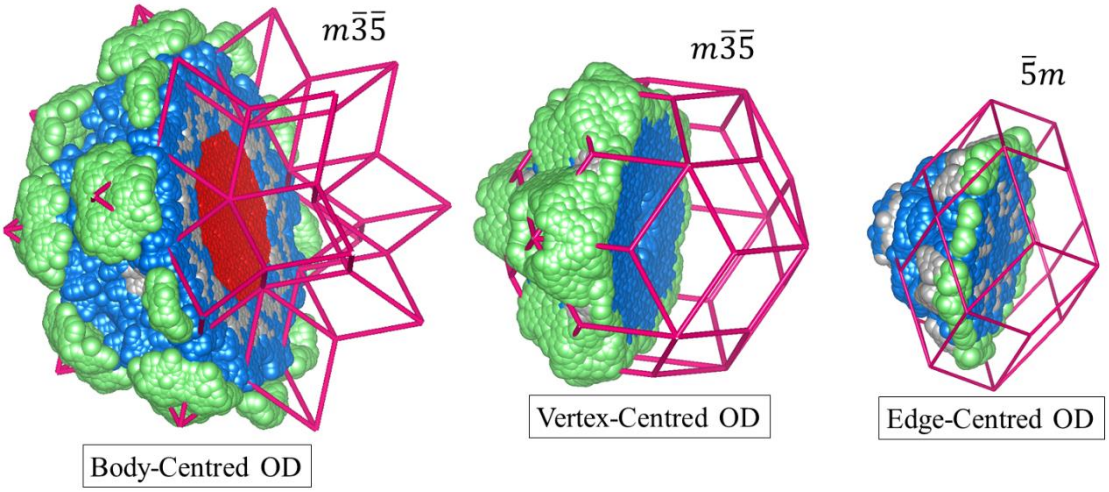

Figure 27. Three ODs of the ZnMgTm iQC lifted to the 6D space: the OD_B ($m\bar{3}\bar{5}$), OD_V ($m\bar{3}\bar{5}$) and OD_E ($\bar{5}m$). The Tm is accumulated only in the OD_B . The empty centre of OD_V is reproduced very well in the present model.

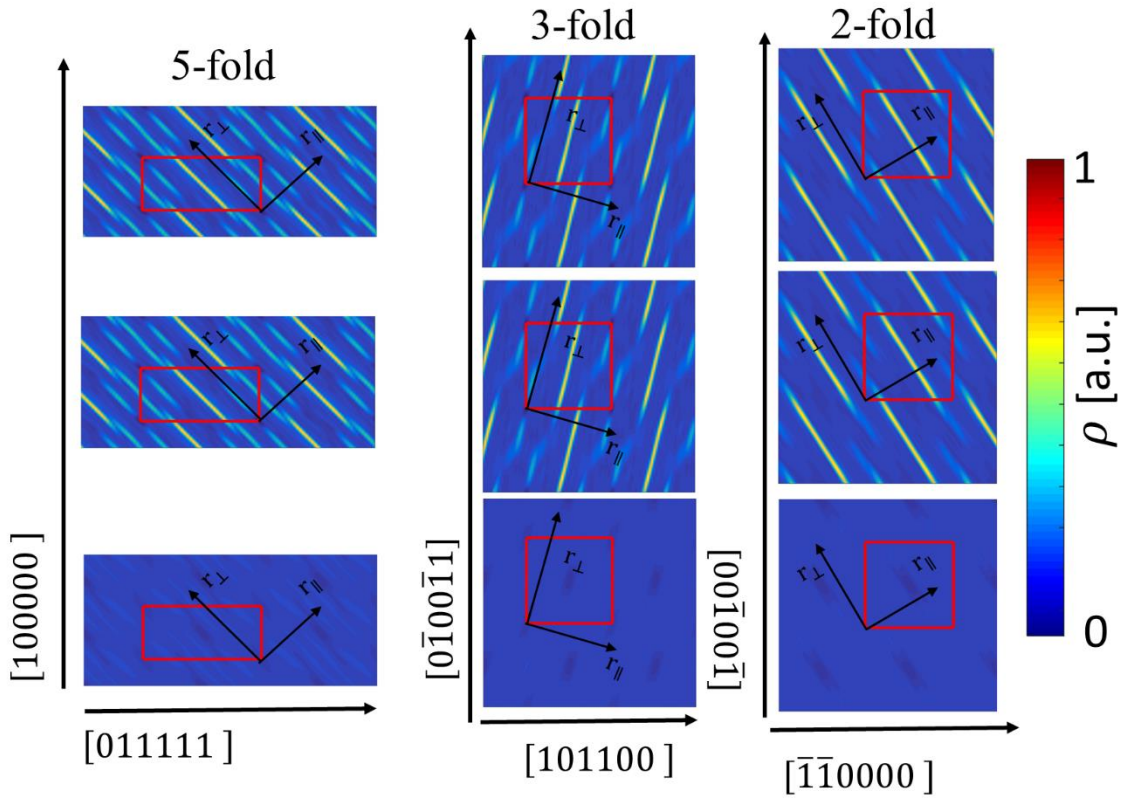

Figure 28. The high-symmetry 2D sections through the 6D space resulting from the Fourier transform of the experimental diffraction pattern (top), our model after the refinement (mid) and the

differential electron density map (bottom). The small residual density validates the correctness of the model. The red rectangle shows the 6D unit cell.

4.8 Discussion

4.8.1 Tiling approach vs cluster model

The model of the ZnMgTm Bergamn iQC was constructed in the tiling-and-decoration scheme, where two golden rhombohedra of the AKNt where chosen as building blocks of the model. This alternative to the cluster approach definition of the model was previously proposed based on the structure refinement of the 2/1 cubic approximant of the AlZnMg QC [185]. Unfortunately, the model was never finished, possibly due to the problem with finding a unique atomic decoration of AR and OR. We dealt with this problem by proposing τ^3 inflated rhombohedra as fundamental building blocks of the structure. The question someone could ask is whether such an approach is justified. In fact, that question is much deeper. So far, all the structure solutions of QCs make a presumption, that a long-range-order is well-approximated by the tiling. Sometimes, the assumption is explicit, when e.g. the structure of decagonal QC is built upon the Penrose tiling. In other situations, like in the case of iQCs, this assumption is hidden when only the subset of the 12-fold vertices of the AKNt is used to define the locations of cluster centres. Either way, the property of tiling is exploited, even though it is still unknown whether a particular tiling well characterizes the structure of QC. There is an attempt to generalize the tilings during the structure refinement of the decagonal QCs [122, 123], but such a work does not exist for the AKNt.

It is difficult to say, whether the cluster approach contradicts or is equivalent to the tiling approach in the context of the iQC. The solved structure exhibits the *a*-linkage and the short *b*-linkage which are absent in the cluster model. That would mean those two approaches cannot be equivalent. But what if the interstitial structure in the cluster model could be interpreted in terms of the clusters but with different atomic decoration? It is already known that atoms in the Tsai-type QC model form a Bergman cluster in the interstitial part [164]. If RTH clusters were assigned to cover the interstitial part, the additional linkages to known *b*- and *c*-, that were observed in our study, could naturally arise. We believe that a new model of the Tsai-type QC, based on the AKNt decoration would be beneficial for better understanding to the structure of iQCs.

4.8.2 Rare-Earth distribution

The location of Tm atoms in the present model is particularly important. The main reason is the magnetic properties of the Zn-Mg-Rare-Earth QC originate from the 4*f* electrons of the rare-earth ions, interacting via the indirect Ruderman-Kittel-Kasuya-Yoshida exchange [186, 187, 188]. So far, all the

research conducted on the Zn-Mg-Rare-Earth QCs shows the spin-glass-like behavior at low temperature and no clear indication of the long-range-order was reported. The nature of the frozen state is still under discussion [189].

One of the attempts on the theoretical investigation of the magnetic ordering in the FCI QCs was made by Sato [172], who proposed a model, where the rare-earths atoms are forming the network of edge-sharing dodecahedra with an edge length of 5.5 Å. However, the dodecahedral spin object does not explain why the spin correlation is terminated at the finite length. From the geometrical point of view, there is no reason why two adjacent dodecahedra should behave as isolated objects what was indicated by the author. Even though the question remains open, the dodecahedron as a spin object at least explains the magnetic diffuse scattering in the neutron diffraction pattern.

Recently, a FCI Bergman QC was investigated in the ZnMgHf in terms of the local atomic arrangement, especially dedicated to the positions of the Hf elements [190]. Similar to rare-earth elements, Hf seems to occupy the #5 rhombic triacontahedral shell of the Bergman cluster. In that study, the Hf elements are not only located in the 3-fold vertices of the RTH cluster, forming the dodecahedron, but also in the 5-fold vertices of the second cluster, forming the icosahedron. In principle, the existence of two types of clusters, differing by the preferential occupation of the high-symmetry sites by Hf, is the reason the face-centered ordering is realized. This new result could benefit for the better modelling of the magnetic properties in Bergman QCs, however, the complete structure solution of the FCI QC is still missing.

The result of the refinement of the PI ZnMgTm QC is in some way even more complex in terms of the Tm elements distribution than what is already known for the FCI phase. In Fig. 29 the distribution of atoms in the rhombic dodecahedron is shown focusing on the Tm atoms. All the Tm atoms are on the vertices of the rhombic triacontahedra (Fig. 29 a)), however not all the vertices are occupied by Tm atoms. It is difficult to point out a rule stating which site of the cluster is occupied. Both 3-fold and 5-fold vertices in the same cluster can be occupied at the same time, therefore the exclusion rule valid for the FCI does not apply. The #5 shell of the RTH cluster, beside Tm atoms, is occupied by Zn and Zn/Tm atoms. Some vertices are occupied by the Zn atoms solely. Such a not unique decoration of cluster sites originates from clusters overlapping along more than *b*- and *c*-linkages. The number of local environments of clusters grows when the *a*- and the short *b*-linkages are additionally allowed. Therefore, the cluster does not well represent the local chemical order.

The rhombic dodecahedron can be decomposed into 2 ARs and 2 ORs. Inside of the shown dodecahedron the short *b*-linkage (white clusters in Fig. 29 a), b) and c)) originates from two adjacent ORs, contributing to a formation of the small rhombic dodecahedron. In Fig. 29 d) – f) the decoration of the small dodecahedron, resulting from the intersection of two RTH clusters is shown. Tm atoms are gathered on the ring occupying the vertices of dodecahedron but the sites that lay on the plane perpendicularly to the linkage direction are occupied by Zn and Zn/Tm mix atoms (sites ‘a’ in Fig. 29

d)). These sites are generated by the overlay of the rhombic triacontahedron and inner icosahedron resulting in a split atomic position, as it was mentioned during the discussion of Fig. 19. The Zn/Mg and Mg atoms are located on the surface of the rhombic face, creating a split position along 2-fold direction Those sites are generated by the #4 soccer-ball polyhedral shell. Zn atoms form a hexagonal ring inside of the rhombic dodecahedron perpendicular to a 3-fold direction (Fig. 29 f)). In this ring sites 'b' are coming from the nodes of the #2 icosahedral shell, the sites 'c' are generated by the #3 dodecahedral shell and the sites 'd' are once again generated by the #4 soccer-ball polyhedral shell.

In Fig. 29 a) and b) not all the RTH clusters are plotted. For the sake of simplicity, only the clusters for which one of the faces lays on the face of the dodecahedron, forming a rhombus of Tm atoms are plotted. In Fig. 29 g) the 2D projection, along a 5-fold axis, of the Tm atoms in the structure is shown. The frame of the RTH clusters are plotted for guidance, to indicate each of the atoms belongs to the vertex of the #5 shell. The Tm-Tm distance is equal to the edge-length of the rhombic triacontahedron. Even though it was estimated to be 5.13 Å, the Tm-Tm distance in the presented cut through the structure is equal to 5.23 Å between the nearest neighbours and 8.65 Å between the second nearest neighbours atoms.

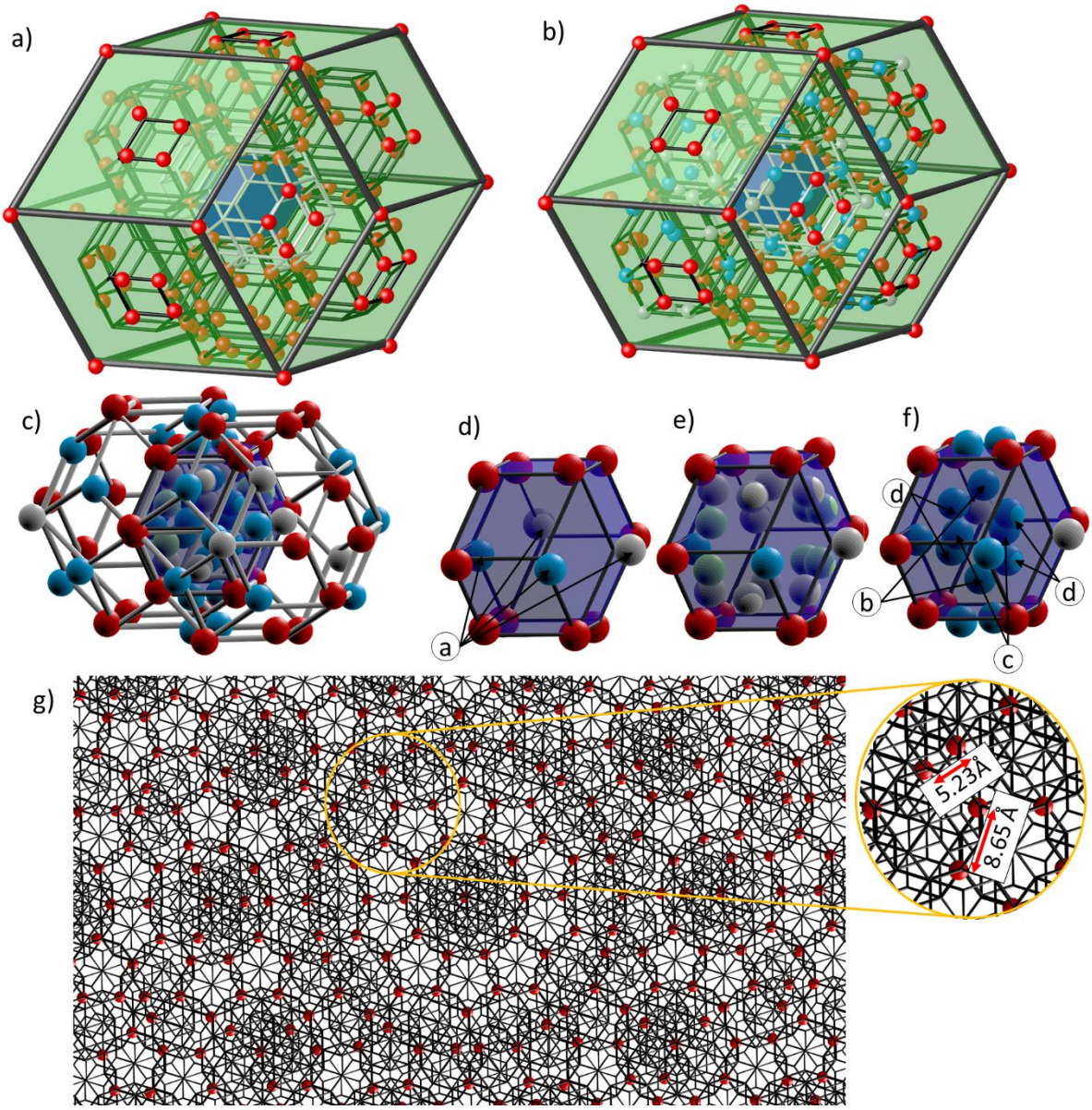

Figure 29. The atomic decoration of the dodecahedral motif in the refined structure of ZnMgTm Bergman iQC. The rare-earth atoms in a) and all the atoms in b), occupying the RTH's #5 rhombic triacontahedral shell are shown. The inner blue dodecahedron is τ^3 times smaller with respect to the green one showing the scaling property; c) the intersection of the RTH clusters inside of the dodecahedron, forming a short *b*-linkage. The atoms occupying the vertices of triacontahedron and all the atoms in the small dodecahedron are shown. In the d), e), f) the atomic decoration of the small dodecahedra, created by the intersection of two RTH clusters along short *b*-linkage is shown. d) shows the outer atoms, e) shows Mg and mix occupation atoms and f) shows Zn atoms inside of the small dodecahedron; g) the piece of the structure projected along a 5-fold axis presenting the distribution of Tm atoms. The 1Å depth is shown. The black bonds determine the frame of the RTH cluster.

4.8.3 Atomic ADPs and Disorder

The refined structure model of the ZnMgTm iQC shows rather small chemical and positional disorders, comparing to known Bergman QC approximants [181, 185]. The maximal atomic mean square displacement parameter $\langle u_{xyz}^2 \rangle$, related with *B*-factors according to the formula $B = 8\pi^2 \langle u_{xyz}^2 \rangle$, found in the refined structure is equal to 0.061 Å^2. It is estimated for one of the Tm atoms in the OR. Such a value is still almost three times lower than for the Zn18 position is the ZnMgZr 1/1 cubic approximant [181]. In Fig. 30 the atomic mean square displacement was plotted for each atom from the asymmetric part of AR and OR. We decided to thoroughly analyze the origin of large displacement parameter for atoms that exhibit $\langle u_{xyz}^2 \rangle > 0.05$ Å^2. The threshold was chosen arbitrarily for practical reasons just to present the idea why the large displacement occurs.

Seven atoms from AR satisfy this condition: 11, 44, 60, 72, 92, 114 and 145. Labels correspond to numbers given in Table S1. All the above listed atoms experience rather significant displacement in the course of the structure refinement. The shift is about 1 Å from the position in the initial model. In all the cases, such a substantial rearrangement is induced by the existence of the split atomic site that in our model was not assumed and instead only one fully occupied atom was considered. An atom 11 is Zn located at the face of AR. It is generated by the #4 soccer-ball polyhedral shell, that was indicated in Fig. 20 to exhibit a considerable disorder. Atoms 60 and 72 are Zn atoms generated by the #3 dodecahedral shell. The nodes of the dodecahedron become disordered due to the formation of the *a*-linkage. Atoms 92 and 114 are Zn generated by the #1 icosahedral shell. The strong displacement of the positions is justified by the *a*-linkage formed by RTH clusters. The behavior is similar to what was presented for the sites ‘a’ and ‘b’ in Fig. 24. Due to the absence of the atom in the site ‘a’, the atom ‘b’ has a space for mobility along a 5-fold direction. In the case of the atom 92 such a mobility occurs along the long-body diagonal of AR. Atoms 44 and 145 are Tm atoms located in the vertices of AR. Their potential maneuverability is caused by the absent atom in sites ‘a’ and ‘d’ in Fig. 24. In addition, these atomic positions were fixed during the structure refinement in the vertices of AR. Therefore, it might not be at their optimal position.

OR manifests less atoms that are significantly disordered in terms of ADPs. Only three atoms satisfy the above-mentioned condition: 15, 62 and 65. An atom 15 is Zn, generated by #2 icosahedral shell, forming the *a*-linkage. Atoms 62 and 65 are Tm atoms laying on the face of OR, sharing the same face of the #5 shell. Positions of Tm atoms can be affected by rather strongly disordered Mg atoms, generated by #4 soccer-ball polyhedral shell, that surround the atom 62. Any disturbance of the #4 shell will affect the #5 shell. Those two Tm atoms show two largest mean displacement parameters: 0.060 Å^2 for the atom 62 and 0.061 Å^2 for the atom 65. Also, three extreme Tm-Tm bond lengths are occurring in this patch: $\mathrm{Tm}_{62} - \mathrm{Tm}_{38} = 4.3$ Å, $\mathrm{Tm}_{62} - \mathrm{Tm}_{65} = 5$ Å and $\mathrm{Tm}_{38} - \mathrm{Tm}_{65} = 5.8$ Å.

It can be speculated what is better for the structure refinement - the explicit split atomic position or a single atom with a large displacement parameter. It is a difficult question especially in the context of QCs. Since the number of local environments in QCs is significantly larger than those in approximant crystals, principally in the Bergman QC where additional linkages are identified, it could be extremely tedious to assign all the split atomic positions correctly. Therefore, we decided not to introduce any more split positions and accept a little larger phononic ADPs.

Besides positional disorder, the structure model displays some chemical disorder. The mixed atoms are predominantly occupying the positions on the edges of rhombohedra, generated by the #1 icosahedral shell, where the *a*-linkage is formed. In this case Zn/Mg mix site is generated. Additional mixing occurs for atoms on the dodecahedral shell e. q. atoms 131 and 121 of the AR, forming the *c*-linkage. The site is co-shared with the vertex position of the triacontahedral shell. Those positions are Zn/Mg mixes with trace amounts of Tm atoms. It could however be the artefact of the refinement since the number of peaks to parameters ratio is low. The number of mix atoms are also occurring for the sites co-shared by the soccer-ball polyhedral and the most inner icosahedron in the short *b*-linkage. Such a site is e. g. the position 49 of the AR being occupied by Zn/Tm mix in a ratio 0.63/0.37. At this point we cannot point out, if it exists, a clear selectivity rule for chemical species to occupy a specific position in the shells of clusters. However it is evident that mixing of the chemical species occurs as a consequence of the overlay of the atomic shells of neighboring clusters.

The partially occupied sites are the atoms 104 and 101 from the OR, that are generated by the #4 soccer-ball polyhedral shell, and 146, 147 and finally 148 from the AR. The atom 146 forms a phason flip site with the atom 55. The atom 147 is generating a close distance with the atom 145. It is therefore no surprising that low occupancy of the site 147 with probability 0.15 is obtained.

Finally, we would like to comment on the magnitude of the phason disorder. The phason correction was made by the general Debye-Waller formula with the phasonic ADP equal to 1.44 $Å^2$. That value is rather low comparing to other known iQCs [61, 62, 191], which is around 3.5 $Å^2$. By curiosity, the phasonic ADP was forcefully set to 0 $Å^2$, to check how much the value of the *R*-factor would change. To our surprise, the *R*-factor almost did not change and was equal to 9.9%. That is a very important result. The phasonic disorder is known to be correlated to single atomic jumps or the frozen lattice disorder associated with the tiling. Single atomic jumps to some extent can be modelled by introducing partial occupancies. However, nothing can be done about the lattice part. The lattice randomization by phasons is what can only be modelled by phasonic Debye-Waller factor [83, 130]. Since our result stays the same when the phasonic ADP is neglected, that means the tiling is correctly chosen. That could mean the AKNt very well describes the structure of the Bergman QC.

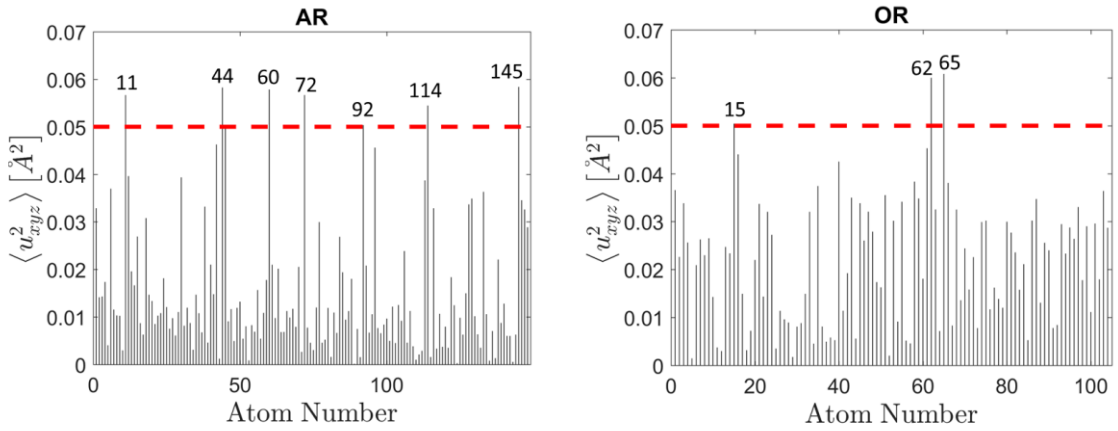

Figure 30. The mean square displacement parameters ($\langle u_{xyz}^2 \rangle$) plotted for atoms in the asymmetric part of the AR (left) and OR (right). The cut-off value of 0.05 Å^2 is shown (red-dotted line). The labels of atoms that exceed the threshold are given.

5. The local structure of the ZnMgHf F-type quasicrystal

This is an Accepted Manuscript of an article published online by Taylor & Francis in *Materials Science and Technology* in 2019, available online:

http://wwww.tandfonline.com/10.1080/02670836.2019.1612579.

The additional section about the analysis of the local structure with respect to the cluster linkages was added.

5.1 Introduction

ZnMgHf alloy [192, 193] is an ideal candidate to investigate the conditions of the QC formation. It was discovered by a chemical substitution of elements in the ZnMgSc [66] phase forming a P-type i-QC with Tsai clusters. Surprisingly, the original premise that the structure will be similar in terms of a geometry of the cluster was incorrect and the QC was formed with Bergman clusters [192]. Apart from potential scientific benefits, enriching the knowledge about phase stability mechanisms, ZnMgHf has plausible industrial applications. ZnMg alloys are extensively studied for their mechanical properties [194, 195]. Excellent strength after precipitation with ZnMgY QCs was observed [196] however due to a high cost of yttrium it did not find a market. On the other side hafnium, as a cheaper element, could be a suitable replacement. In the ZnMgHf system the existence of both P-type ($Zn_{85}Mg_7Hf_8$) and F-type QC ($Zn_{77}Mg_{17}Hf_6$) was reported along the periodic phase ($Zn_{76}Mg_{20}Hf_4$) which appeared to be a 1/1 cubic approximant to the F-type QC [193]. Previous studies were performed by means of powder X-ray diffraction (XRD), to carry out a phason strain analysis, and an electron microscopy to identify phases in a sample. For most, the composition range in 873 K for each phase was determined with EPMA concluding the composition for each element to be varying in the range of 3 at. % for Zn and Mg and 2 at. % for Hf [193]. The local cluster environment takes the form of the Bergman-type for the F-type phase and the Tsai-type for the P-type phase. The rule of e/a is preserved suggesting the Hume-Rothery mechanism of stabilization. The cluster environment was observed under an electron microscope with a HAADF-STEM technique [193]. An indication that the Bergman cluster is indeed forming the structure came with the analysis by Gomez *et al.* [181] who performed a structure refinement of the 1/1 cubic approximant of ZnMgTM, TM={Hf, Zr, Ti} QCs from a single crystal XRD. Those periodic isostructures are built of two types of Bergman clusters distinguished by the TM atom positions. Due to high disorder occurring in the sample and the complexity of the structure the agreement of the model with the experimental diffraction data is not ideal ($R = 7.35\%$ for ZnMgHf) and the composition is significantly different from the experimentally observed (up to 3 at. % for Zn atoms). Nevertheless, close enough to be convinced of the correctness of the model. The distinction between clusters is primarily made by the TM atom's preference in the occupation of the high-symmetry positions of the rhombic triacontahedral outer shell. The cluster centered at the unit cell's vertex (V-RTH) has 5-fold

vertices occupied by TM, whereas the one centered in the middle of the unit cell (B-RTH) has 3-fold vertices occupied by TM. What is also interesting, is the peculiar type of disorder observable in the electron density map. Atoms seem to fluctuate significantly along the 5-fold direction meaning that the atomic cluster is distorted. Even though the structure of the approximant crystals was solved by XRD, the same lacks for the F-type QC. The main problem was an absence of a good quality single crystals of a proper size, necessary for succeeding in the structure analysis. As it was already mentioned, all previous experiments on this QC were performed with the use of the electron microscopy on small crystals in the range of tens of nanometers. In this paper we report a successful synthesis of good quality ZnMgHf F-type QCs with a max diameter ~300 μm (see Fig. 32). After an initial screening for the best crystalline grain, the single crystal XRD was performed using a synchrotron radiation and a local cluster structure was derived using a charge flipping algorithm [107, 175]. The synthesis was checked to be repeatable, resulting with high-quality crystals at each time.

5.2 Synthesis

The QC was synthesized by a high-temperature reaction of pure elements. High purity Zn (Nilaco 4N), Mg (Nilaco 4N) and Hf (99.9%) were used. The rod of Zn ($\sim$1 cm in a diameter) was cut into discs ($\sim$1 mm thick) and subsequently each disc was additionally split in halves. The rod of Mg ($\sim$0.5 cm in a diameter) was also cut into discs ($\sim$1 mm thick) without further processing. Hf takes a form of a sponge out of which small grains were selected. Since no single grain of size suitable for a single crystal XRD was grown after the first attempt, we experimented with an initial composition and altered a heat treatment in order to obtain faceted grains, which would be a marker of a good quality sample. For the first synthesis the initial composition was adapted from Hasegawa et al. [192]: $Zn_{77}Mh_{17}Hf_6$. The elements were put into the Al_2O_3 crucible, with the toughest (Hf) to melt on the bottom and Zn on top as it has the lowest melting point among used elements. Afterwards, the components were sealed in a quartz tube under Ar atmosphere (back pressure $\sim$600 Torr) after previous evacuation to a pressure of $2.1 \cdot 10^{-6}$ Torr. The heat treatment, adapted from Ohhashi *et al*., [193], was executed in a muffle furnace. First, we performed a rapid heating up to 923 K in 6h, finally reaching 973 K after additional 1h. We avoided exceeding 973 K for the high content of Zn in the sample which boils at 1180 K and could intensely evaporate. The sample was kept in 973 K for 12 h to melt constituents. Even so the melting point of Hf is much higher (2504 K), it is dissolved by Zn-Mg melt. After cooling the sample with a ratio of -2.8 K/h we reached the annealing temperature (823 K) in which a sample was held for 7 d (144 h). The process was finalized by quenching the sample in water and breaking a quartz tube. Within two attempts no faceted QC were observed even though the F-type phase was existing with trace amounts of Zn and Zn_2Mg Lavas phase [197] (Fig. 31). To check the crystal for phase transitions we performed a DTA experiment with a heating ratio equal to 10 K/min. The phase transition starting from 843 K is seen (Fig. 32 right). We performed a third attempt to grow the F-type

QC with a plan to set the annealing temperature to 833 K. Since we also observed a strong evaporation of Zn we intended to increase its amount to 79 at. % while decreasing the Mg content to 13 at. % and increasing Hf content to 7 at. %. Using the same elements as before and the same preparations conditions we resulted with faceted QCs visible under an optical microscope (Fig. 32 left).

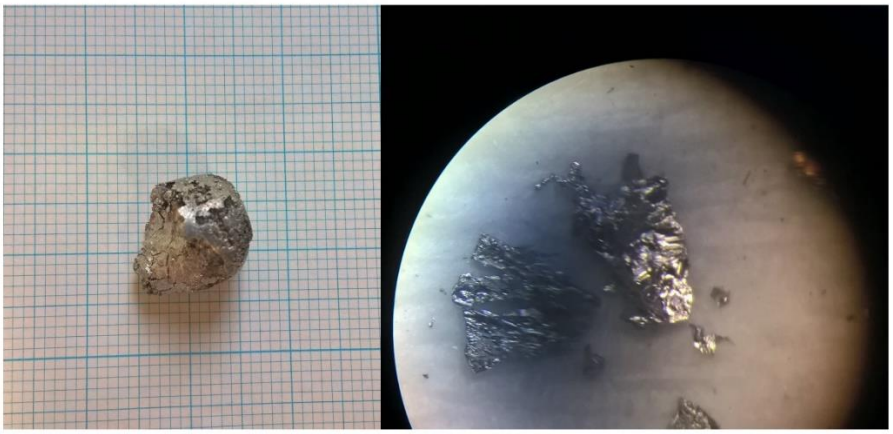

Figure 31. The shape of the sample after preparation (left) and the magnification (80x) of reflective grains found in the sample (right). The existence of the F-type ZnMgHf QC was confirmed with a powder XRD. No faceted QCs were observed.

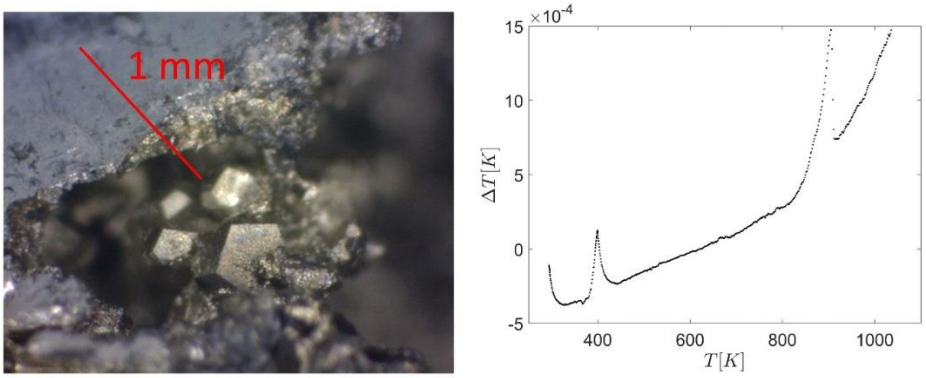

Figure 32. The DTA figure (heating phase) showing phase transition around 843 K (right). The peak, starting around 373 K shows water evaporation. The faceted QCs with pentagonal dodecahedron shape were observed under optical microscope after annealing in 833 K (left).

5.3 Characterization

To confirm the existence of an icosahedral phase in the sample with no faceted QC the powder XRD with Cu*Ka* radiation was performed with the use of in-house Rigaku RINT-2000 diffractometer.

The sample was grinded in an agate-mortar to obtain grains < 25 μm. The indexation was performed in a 6D Elser base [112] identifying the first high peak as a 422222 5-fold reflection. All peaks were identified in the vicinity of $\Delta 2\theta = 0.04°$ (Fig. 33). The systematic extinction rule characteristic for the F-type QC (all indices are even or odd) is observed. The quality of the sample was checked by the analysis of the peak broadening with respect to parallel (k_{par}) and perpendicular (k_{per}) component of the six-dimensional scattering vector. The existence of a phason strain, typical only for QC structures is reflected by the dependence of the peak position with respect to k_{per}. It is responsible for breaking the icosahedral symmetry and the reduction of the long-range order. Within our sample, the regular lattice strain with respect to k_{par} is observed, however no relation with k_{per} is present, meaning the phason strain is absent in the structure. The annealing treatment is known to reduce the phason strain in the crystal and since the sample was extensively annealed in an elevated temperature it is not visible in our sample.

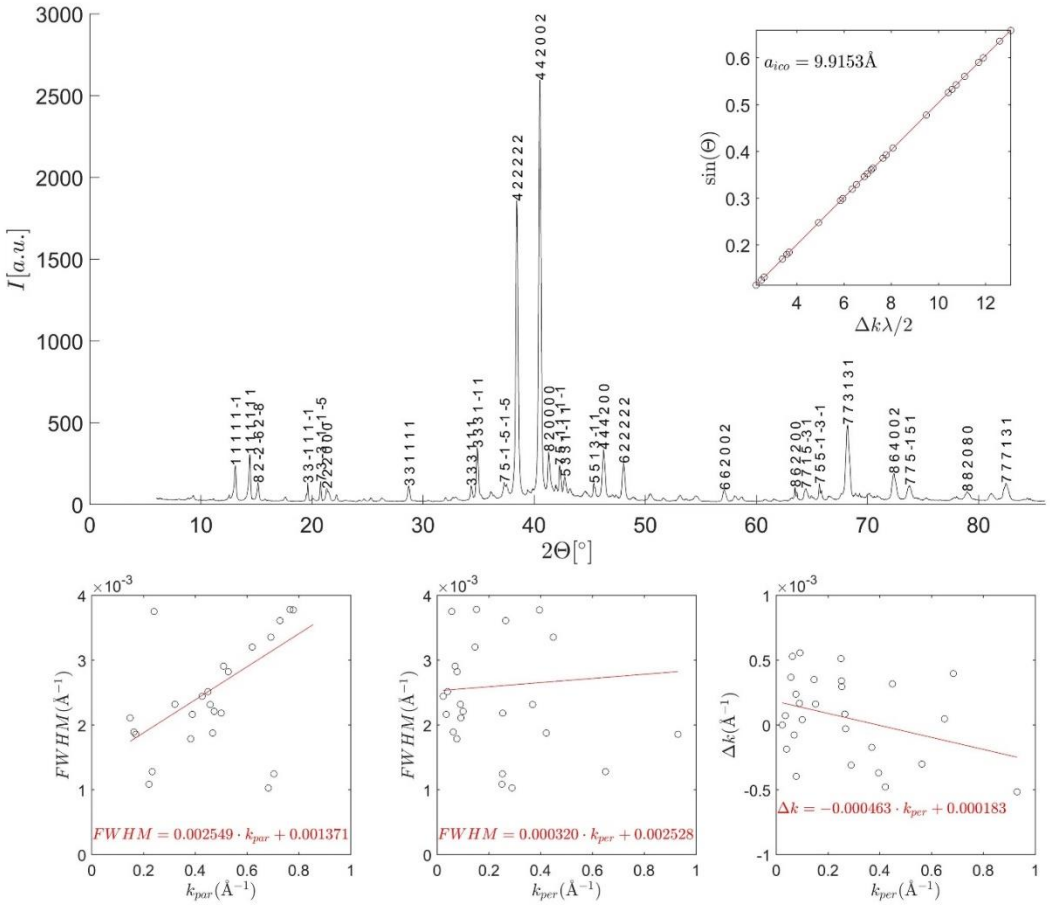

Figure 33. The diffraction pattern of the F-type icosahedral ZnMgHf QC indexed in the Elser base (top). The inset plot shows a_{ico} lattice constant fit. The width of the peak and a peak shift plotted with respect to the k_{par} and k_{per} (bottom). No phason strain is reported, only regular linear strain is observed.

The composition of the crystal after a successful growth of the faceted grains with the altered temperature program was checked with WDX on EPMA (Fig. 34)

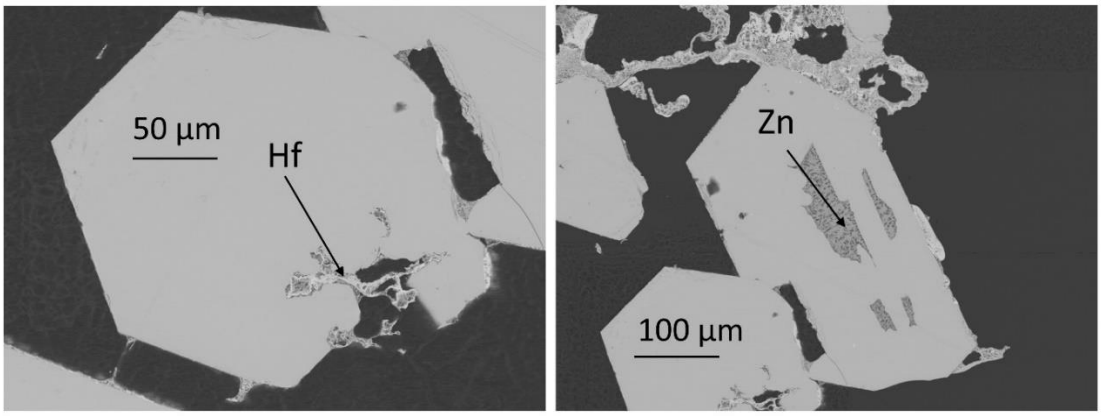

Figure 34. The BSE (Back-Scattered Electron) images of the single crystal phases of ZnMgHf. Zn and Hf islands are detected.

The average composition after the measurement of the elements' content in eight different points for each grain was concluded to be: $Zn_{80,7}Mg_{11,7}Hf_{7,5}$. The standard deviation of the atomic composition is < 0.2 at. %. It is significantly different than the composition reported during previous research [19, 20]. The surplus of Mg and the deficiency of Zn in previous studies could be the reason for lack of the observation of large single crystals. The significant mixing between Zn/Mg could lead to the presence of disorder, affecting crystalline growth.

The existence of the F-type centering in the QC was also proven with an electron diffraction. In the Fig. 35 three characteristic rotational symmetries are shown, including a 5-fold symmetry (10-fold due to Friedel's law). A characteristic $\tau = (1 + \sqrt{5})/2$ scaling is being shown in the diffraction diagram involving 2-fold symmetry. That is a clear indication of the superlattice existence.

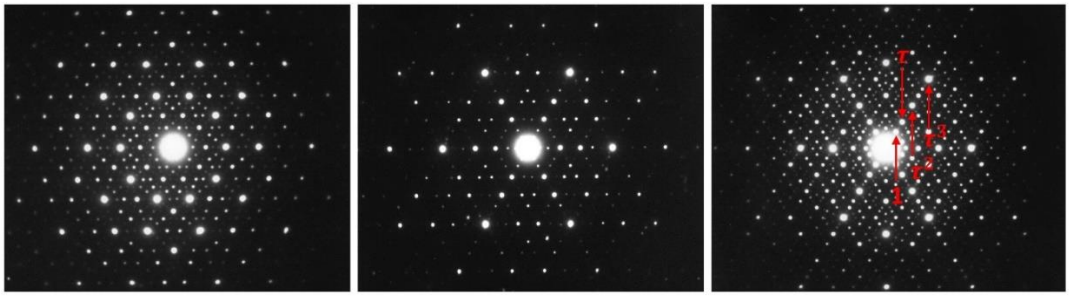

Figure 35. The electron diffraction of the ZnMgHf icosahedral QC in the plane perpendicular to the 5-fold (left), 3-fold (mid) and 2-fold (right) axis. The $\tau = (1 + \sqrt{5})/2$ scaling characteristic for the F-type QC is observed along 5-fold direction of the 2-fold symmetry diffraction pattern

5.4 The local structure

The single crystal diffraction data was collected at the Crystal beam line at synchrotron SOLEIL. The measurement was conducted at 120 K with the incident energy of 21.28 keV. Two runs with different exposure time were collected to cover the wide dynamic range of peaks' intensities. The integration of the reflection data was conducted with a *CrysAlis*^{Pro} software [174] and 4197 independent reflections were collected. The *Superflip* software [107] was used to assign phases to the diffraction peaks resulting in the crystallographic R = 22.41%. The value of the R-factor allows to discuss the main features of the structure however, fine details must be discussed only after the refinement. The electron density map, which was obtained from the phased diffraction data, shows the existence of Bergman clusters. At this point we can confirm that the F-type ordering is executed by a chemical substitution of high symmetry positions in a cluster resulting in two atomic decorations of the clusters (Fig. 36). The difference is best visible by observing the Hf's position in the rhombic triacontahedron. The first version of the cluster has large electron density accumulation in 3-fold vertices of the triacontahedron. It corresponds to B-RTH cluster from the model of 1/1 approximant by Gomez *et al*. [181]; Hf in the second cluster is located in 5-fold positions of the triacontahedron, just like in the V-RTH cluster in the latter model. Even though the similarity between the structure of the approximant crystal and the QC is significant we are unable to assign the atomic decoration to remaining positions in the cluster due to low a contrast between Zn and Mg in the electron density. Further analysis will be possible after the structure model of the F-type QC is ready for the refinement. The other characteristic trait of the structure is that it exhibits a significant disorder in the inner shells of the B-RTH cluster. What is interesting, a similar disorder manifests itself in the B-RTH cluster in Gomez *et al.*'s model [181]. The atomic position, particularly occurring in the inner shell is highly diffused outward along 5-fold direction. It is a proof of high relaxation of the atomic shells, possibly due to the existence of a free atom in the cluster center. The V-RTH cluster seems to lack the atom in the center of the cluster. The isosurface plot of the electron densities represents all the shells of the cluster confirming Bergman cluster to be formed (Fig. 37).

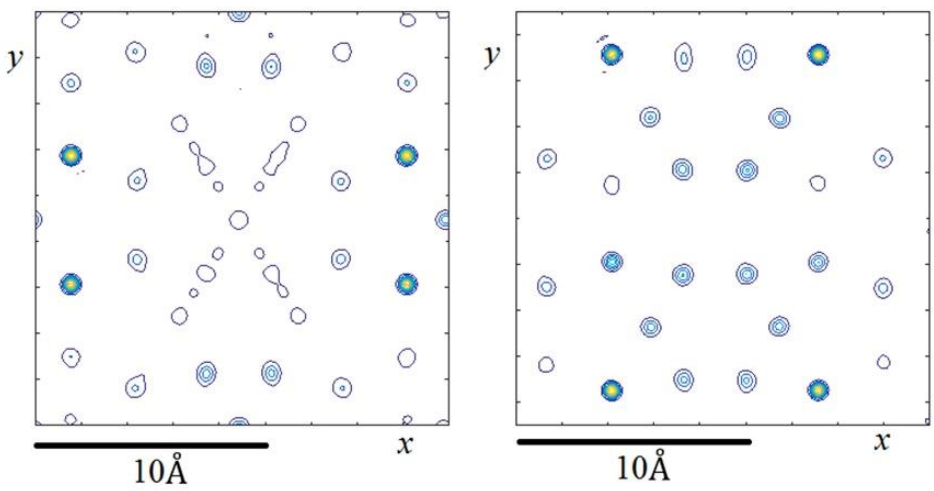

Figure 36. The section through the cluster center calculated from the phased diffraction data. Two types of Bergman clusters are visible: Hf occupies 3-fold vertices of the rhombic triacontahedron (left) and 5-fold position (right). That confirms the existence of the similar clusters in the QC as in the approximant crystal reported by Gomez et al.

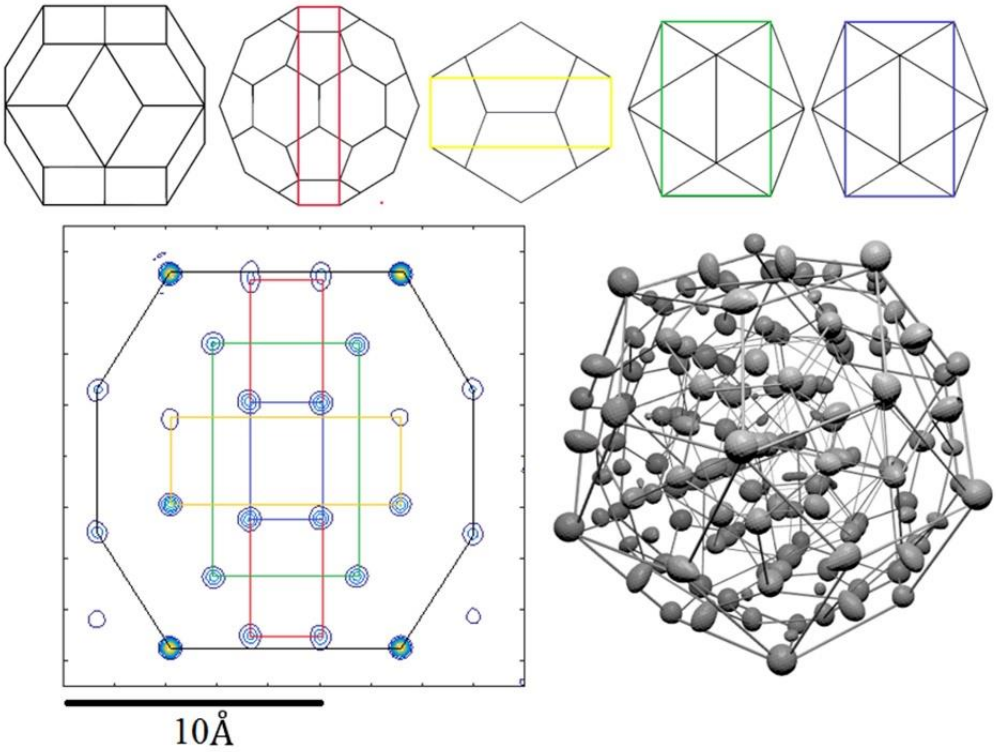

Figure 37. The Bergman cluster in the i-ZnMgHf F-type QC is composed of five shells: (from left) rhombic triacontahedron, soccer-ball polyhedral, dedecahedron, icosahedron and inner icosahedron. The

vertices contributing to high intensity positions visible in the contour plot are related to sections through each shell of the cluster. A 3D visualization of the complete cluster by a calculation of the isosurfaces in the electron density map is shown (bottom right).

Similarly to the analysis of the ZnMgTm iQC, discussed in §4.3, the sections through a 6D electron density were calculated based on the results of the phasing with a SUPERFLIP software. The electron density maps are plotted in Fig. 38. Just by comparing the axis units in Fig. 18 and Fig. 38 it is evident that a 6D unit cell, that in both figures is outlined with a red rectangle, for the ZnMgHf F-type QC is doubled. It is another indication about the formation of the superlattice in the case of the FCI QC. The even vertex OD, labeled as n_0 in Fig. 38 exhibit an empty center, similarly to the corresponding OD in Fig. 18. As it was pointed out, the V-RTH cluster has an empty cluster center, therefore it is not surprising that the nD embedding of those sites is unoccupied. Apart from n_0 domain, there is also a n_1 domain, occupying odd nodes of the 6D lattice and a bc_0 that is a body-center OD within a unexpanded unit cell. All three ODs are visible in the 5-fold section (a)) and the 3-fold section (b)) but a 2-fold section shows no signs of the superlattice and only an n_0 domain is present. Since the high electron density is accumulated in the n_1 domain, that means Hf is occupying vertices corresponding to those sites.

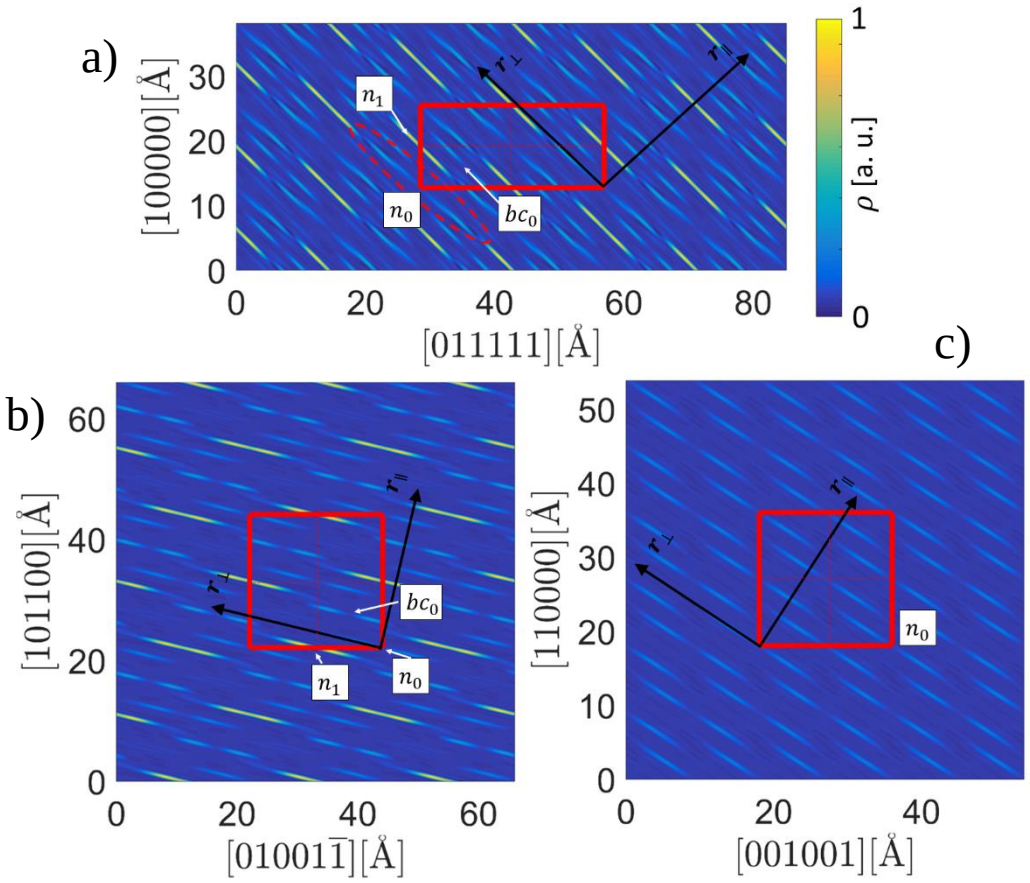

Figure 38. The 2D sections through the 6D electron density of the ZnMgHf F-type Bergman quasicrystal. Sections containing 5-fold axes (a)), 3-fold axes (b)) and 2-fold axes (c)) are presented. In each figure the outline of the 6D unit cell is plotted (red rectangle) together with vectors representing parallel ($r_\parallel$) and perpendicular ($r_\perp$) space.

The reason why within the 2-fold section the unit cell is not doubled is very clearly visible when the 2D section through the 3D real space is calculated. In Fig. 39 a block $100\text{Å} \times 100\text{Å}$ is plotted perpendicularly to the 2-fold axis. With a green and red line an outline of the RTH cluster is plotted. The green corresponds to the cluster with Hf atoms occupying the 3-fold vertices of the triacontahedral shell (B-RTH) and the red corresponds to the cluster with Hf atoms in the 5-fold vertices of the triacontahedral shell (V-RTH). Selected clusters within the section were outlined to vizualize all the interesting features. What can be perceived straight away is the clusters are connected via tha *a*-linkage, therefore the cluster covering developed for the ZnMgTm strucuture is valid. What goes beyond a simple PI quasicrystal is the *a*-linkage occurs between V-RTH and B-RTH. Two clusters of the same type are never connected along the *a*-linkage (patch 2.). The same applies for the *c*-linkage (patch 3.) The supercell evident in the 5- and 3-fold section through the 6D electron density in Fig. 38 is therefore caused by two types of cluster that alternately appear in the structure. If there was no other cluster, the

strucutre would be a PI. Let's now focus on the linkages along 2-fold axes. A short *b*-linkage is also present in the strucutre of the F-type QC (patch 1.) but contrary to what was true for the *a*- and *c*- linkage, the *b*-linkage is always connecting two clusters of the same type. That is true both for the V-RTH and B-RTH cluster. That is the reason why in the 2-fold section through the 6D electron density the unit cell is not doubled.

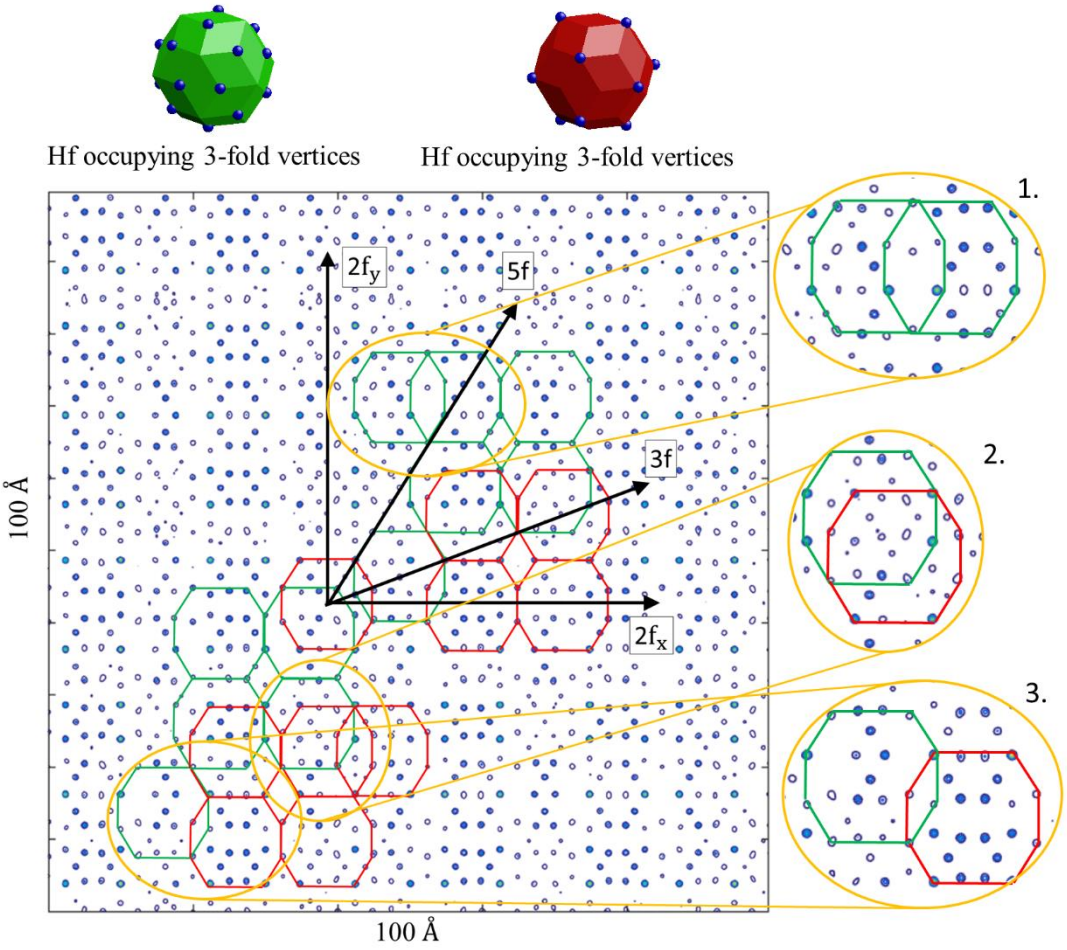

Figure 39. The $100\text{Å} \times 100\text{Å}$ 2D section through the 3D electron density in the real space, perpendicular to the 2-fold axis. V-RTH cluster (red) and B-RTH cluster are outlined to indicate characteristic linkages. Patch 1. Shows a *b*-linkage, patch 2. Represents an *a*-linkage and patch 3. Marks a *c*-linkage. Only a *b*-linkage (both short and regular) can connect two clusters of the same type.

6. Summary

6.1 ZnMgTm P-type iQC

The structure model for the PI ZnMgTm QC is proposed based on the atomic decoration of the two rhombohedra in Ammann-Kramer-Neri tiling. The rhombohedra used in the model are τ^3 inflated in comparison to standard lattice size. The inflation allows to evade the problem of an ambiguous decoration of rhombohedra in the interstitial part of the structure existing in a cluster-based model. The ambiguity was the main obstacle for the construction of the occupation domains for the structure modelling in a 6D embedding. For the structure refinement, we resigned from the higher-dimensional approach for the sake of the real-space approach. Since the structure modelling was based on the real-space atomic decoration of rhombohedra it is redundant to lift the structure to 6D just for the refinement.

The iQC was classified as the Bergman QC based on the inner structure of the rhombic triacontahedral cluster. The 3D electron density map, reconstructed after phasing with *Superflip*, shows four possible linkages between rhombic triacontahedral clusters. Apart from known *b*- and *c*-linkages there are short *b*- and *a*-linkages. The interaction of atoms due to the existence of additional linkages creates split atomic positions in the high-symmetry sites of the structure and a few instances of large ADPs. All the characteristic features observed in the *ab initio* structure solution are well represented in the refined structure.

The refinement resulted in a very good agreement of the calculated structure factor with the experimental diffraction amplitudes measured by the crystallographic *R*-factor equal to 9.8% with the reflections-to-parameters ratio of about 3.9. The model shows an inherent chemical mixing of atoms which is commonly observed for ZnMg-Rare-Earth QCs and approximants.

The analysis of the refined structure in terms of the Bergman cluster distribution shows two major novelties:

1. A whole structure can be represented as a covering by rhombic triacontahedral clusters. All the atoms are generated by the vertices of five shells of the Bergman cluster expanded with the most outer shell of rhombic triacontahedron. No interstitial part of the structure must be distinguished contrary to what was proposed for binary CdYb QC.
2. Apart from the *b*- and the *c*-linkages given by the 12-fold sphere packing geometry, the short *b*- and *a*-linkages are present in the model. The linkage along a 5-fold direction is primarily responsible for the occurrence of the occupied cluster centers observed in the electron density map. The node of the #2 icosahedral shell interpenetrates the central position of the neighboring cluster being perceived as a lonely atom inside the cluster. The *a*-linkage does not introduce short interatomic distances as the sites that are in close

vicinity to each other become split atomic sites. In reality, those sites are giving space for the occurrence of the phason flips.

The main question is whether a proposed model, with the cluster covering, could be used to two other families of iQC: Tsai and Mackay. Before the attempt of the structure modelling is made we cannot answer this question. To our knowledge it can be that only Bergman QC demonstrates such a peculiar atomic structure.

When it comes to the rare-earth atom distribution it is difficult to unambiguously tell which cluster sites are occupied by this element. In principle the Tm element is located at the vertices of triacontahedron but due to the short *a*-linkage and the *c*-linkage the inner dodecahedral shell can also be occupied by Tm atoms. To our knowledge the occupation of the triacontahedron by Tm depends on the local arrangement of the RTH clusters but the number of such local environments is much greater than those of the standard cluster-based model with *b*- and *c*-linkages only. It is therefore much more convenient to use the golden rhombohedra than cluster to tell where the atoms in the structure really are.

6.2 ZnMgHf F-type iQC

The high-quality, faceted single crystals of the ZnMgHf F-type QC were synthesized with the use of the self-flux crystal growth technique, reaching a diameter of up to ~ 300 μm. The synthesis process known from literature was refined based on the known results published before in the literature and in-house DTA measurements. The quality of grown crystals was satisfactory to conduct an X-ray diffraction experiment using a synchrotron facility, which resulted in a dataset of more than 4000 symmetry independent diffraction peaks that were used further for the local structure designation.

The local structure of the F-type Bergman QC was solved and analyzed based on the result of the *ab initio* structure solution made by the charge flipping algorithm implemented in the SUPERFLIP software. The self-consistent algorithm allows assigning phases to diffraction Bragg peaks and therefore retrieve the electron density which corresponds to the distribution of atoms in the structure. The convergent of the structure model with experimental data was finalized with the crystallographic R-factor equal to 22.4%. Even though it is higher than results obtainable e.g. P-type structures it allows to retrieve the structure features even without the atomic structure refinement.

The structure was proven to be a Bergman type iQC based on the shape of the local atomic cluster. Two types of clusters were found: The RTH cluster with Hf distributed in the 3-fold vertices of the triacontahedral shell and the RTH cluster with Hf distributed in the 5-fold vertices of the triacontahedral shell. It well corresponds to the result of the atomic structure refinement performed upon 1/1 cubic periodic approximant crystals of the ZnMg(Hf, Ti, Zr) known in the literature. For the approximant crystals, two clusters were also distinguished: V-RTH cluster located in the vertices of the unit cell and B-RTH cluster located in the center of the unit cell. The V-RTH cluster corresponds to the cluster with Hf located in 5-fold vertices of the triacontahedral shell and B-RTH to the other one. In

addition, both in the approximant crystals and now in the QC, the B-RTH cluster is distorted along 5-axes pointing from the center of clusters due to the center of a cluster being occupied by atomic species. V-RTH clusters seem to be empty in the center, which is also evident in the 2D sections through the 6D electron density.

The large $100\text{Å} \times 100\text{Å}$ block of the real space electron density was calculated, perpendicular to the 2-fold direction. By analyzing the cluster distribution within a calculated section, the existence of *a*-linkages and short *b*-linkages was confirmed alongside regular *b*- and *c*-linkages known from the structure model of the Tsai iQC. What is specific for the F-type structure is the *a*-linkage and the *c*-linkage connect clusters of different types i.e. V-RTH cluster is linked with B-RTH cluster and never two clusters of the same type are linked with those linkages. It is constrain imposed by the F-type superlattice formation (or rather a superlattice is formed due to a specific linkage rule between clusters). It is confirmed by the nD sections were 3- and 5-fold sections exhibit a superlattice, whereas a 2-fold section does not show the unit cell to be doubled. In the real space, two clusters of the same type can be connected only along a *b*-linkage.

Currently, an infinite structure model of the F-type Bergman QC has not been developed.

Supporting information

In Table S1 the list of the refined parameters of the ZnMgTm structure is submitted [143]. Coordinates x, y and z are given in a rhombohedron-spanning base, what means real-structure **r** coordinate vector is obtained as follows: $r = X\mathbf{f}_1 + Y\mathbf{f}_2 + Z\mathbf{f}_3$, where $\mathbf{f}_1, \mathbf{f}_2, \mathbf{f}_3$ are vectors spanning edges of the rhombohedra. For the AR those vectors are $\mathbf{a}_1$, $\mathbf{a}_2$, $\mathbf{a}_6$ respectively and for the OR $\mathbf{a}_1$, $-\mathbf{a}_3$, $-\mathbf{a}_6$. The letter 'L' stands for an acute rhomb and the letter 'S' stands for a obtuse rhombus. SOF defines site of fraction: 1 means the position is fully occupied, 0 means there is no atom there. The column labeled „Fraction" gives the ratio of atom inside a rhombus depending on it position in a rhombus f. i. atom on the edge is only in half inside a rhombus. Variable $\langle {u^2}_{xyz} \rangle$ defines mean atomic displacement.

Table S1 The list of parameters describing the structure model of ZnMgTm iQC.

Unit Type	Nr	x	y	z	p(Zn)	p(Mg)	p(Tm)	SOF	$\langle {u^2}_{xyz} \rangle$ [Å²]	Fraction
L	1	1.0000	1.0000	1.0000	0.0000	0.0000	1.0000	1.0000	0.032873	0.0083
L	2	0.8511	0.8511	0.8511	1.0000	0.0000	0.0000	1.0000	0.014136	0.166667
L	3	1.0000	0.8490	0.8489	1.0000	0.0000	0.0000	1.0000	0.014304	0.5
L	4	0.7654	0.7655	0.7654	0.0000	0.0000	1.0000	1.0000	0.017362	0.166667
L	5	1.0000	0.7656	0.7656	0.6017	0.0000	0.3983	1.0000	0.004038	0.25
L	6	0.7065	0.7087	0.7066	1.0000	0.0000	0.0000	1.0000	0.03697	0.166667
L	7	0.7361	0.6186	0.6186	1.0000	0.0000	0.0000	1.0000	0.011544	0.5
L	8	0.8503	0.6170	0.6170	1.0000	0.0000	0.0000	1.0000	0.010316	0.5
L	9	1.0000	0.6357	0.6096	0.0000	0.0000	1.0000	1.0000	0.010224	0.25
L	10	0.7298	0.5490	0.5490	1.0000	0.0000	0.0000	1.0000	0.002974	0.5
L	11	1.0000	0.5634	0.5428	1.0000	0.0000	0.0000	1.0000	0.05667	0.5
L	12	0.5258	0.5258	0.5250	1.0000	0.0000	0.0000	1.0000	0.039609	0.166667
L	13	0.6961	0.4836	0.4836	1.0000	0.0000	0.0000	1.0000	0.019586	0.5
L	14	0.8493	0.4787	0.4787	1.0000	0.0000	0.0000	1.0000	0.016645	0.5
L	15	1.0000	0.4931	0.4333	1.0000	0.0000	0.0000	1.0000	0.026908	0.5

L	16	0.4688	0.4688	0.4688	0.0000	0.0000	1.0000	1.0000	0.0087	0.166667
L	17	1.0000	0.3843	0.3843	0.0000	0.0000	1.0000	1.0000	0.006281	0.25
L	18	0.3768	0.3635	0.3462	1.0000	0.0000	0.0000	1.0000	0.030785	0.166667
L	19	0.4971	0.3820	0.3819	1.0000	0.0000	0.0000	1.0000	0.014663	0.5
L	20	0.6149	0.3837	0.3797	1.0000	0.0000	0.0000	1.0000	0.013353	0.5
L	21	0.7679	0.3818	0.3740	0.0000	0.0000	1.0000	1.0000	0.008512	0.5
L	22	0.4948	0.3128	0.3128	1.0000	0.0000	0.0000	1.0000	0.010262	0.5
L	23	0.7308	0.3091	0.3088	1.0000	0.0000	0.0000	1.0000	0.010794	0.5
L	24	0.2346	0.2355	0.2350	0.0000	0.0000	1.0000	1.0000	0.018126	0.166667
L	25	0.4707	0.2407	0.2407	0.6863	0.0000	0.3137	1.0000	0.012074	0.5
L	26	0.6102	0.2398	0.2398	1.0000	0.0000	0.0000	1.0000	0.007521	0.5
L	27	0.7327	0.2384	0.2384	1.0000	0.0000	0.0000	1.0000	0.009739	0.5
L	28	0.8576	0.2329	0.2329	1.0000	0.0000	0.0000	1.0000	0.006094	0.5
L	29	1.0000	0.2405	0.2405	1.0000	0.0000	0.0000	1.0000	0.011048	0.25
L	30	0.1530	0.1533	0.1529	1.0000	0.0000	0.0000	1.0000	0.039365	0.166667
L	31	0.7597	0.1483	0.1483	0.3929	0.0000	0.6071	1.0000	0.008154	0.5
L	32	0.2680	0.1461	0.1402	1.0000	0.0000	0.0000	1.0000	0.011936	0.5
L	33	0.3845	0.1610	0.1295	1.0000	0.0000	0.0000	1.0000	0.00872	0.5
L	34	0.5213	0.1452	0.1452	1.0000	0.0000	0.0000	1.0000	0.003104	0.5
L	35	0.7120	0.0863	0.0863	1.0000	0.0000	0.0000	1.0000	0.014675	0.5
L	36	0.2637	0.0727	0.0727	1.0000	0.0000	0.0000	1.0000	0.010787	0.5
L	37	0.4981	0.0730	0.0730	1.0000	0.0000	0.0000	1.0000	0.006758	0.5
L	38	0.0000	0.0000	0.0000	0.0000	0.0000	1.0000	1.0000	0.0332	0.0083
L	39	0.2340	0.0000	0.0000	0.5331	0.0000	0.4669	1.0000	0.004593	0.1
L	40	0.3869	0.0000	0.0000	1.0000	0.0000	0.0000	1.0000	0.021	0.1
L	41	0.5042	0.0000	0.0000	1.0000	0.0000	0.0000	1.0000	0.014783	0.1
L	42	0.6021	0.0000	0.0000	1.0000	0.0000	0.0000	1.0000	0.046273	0.1
L	43	0.8357	0.0000	0.0000	0.4471	0.4293	0.1236	1.0000	0.00122	0.1
L	44	1.0000	0.0000	0.0000	0.0000	0.0000	1.0000	1.0000	0.05824	0.075

L	45	1.0000	0.1500	0.1969	1.0000	0.0000	0.0000	1.0000	0.049964	0.5
L	46	0.9278	0.7039	0.7271	0.5000	0.5000	0.0000	1.0000	0.009076	1
L	47	0.9175	0.3365	0.3368	1.0000	0.0000	0.0000	1.0000	0.011649	0.5
L	48	0.8529	0.6191	0.7349	1.0000	0.0000	0.0000	1.0000	0.004927	1
L	49	0.6176	0.5061	0.6176	0.6313	0.0000	0.3687	1.0000	0.011912	0.5
L	50	0.6213	0.3836	0.4987	1.0000	0.0000	0.0000	1.0000	0.013214	1
L	51	0.8419	0.3622	0.4812	1.0000	0.0000	0.0000	1.0000	0.005434	1
L	52	0.3827	0.2660	0.3827	1.0000	0.0000	0.0000	1.0000	0.008038	0.5
L	53	0.3835	0.1527	0.2648	1.0000	0.0000	0.0000	1.0000	0.000855	1
L	54	0.6180	0.1175	0.2307	0.8343	0.0000	0.1657	1.0000	0.008275	1
L	55	0.8091	0.0000	0.1207	0.3806	0.3419	0.2775	1.0000	0.006894	0.5
L	56	0.6190	0.0000	0.1159	1.0000	0.0000	0.0000	1.0000	0.015657	0.5
L	57	0.8489	0.7359	0.8608	1.0000	0.0000	0.0000	1.0000	0.005441	0.5
L	58	0.8595	0.2310	0.3554	1.0000	0.0000	0.0000	1.0000	0.010848	1
L	59	0.8506	0.1067	0.2459	1.0000	0.0000	0.0000	1.0000	0.017778	1
L	60	0.8065	0.4662	0.6012	1.0000	0.0000	0.0000	1.0000	0.05784	1
L	61	0.6102	0.2402	0.3825	1.0000	0.0000	0.0000	1.0000	0.020974	1
L	62	0.3871	0.0000	0.1519	1.0000	0.0000	0.0000	1.0000	0.009769	0.5
L	63	0.6877	0.5045	0.6884	1.0000	0.0000	0.0000	1.0000	0.020141	0.5
L	64	0.6898	0.1166	0.3094	1.0000	0.0000	0.0000	1.0000	0.006825	1
L	65	0.9278	0.1162	0.3103	1.0000	0.0000	0.0000	1.0000	0.006839	1
L	66	0.1566	0.0000	0.1566	1.0000	0.0000	0.0000	1.0000	0.011243	0.5
L	67	0.9267	0.7346	0.9267	1.0000	0.0000	0.0000	1.0000	0.009881	0.5
L	68	0.9263	0.4992	0.6917	1.0000	0.0000	0.0000	1.0000	0.011715	1
L	69	0.9263	0.3549	0.5472	1.0000	0.0000	0.0000	1.0000	0.007913	1
L	70	0.5194	0.3238	0.5173	0.0000	1.0000	0.0000	1.0000	0.020522	1
L	71	0.6936	0.2659	0.4553	0.5000	0.5000	0.0000	1.0000	0.002657	1
L	72	0.5486	0.1395	0.3272	1.0000	0.0000	0.0000	1.0000	0.056672	1
L	73	1.0000	0.7663	1.0000	0.5303	0.0000	0.4697	1.0000	0.007744	0.1

L	74	1.0000	0.6118	0.8693	1.0000	0.0000	0.0000	1.0000	0.004573	0.5
L	75	0.7614	0.5257	0.7614	1.0000	0.0000	0.0000	1.0000	0.003028	0.5
L	76	0.6188	0.3861	0.6190	1.0000	0.0000	0.0000	1.0000	0.011987	0.5
L	77	0.7580	0.3842	0.6365	1.0000	0.0000	0.0000	1.0000	0.029957	1
L	78	1.0000	0.3720	0.6280	0.0000	0.0000	1.0000	1.0000	0.004578	0.5
L	79	0.7332	0.3174	0.5452	1.0000	0.0000	0.0000	1.0000	0.005226	1
L	80	0.3823	0.1548	0.3823	1.0000	0.0000	0.0000	1.0000	0.011897	0.5
L	81	0.7664	0.1424	0.3857	1.0000	0.0000	0.0000	1.0000	0.00159	1
L	82	1.0000	0.1501	0.3850	1.0000	0.0000	0.0000	1.0000	0.010919	0.5
L	83	0.4979	0.0801	0.3057	1.0000	0.0000	0.0000	1.0000	0.00665	1
L	84	0.2379	0.0000	0.2379	0.5935	0.0000	0.4065	1.0000	0.026855	0.25
L	85	0.3852	0.0000	0.2343	1.0000	0.0000	0.0000	1.0000	0.019391	0.5
L	86	0.4799	0.0000	0.2272	1.0000	0.0000	0.0000	1.0000	0.009426	0.5
L	87	0.6130	0.0000	0.2319	1.0000	0.0000	0.0000	1.0000	0.011236	0.5
L	88	0.7333	0.0000	0.2292	1.0000	0.0000	0.0000	1.0000	0.01801	0.5
L	89	0.8681	0.0000	0.2130	0.4932	0.4754	0.0313	1.0000	0.000147	0.5
L	90	1.0000	0.0000	0.2331	0.6111	0.0000	0.3889	1.0000	0.007479	0.3
L	91	0.8504	0.6168	0.8613	1.0000	0.0000	0.0000	1.0000	0.001548	0.5
L	92	0.4378	0.2199	0.4760	1.0000	0.0000	0.0000	1.0000	0.050347	0.5
L	93	0.8829	0.2637	0.4499	1.0000	0.0000	0.0000	1.0000	0.0208	1
L	94	1.0000	0.2379	0.4755	0.0000	1.0000	0.0000	1.0000	0.006703	0.5
L	95	0.2402	0.0635	0.3394	0.5000	0.5000	0.0000	1.0000	0.01057	1
L	96	1.0000	0.4989	0.7637	0.5000	0.5000	0.0000	1.0000	0.045612	0.5
L	97	0.7582	0.3917	0.7582	1.0000	0.0000	0.0000	1.0000	0.007662	0.5
L	98	0.8837	0.3770	0.7713	1.0000	0.0000	0.0000	1.0000	0.006571	1
L	99	0.8798	0.3118	0.6887	1.0000	0.0000	0.0000	1.0000	0.008387	1
L	100	0.6201	0.2343	0.6200	0.0000	0.0000	1.0000	1.0000	0.009647	0.5
L	101	0.5213	0.1410	0.5248	0.0000	1.0000	0.0000	1.0000	0.004961	0.5
L	102	0.6415	0.0773	0.4511	0.4323	0.3932	0.1744	1.0000	0.012161	1

L	103	0.6180	0.0000	0.3783	0.0000	0.0000	1.0000	1.0000	0.004508	0.5
L	104	0.7760	0.0000	0.3624	1.0000	0.0000	0.0000	1.0000	0.01251	0.5
L	105	0.8824	0.0000	0.3849	1.0000	0.0000	0.0000	1.0000	0.009183	0.5
L	106	1.0000	0.6137	1.0000	1.0000	0.0000	0.0000	1.0000	0.023861	0.1
L	107	0.8552	0.4776	0.8552	0.0000	0.0000	1.0000	1.0000	0.004587	0.5
L	108	1.0000	0.3937	0.7638	1.0000	0.0000	0.0000	1.0000	0.011252	0.5
L	109	0.8548	0.2335	0.6148	0.0000	0.0000	1.0000	1.0000	0.003821	1
L	110	1.0000	0.2356	0.6195	1.0000	0.0000	0.0000	1.0000	0.001	0.5
L	111	0.6440	0.1494	0.5266	0.0000	1.0000	0.0000	1.0000	0.002106	1
L	112	0.7626	0.1419	0.5290	0.0000	1.0000	0.0000	1.0000	0.00288	1
L	113	0.4870	0.0826	0.4865	0.5000	0.5000	0.0000	1.0000	0.03872	0.5
L	114	0.8291	0.0662	0.4610	1.0000	0.0000	0.0000	1.0000	0.054452	1
L	115	1.0000	0.0000	0.3843	1.0000	0.0000	0.0000	1.0000	0.00157	0.3
L	116	0.3814	0.0000	0.3816	0.0000	0.0000	1.0000	1.0000	0.03286	0.25
L	117	0.9273	0.5012	0.9273	1.0000	0.0000	0.0000	1.0000	0.003327	0.5
L	118	0.6914	0.2703	0.6914	1.0000	0.0000	0.0000	1.0000	0.010665	0.5
L	119	0.9251	0.1179	0.5449	1.0000	0.0000	0.0000	1.0000	0.003723	1
L	120	0.7611	0.2698	0.7611	1.0000	0.0000	0.0000	1.0000	0.007963	0.5
L	121	0.7694	0.1534	0.6376	0.4633	0.4592	0.0775	1.0000	0.003509	1
L	122	1.0000	0.4964	1.0000	1.0000	0.0000	0.0000	1.0000	0.018359	0.1
L	123	1.0000	0.3851	0.8850	1.0000	0.0000	0.0000	1.0000	0.012448	0.5
L	124	1.0000	0.1173	0.6082	1.0000	0.0000	0.0000	1.0000	0.00027	0.5
L	125	0.7631	0.0000	0.5239	0.0000	1.0000	0.0000	1.0000	0.00982	0.5
L	126	1.0000	0.0000	0.5013	1.0000	0.0000	0.0000	1.0000	0.006276	0.3
L	127	0.4638	0.0000	0.4638	1.0000	0.0000	0.0000	1.0000	0.014981	0.5
L	128	0.5235	0.0000	0.5494	1.0000	0.0000	0.0000	1.0000	0.033669	0.5
L	129	0.9047	0.3390	0.9444	0.0000	1.0000	0.0000	1.0000	0.034888	0.5
L	130	0.8535	0.2349	0.8535	0.0000	0.0000	1.0000	1.0000	0.010161	0.5
L	131	0.8890	0.1483	0.7578	0.4879	0.4954	0.0168	1.0000	0.006345	1

L	132	0.8488	0.0000	0.6177	1.0000	0.0000	0.0000	1.0000	0.003507	0.5
L	133	1.0000	0.3796	1.0000	1.0000	0.0000	0.0000	1.0000	0.03631	0.1
L	134	0.7678	0.1433	0.7678	1.0000	0.0000	0.0000	1.0000	0.01058	1
L	135	0.6830	0.0712	0.6830	0.0000	1.0000	0.0000	1.0000	0.00080	0.5
L	136	0.8825	0.0706	0.6889	1.0000	0.0000	0.0000	1.0000	0.00703	1
L	137	0.6186	0.0000	0.6186	0.0000	0.0000	1.0000	1.0000	0.001323	0.25
L	138	1.0000	0.0000	0.6109	1.0000	0.0000	0.0000	1.0000	0.022068	0.3
L	139	1.0000	0.1558	0.8848	0.0000	1.0000	0.0000	1.0000	0.00874	0.5
L	140	1.0000	0.2343	1.0000	0.5000	0.5000	0.0000	1.0000	0.012799	0.1
L	141	0.7600	0.0000	0.7600	1.0000	0.0000	0.0000	1.0000	0.006012	0.25
L	142	1.0000	0.0000	0.7366	0.5000	0.5000	0.0000	1.0000	0.005993	0.3
L	143	0.9229	0.0804	0.8775	0.0000	1.0000	0.0000	1.0000	0.000544	1
L	144	0.8609	0.0000	0.8609	1.0000	0.0000	0.0000	1.0000	0.006281	0.25
L	145	1.0000	0.0000	1.0000	0.0000	0.0000	1.0000	1.0000	0.058382	0.075
L	146	0.8982	0.0000	0.1374	0.0000	1.0000	0.0000	0.7306	0.034549	0.5
L	147	1.0000	0.1055	0.1055	0.0000	1.0000	0.0000	0.1519	0.0326	0.5
L	148	1.0000	0.6233	0.7554	0.0000	1.0000	0.0000	0.3005	0.02886	0.5
S	1	1.0000	1.0000	1.0000	0.0000	0.0000	1.0000	1.0000	0.036567	0.0583
S	2	0.0000	0.0000	0.0000	0.0000	0.0000	1.0000	1.0000	0.022625	0.0583
S	3	0.6166	0.6166	0.6166	1.0000	0.0000	0.0000	1.0000	0.03383	0.166667
S	4	0.3741	0.3741	0.3741	0.4650	0.4504	0.0846	1.0000	0.025619	0.166667
S	5	0.8141	0.7208	0.8143	0.4756	0.4632	0.0611	1.0000	0.001454	0.5
S	6	0.2647	0.1913	0.1905	0.0000	1.0000	0.0000	1.0000	0.020908	0.5
S	7	0.6205	0.5014	0.6205	1.0000	0.0000	0.0000	1.0000	0.026266	0.5
S	8	1.0000	0.8831	0.8513	0.0000	1.0000	0.0000	0.5000	0.022971	0.5
S	9	0.1189	0.0000	0.1531	0.4912	0.4873	0.0215	1.0000	0.026512	0.25
S	10	0.4987	0.3894	0.3894	1.0000	0.0000	0.0000	1.0000	0.014267	0.5
S	11	0.3844	0.2370	0.3844	0.5798	0.0000	0.4202	1.0000	0.003734	0.5
S	12	0.7680	0.6190	0.6190	0.5964	0.0000	0.4036	1.0000	0.002986	0.5

S	13	1.0000	0.8540	0.8862	0.0000	1.0000	0.0000	0.5000	0.024701	0.5
S	14	1.0000	0.7662	1.0000	0.5000	0.5000	0.0000	1.0000	0.023374	0.2
S	15	0.8568	0.6572	0.7453	1.0000	0.0000	0.0000	1.0000	0.050424	1
S	16	0.2172	0.0000	0.2172	1.0000	0.0000	0.0000	1.0000	0.04403	0.25
S	17	0.2643	0.0000	0.0000	0.5234	0.0000	0.4766	1.0000	0.014926	0.2
S	18	0.6231	0.3866	0.6231	1.0000	0.0000	0.0000	1.0000	0.003165	0.5
S	19	0.6182	0.3811	0.5003	0.7047	0.0000	0.2953	1.0000	0.007213	1
S	20	1.0000	0.7605	0.7365	0.5000	0.5000	0.0000	0.5000	0.021984	0.5
S	21	0.2435	0.0000	0.1523	0.0000	1.0000	0.0000	1.0000	0.033685	0.5
S	22	0.4169	0.1881	0.2557	1.0000	0.0000	0.0000	1.0000	0.014343	1
S	23	0.5861	0.3690	0.3760	1.0000	0.0000	0.0000	1.0000	0.032031	0.5
S	24	1.0000	0.7306	0.7680	0.0000	1.0000	0.0000	0.5000	0.027225	1
S	25	0.8124	0.5037	0.8124	1.0000	0.0000	0.0000	1.0000	0.00349	0.5
S	26	0.5026	0.1938	0.4286	1.0000	0.0000	0.0000	1.0000	0.011372	1
S	27	0.8013	0.4898	0.5655	1.0000	0.0000	0.0000	1.0000	0.00959	1
S	28	0.5014	0.1870	0.1870	0.7210	0.0000	0.2790	1.0000	0.008939	0.5
S	29	0.6145	0.2630	0.6152	1.0000	0.0000	0.0000	1.0000	0.001743	0.5
S	30	0.7306	0.3740	0.3740	1.0000	0.0000	0.0000	1.0000	0.008081	0.5
S	31	1.0000	0.6183	0.7658	1.0000	0.0000	0.0000	1.0000	0.008822	0.5
S	32	0.3860	0.0000	0.2374	1.0000	0.0000	0.0000	1.0000	0.014928	0.5
S	33	1.0000	0.6053	1.0000	1.0000	0.0000	0.0000	1.0000	0.032032	0.2
S	34	1.0000	0.6252	0.8816	1.0000	0.0000	0.0000	1.0000	0.004522	0.5
S	35	0.3868	0.0000	0.3842	0.0000	0.0000	1.0000	1.0000	0.037418	0.25
S	36	0.7760	0.3842	0.6240	1.0000	0.0000	0.0000	1.0000	0.008097	1
S	37	0.6158	0.2291	0.3754	0.7298	0.0000	0.2702	1.0000	0.00494	1
S	38	1.0000	0.6149	0.6149	0.0000	0.0000	1.0000	1.0000	0.005805	0.25
S	39	0.3816	0.0000	0.1173	1.0000	0.0000	0.0000	1.0000	0.005259	0.5
S	40	0.3985	0.0000	0.0000	1.0000	0.0000	0.0000	1.0000	0.042503	0.2
S	41	0.5722	0.1166	0.4272	1.0000	0.0000	0.0000	1.0000	0.011388	1

S	42	0.6108	0.1505	0.6304	0.4102	0.3799	0.2099	1.0000	0.019232	0.5
S	43	0.8482	0.3770	0.7600	1.0000	0.0000	0.0000	1.0000	0.034987	1
S	44	0.8340	0.3808	0.5027	0.0000	1.0000	0.0000	1.0000	0.005585	1
S	45	0.6107	0.1451	0.2259	1.0000	0.0000	0.0000	1.0000	0.033832	1
S	46	0.8533	0.3739	0.3737	1.0000	0.0000	0.0000	1.0000	0.026036	0.5
S	47	1.0000	0.5011	1.0000	1.0000	0.0000	0.0000	1.0000	0.032064	0.2
S	48	1.0000	0.4904	0.7702	0.0000	1.0000	0.0000	0.5000	0.027896	0.5
S	49	0.5002	0.0000	0.2255	0.5000	0.5000	0.0000	1.0000	0.017368	0.5
S	50	0.5005	0.0000	0.0000	1.0000	0.0000	0.0000	1.0000	0.016273	0.2
S	51	0.7691	0.2433	0.6271	0.0000	1.0000	0.0000	1.0000	0.035515	1
S	52	0.7663	0.2447	0.5057	0.0000	1.0000	0.0000	1.0000	0.002018	1
S	53	0.7612	0.2341	0.3728	0.0000	1.0000	0.0000	1.0000	0.030168	1
S	54	0.8120	0.2648	0.8120	1.0000	0.0000	0.0000	1.0000	0.009134	0.5
S	55	0.9970	0.4906	0.8165	0.0000	1.0000	0.0000	0.5000	0.03414	1
S	56	0.7330	0.1846	0.1846	1.0000	0.0000	0.0000	1.0000	0.005164	0.5
S	57	0.7546	0.1396	0.6168	0.0000	1.0000	0.0000	1.0000	0.004572	1
S	58	1.0000	0.3870	1.0000	1.0000	0.0000	0.0000	1.0000	0.038332	0.2
S	59	0.6333	0.0000	0.6333	0.0000	0.0000	1.0000	1.0000	0.034813	0.25
S	60	1.0000	0.3851	0.8478	1.0000	0.0000	0.0000	1.0000	0.018075	0.5
S	61	0.6188	0.0000	0.3400	0.0000	0.0000	1.0000	1.0000	0.045286	0.5
S	62	1.0000	0.4207	0.6026	0.0000	0.0000	1.0000	1.0000	0.059987	0.5
S	63	0.6197	0.0000	0.2344	0.0000	1.0000	0.0000	1.0000	0.032525	0.5
S	64	0.6173	0.0000	0.1216	1.0000	0.0000	0.0000	1.0000	0.007151	0.5
S	65	1.0000	0.3509	0.3509	0.0000	0.0000	1.0000	1.0000	0.060805	0.5
S	66	0.6105	0.0000	0.0000	1.0000	0.0000	0.0000	1.0000	0.038066	0.2
S	67	0.8613	0.2332	0.3677	1.0000	0.0000	0.0000	1.0000	0.008294	1
S	68	0.8089	0.1129	0.6053	1.0000	0.0000	0.0000	1.0000	0.032505	1
S	69	0.8937	0.2312	0.6278	0.0000	1.0000	0.0000	1.0000	0.013581	1
S	70	0.7689	0.1210	0.3845	0.0000	1.0000	0.0000	0.5000	0.024404	1

S	71	0.8873	0.1955	0.8104	1.0000	0.0000	0.0000	1.0000	0.015815	1
S	72	0.8095	0.1150	0.4268	0.0000	1.0000	0.0000	0.5000	0.022575	1
S	73	0.8034	0.1165	0.1906	1.0000	0.0000	0.0000	1.0000	0.00778	1
S	74	0.7490	0.0000	0.7546	1.0000	0.0000	0.0000	1.0000	0.029904	0.25
S	75	1.0000	0.2606	0.2354	0.0000	1.0000	0.0000	1.0000	0.030194	0.5
S	76	1.0000	0.2705	1.0000	0.5119	0.0000	0.4881	1.0000	0.011688	0.2
S	77	0.7715	0.0000	0.6273	1.0000	0.0000	0.0000	1.0000	0.016214	0.5
S	78	1.0000	0.2347	0.7656	0.6249	0.0000	0.3751	1.0000	0.013864	0.5
S	79	0.7581	0.0000	0.5090	0.5000	0.5000	0.0000	1.0000	0.012018	0.5
S	80	1.0000	0.2320	0.6182	0.0000	1.0000	0.0000	1.0000	0.029963	0.5
S	81	0.7676	0.0000	0.3865	0.0000	1.0000	0.0000	1.0000	0.027702	0.5
S	82	1.0000	0.2305	0.4993	0.5000	0.5000	0.0000	1.0000	0.023557	0.5
S	83	0.7656	0.0000	0.2356	1.0000	0.0000	0.0000	1.0000	0.015771	0.5
S	84	1.0000	0.2331	0.3789	1.0000	0.0000	0.0000	1.0000	0.021104	0.5
S	85	0.7397	0.0000	0.0000	0.5120	0.0000	0.4880	1.0000	0.005249	0.2
S	86	0.8469	0.0000	0.8886	0.4804	0.4721	0.0475	1.0000	0.030208	0.25
S	87	0.8620	0.0000	0.7748	0.0000	1.0000	0.0000	1.0000	0.034707	0.5
S	88	1.0000	0.1152	0.6192	1.0000	0.0000	0.0000	1.0000	0.013057	0.5
S	89	0.8506	0.0000	0.3863	1.0000	0.0000	0.0000	1.0000	0.025576	0.5
S	90	0.8586	0.0000	0.1414	1.0000	0.0000	0.0000	1.0000	0.023994	0.5
S	91	0.8820	0.0000	0.6190	1.0000	0.0000	0.0000	1.0000	0.007789	0.5
S	92	1.0000	0.1186	0.3797	1.0000	0.0000	0.0000	1.0000	0.008419	1
S	93	1.0000	0.0000	1.0000	0.0000	0.0000	1.0000	1.0000	0.029466	0.025
S	94	1.0000	0.0000	0.7665	0.5003	0.0000	0.4997	1.0000	0.023321	0.1
S	95	1.0000	0.0000	0.6100	1.0000	0.0000	0.0000	1.0000	0.028762	0.1
S	96	1.0000	0.0000	0.5002	1.0000	0.0000	0.0000	1.0000	0.026407	0.1
S	97	1.0000	0.0000	0.3870	1.0000	0.0000	0.0000	1.0000	0.033026	0.1
S	98	1.0000	0.0000	0.2343	0.5036	0.0000	0.4964	1.0000	0.017773	0.1
S	99	1.0000	0.0000	0.0000	0.0000	0.0000	1.0000	1.0000	0.029022	0.025

S	100	1.0000	0.1349	0.8564	1.0000	0.0000	0.0000	1.0000	0.011128	0.5
S	101	1.0000	0.0966	0.9330	0.0000	1.0000	0.0000	0.7037	0.02959	0.5
S	102	1.0000	0.4646	0.5343	1.0000	0.0000	0.0000	0.9609	0.01795	0.5
S	103	0.5291	0.0000	0.4369	1.0000	0.0000	0.0000	0.9353	0.036378	0.5
S	104	0.9202	0.0000	0.0974	0.0000	1.0000	0.0000	0.3474	0.028711	0.5

References

[1] M. Eckert, "Max von Laue and the discovery of X-ray diffraction in 1912," *Ann. Phys.,* vol. 524, pp. A83-A85, 2012.

[2] W. H. Bragg and W. L. Bragg, "The reflectionof X-rays by crystals," *Proc. R. Soc. Lond. A.,* vol. 88, pp. 428-438, 1913.

[3] R.-J. Haüy, Essai d'une Théorie sur la Structure des Crystaux, appliauée à plusieurs genres de substances crystallisées., Paris: Gogué & Née,, 1784.

[4] E. J. Aiton, A. M. Duncan and J. V. Field, The harmony of the world, Am. Phil. Society, 1997.

[5] E. S. Fedorov, "Symmetry of Regular Systems of Figures," *Zap. Mineral. Obch.,* vol. 28, pp. 1-146, 1891.

[6] A. M. Schönflies, Theorie der Kristallstruktur., Berlin: Gebr. Bornträger",, 1891.

[7] A. L. Patterson, "A direct method for the determination of the components of interatomic distances in crystals," *Z. Kristallogr.,* vol. 90, p. 517–542, 1935.

[8] H. Hauptman, "Direct Methods and Anomalous Dispersion (Nobel Lecture)," *Angewandte Chemie International Edition,* vol. 25, pp. 603-613, 1986.

[9] J. Karle, "Recovering Phase Informationfrom Intensity Data (Nobel Lecture)," *Angewandte Chemie International Edition,* vol. 25, pp. 614-629, 1986.

[10] U. Dehlinger, "Uber die Verbreiterung der Debyelinien bei kaltbearbeiteten Metallen," *Z. Kristallogr.,* vol. 65, p. 615, 1927.

[11] G. D. Preston, "The diffraction of X-rays by age-hardening aluminium copper alloys," *Proc. Roy. Soc. A,* vol. 167, p. 526, 1938.

[12] V. Daniel and H. Lipson, "An X-ray study of the dissociation of an alloy of copper, iron and nickel," *Proc. Roy. Soc., A,* vol. 181, p. 368, 1943.

[13] M. E. Hargreaves, "Modulated structures in some copper–nickel–iron alloys," *Acta Cryst.,* vol. 4, p. 301, 1951.

[14] K. Fujiwara, "On the period of out-of-step of ordered alloys with anti-phase domain structure," *J. Phys. Soc. Japan,* vol. 12, p. 7, 1957.

[15] S. van Smaalen, Incommensurate Crystallography, Oxford University Press, IUCR Monographs on Crystallography No. 21, 2007.

[16] P. M. de Wolff, "The Pseudo-Symmetry of Modulated Crystal Structures," *Acta Cryst. A,* vol. 30, pp. 777-785, 1974.

[17] A. Janner, "Superspace Groups," in *Methods Of Structural Analysis Of Modulated Structures And Quasicrystals,* World Scientific, 1991, pp. 64-78.

[18] V. Petricek, M. Dusek and L. Palatinus, "Crystallographic Computing System JANA2006: General features," *Z. Kristallogr.,* vol. 229, pp. 345-352, 2016.

[19] D. Shechtman, I. Blech, D. Gratias and J. W. Cahn, "Metallic Phase with Long-Range Orientational Order and No Translational Symmetry," *Phys. Rev. Lett.,* vol. 53, pp. 1951-1954, 1984.

[20] D. Levine and P. J. Steinhardt, "Quasicrystals: A New Class of Ordered Structures," *Phys. Rev. Lett.,* vol. 53, p. 2477, 1984.

[21] A. L. Mackay, "Crystallography and the Penrose pattern," *Physica A,* vol. 114, pp. 609-613, 1982.

[22] M. Senechal, "The mysterious Mr. Ammann," *Math. Intelligencer,* vol. 26, p. 10, 2004.

[23] R. Penrose, "The role of aesthetics in pure and applird mathematical research," *Bull. Inst. Math. Appl.,* vol. 10, pp. 266-271, 1974.

[24] L. Pauling, "Apparent icosahedral symmetry is due to directed multiple twinning of cubic crystals," *Nature,* vol. 317, pp. 512-514, 1985.

[25] P. A. Bancel, P. A. Heiney, P. W. Stephens and A. I. Goldman, "Structure of Rapidly Quenched Al-Mn," *Phys. Rev. Lett.,* vol. 54, p. 2422, 1985.

[26] A.-. P. Tsai, "A Stable Quasicrystal in Al-Cu-Fe System," *Jpn. J. Appl. Phys.,* vol. 26, p. 1505, 1987.

[27] IUCr, "Report of the Executive Committee for 1991," *Acta Cryst. A,* vol. 48, pp. 922-946, 1992.

[28] H. Bohr, "Zur Theorie der fastperiodischen Funktionen I," *Acta Math.,* vol. 45, pp. 29-127, 1925.

[29] J. Wolny, I. Buganski and R. Strzalka, "Diffraction pattern of modulated structures described by Bessel functions," *Philos. Mag.,* vol. 96, pp. 1-16, 2016.

[30] R. Lifshitz, "The square Fibonacci tiling," *J. All. Comp.,* vol. 342, pp. 186-190, 2002.

[31] S. Coates, J. A. Smerdon, R. McGrath and H. R. Sharma, "A molecular overlayer with the Fibonacci square grid structure," *Nat. Comm.,* vol. 9, p. 3435, 2018.

[32] R. Lifshitz, "Quasicrystal: A matter of definition," *Found. Phys.,* vol. 33, pp. 1703-1711, 2003.

[33] R. Lifshitz, "What is a crystal?," *Z. Kristallogr.,* vol. 222, pp. 313-317, 2007.

[34] W. Steurer, "Quasicrystals: What do we know? What do we want to know? What can we know?," *Acta Cryst. A,* vol. 74, pp. 1-11, 2018.

[35] L. Bindi, P. J. Stainhardt, N. Yao and P. J. Lu, "Natural Quasicrystals," *Science,* vol. 324, pp. 1306-1309, 2009.

[36] L. Bindi, C. Lin, P. J. Steinhardt and C. Ma, "Collisions in outer space produced an icosahedral phase in the Khatyrka meteorite never observed previously in the laboratory," *Scientific Reports,* vol. 6, p. 38117, 2016.

[37] L. Bindi, N. Yao, C. Lin, L. S. Hollister and C. L. Andronicos, "Natural quasicrystal with decagonal symmetry," *Sci. Rep.,* vol. 5, p. 911, 2015.

[38] L. Bindi, J. M. Eiler, Y. Guan, L. S. Hollister and G. MacPherson, "Evidence for the extraterrestrial origin of a natural quasicrystal," *Proc. Natl Acad. Sci. USA,* vol. 109, p. 1396–1401, 2012.

[39] W. Steurer, "Twenty years of structure research on quasicrystals. Part 1. Pentagonal, octagonal,," *Z. Kristallogr.,* vol. 219, pp. 391-446, 2004.

[40] J. Daams and P. Villars, "Atomic environments in relation to compound prediction," *Eng. Appl. Artif. Intell.,* vol. 13, pp. 507-511, 2000.

[41] S. Ben-Abraham and F. Gähler, "Covering cluster description of octagonal MnSiAl quasicrystals," *Phys. Rev. B,* vol. 60, pp. 860-864, 1999.

[42] T. Ishimasa, H. -U. Nissen and Y. Fukano, "New ordered state between crystalline and amorphous in Ni-Cr particles," *Phys. Rev. Lett.,* vol. 55, p. 511, 1985.

[43] S. Förster, K. Meinel, R. Hammer, M. Trautman and W. Widdra, "Quasicrystalline structure formation in a classical crystalline thin-film system," *Nature,* vol. 502, pp. 215-218, 2013.

[44] L. Elcoro and J. M. Perez-Mato, "Cubic superspace symmetry and inflation rules in metastable MgAl alloy," *Eur. Phys. J. B,* vol. 7, pp. 85-89, 1999.

[45] A. J. Bradley and H. J. Goldschmidt, "An X-ray study of slowly-cooled iron-copper-aluminium alloys. Part II. - Alloys rich in aluminium.," *J. Inst. Met.,* vol. 65, pp. 195-210, 1939.

[46] H. K. Hardy and J. M. Silcock, "The phase sections at 500C and 350C of aluminium-rich aluminium-copper-lithium alloys," *J. Inst. Met.,* vol. 84, pp. 423-428, 1956.

[47] B. Dubost, J. M. Lang, M. Tanaka, P. Sainfort and M. Audier, "Large AlCuLi Single Quasi-Crystals with Triacontahedral Solidification Morphology," *Nature,* vol. 324, pp. 48-50, 1986.

[48] A. Palenzona, "Ytterbium-Cadmium System," *J. Less.-Comm. Met.,* vol. 25, pp. 367-372, 1971.

[49] G. Bruzzone, "Ca-Cd and Ba-Cd Systems," *Gaz. Chim. Ital.,* vol. 102, pp. 234-242, 1972.

[50] J. Q. Guo, E. Abe and A. P. Tsai, "Stable icosahedral quasicrystals in binary Cd-Ca and Cd-Yb systems," *Phys. Rev. B,* vol. 62, p. R14605, 2000.

[51] A. P. Tsai, J. Q. Guo, E. Abe, H. Takakura and T. J. Sato, "A stable binary quasicrystal," *Nature,* vol. 408, pp. 537-538, 2000.

[52] A. L. Mackay, "A dense non-crystallographic packing of equal spheres," *Acta Cryst.,* vol. 15, pp. 916-918, 1962.

[53] G. Bergman, J. L. T. Waugh and L. Pauling, "Crystal structure of the intermetallic compound Mg32 (Al, Zn)49 and related phases," *Nature,* vol. 169, pp. 1057-1058, 1952.

[54] W. Steurer and S. Deloudi, Crystallography of Quasicrystals: Concepts, Methods and Strucutres, Springer, 2009.

[55] F. C. Frank and J. S. Kasper, "Complex alloy structures regarded as sphere packings. I. Definitions and basic principles," *Acta Cryst.,* vol. 11, p. 184, 1958.

[56] V. V. Molokanov and V. N. Chebotnikov, "Quasicrystals and amorphous alloys in Ti-Zr-Ni system: glassforming ability, structure and properties," *J. Non-Cryst. Solids,* vol. 117/118, pp. 789-792, 1990.

[57] K. F. Kelton, W. J. Kim and R. M. Stroud, "A stable Ti-based quasicrystal," *App. Phys. Lett.,* vol. 70, p. 3230, 1997.

[58] C. L. Henley and V. Elser, "Quasicrystal structure of (Al, Zn)49Mg32," *Phil. Mag. B,* vol. 53, pp. L59-L66, 1986.

[59] K. Kmiya, T. Takeuchi, N. Kabeya, N. Wada, T. Ishimasa, A. Ochiai, K. Deguchi, K. Imura and N. K. Sato, "Discovery of superconductivity in quasicrystal," *Nature Comm.,* vol. 9, p. 154, 2018.

[60] P. C. Canfield, M. L. Caudle, C. S. Ho, A. Kreyssing and S. Nandi, "Solution growth of a binary icosahedral quasicrystal of Sc12Zn88," *Phys. Rev. B,* vol. 81, p. 020201, 2010.

[61] T. Yamada, H. Takakura, H. Euchner, C. P. Gomez, A. Bosak, P. Fertey and M. de Boissieu, "Atomic structure and phason modes of the Sc–Zn icosahedral quasicrystal," *IUCrJ,* vol. 3, pp. 247-258, 2016.

[62] H. Takakura, C. P. Gomez, A. Yamamoto, M. de Boissieu and A. Tsai, "Atomic structure of the binary icosahedral," *Nat. Mat.,* vol. 6, pp. 58-63, 2007.

[63] W. Hume-Rothery, "Research on the Nature, Properties and Conditions of Formation of Intermetallic Compounds, with Special Reference to Certain Compounds of Tin," *J. Inst. Metals,* vol. 35, pp. 295-299, 1926.

[64] K. M. Rabe, A. Kortan, J. Phillips and P. Villars, "Quantum diagrams and the prediction of new ternary quasicrystals," *Phys. Rev. B,* vol. 43, p. 6280, 1991.

[65] A. P. Tsai, "Metallurgy of Quasicrystals," in *Physical Properties of Quasicrystals*, Heidelberg, Springer, 1998, pp. 5-50.

[66] Y. Kaneko, Y. Arichika and T. Ishimasa, "Icosahedral quasicrystal in annealed Zn–Mg–Sc alloys," *Phil. Mag. Lett.,* vol. 81, pp. 777-787, 2001.

[67] M. Engel, P. F. Damasceno, C. L. Phillips and S. C. Glotzer, "Computational self-assembly of a one-component icosahedral quasicrystal," *Nat. Mat.,* vol. 14, pp. 109-116, 2015.

[68] P. Subramanian, A. J. Archer, E. Knobloch and A. M. Rucklidge, "Spatially localized quasicrystalline structures," *New. J. Phys.,* vol. 20, p. 122002, 2018.

[69] S. Alexander and J. McTague, "Should All Crystals Be bcc? Landau Theory of Solidification and Crystal Nucleation," *Phys. Rev. Lett.,* vol. 41, p. 702, 1978.

[70] L. Bendersky, "Quasicrystal with One-Dimensional Translational Symmetry and a Tenfold," *Phys. Rev. Lett.,* vol. 55, pp. 1461-1463, 1985.

[71] K. Chattopadhyay, S. Ranganathan, Subanna G. N. and N. Thangaraj, "Electron-Microscopy of Quasi-Crystals in Rapidly Solidified Al-14-Percent Mn Alloys," *Scr. Met.,* vol. 19, pp. 767-771, 1985.

[72] M. Khaidar, C. H. Allibert and J. Driole, "Phase-Equilibria of the Fe-Ni-Al System for Al Content above 50 at-Percent and Crystal-Structures of Some Ternary Phases," *Z. Metkd.,* vol. 73, pp. 433-438, 1982.

[73] U. Lemmerz, B. Grushko, C. Freiburg and M. Jansen, "Study of Decagonal Quasi-Crystalline Phase-Formation in the Al-Ni-Fe Alloy System," *Philos. Mag. Lett.*, vol. 69, pp. 141-146, 1994.

[74] L. X. He, Z. Zhang, Y. K. Wu and K. H. Kuo, "Stable decagonal quasi-crystals with differen tperiodicities along the tenfold axis in Al65Cu20Co15," *Inst. Phys. Conf. Ser.*, vol. 93, pp. 501-502, 1988.

[75] S. P. Ge and K. H. Kuo, "Icosahedral and stable decagonal quasicrystals in Ga46Fe23Cu23Si8, Ga50Co25Cu25 and Ga46V23Ni23Si8," *Phil. Mag. Lett.*, vol. 75, pp. 245-253, 1997.

[76] W. Steurer and K. H. Kuo, "5-Dimensional Structure-Analysis of Decagonal Al65Cu20Co15," *Acta Cryst. B,* vol. 46, pp. 703-712, 1990.

[77] E. Cockayne and M. Widom, "Ternary model of an Al-Cu-Co decagonal quasicrystal," *Phys. Rev. Lett.*, vol. 81, pp. 598-601, 1998.

[78] S. E. Burkov, "Strucutre Model of the Al-Cu-Co Decagonal Quasicrystal," *Phys. Rev. Lett.*, vol. 67, pp. 614-617, 1991.

[79] T. C. Lubensky, S. Ramaswamy and J. Toner, "Hydrodynamics of icosahedral quasicrystals," *Phys. Rev. B,* vol. 32, pp. 7444-7452, 1985.

[80] T. C. Lubensky, J. E. S. Socolar, P. J. Steinhardt, P. A. Bancel and P. A. Heiney, "Distortion and Peak Broadening in Quasicrystal Diffraction Patterns," *Phys. Rev. Lett.*, vol. 57, p. 1440, 1986.

[81] S. Taniguchi and E. Abe, "Highly-perfect decagonal quasicrystalline Al64Cu22Co14 with non-centrosymmetry," *Philos. Mag.*, vol. 88, pp. 1949-1958, 2008.

[82] P. Kuczera, W. Steurer and J. Wolny, "Comparative structural study of decagonal quasicrystals in the systems Al-Cu-Me (Me = Co, Rh, Ir)," *Acta Cryst. B,* vol. 68, pp. 578-589, 2012.

[83] I. Buganski, R. Strzalka and J. Wolny, "Phason-flips refinement of and multiple-scattering correction for the d-AlCuRh quasicrystal," *Acta Cryst. A,* vol. 75, pp. 352-361, 2019.

[84] R. Strzalka, I. Buganski, P. Kuczerka, L. Pytlik and J. Wolny, "Atomic Structure of Decagonal Al-Cu-Rh Quasicrystal–Revisited: New Correction for Phonons," *Crystals*, vol. 9, p. 78, 2019.

[85] N. Wang, H. Chen and K. H. Kuo, "Two-Dimensional Quasicrystal With Eightfold Rotational Symmetry," *Phys. Rev. Lett.*, vol. 59, pp. 1010-1013, 1987.

[86] W. Cao, H. Q. Ye and K. H. Kuo, "New Octagonal Quasicrystal and Related Crystalline Phases in Rapidly Solidified Mn4Si," *Phys. Stat. Solidi A,* vol. 107, pp. 511-519, 1988.

[87] N. Wang, K. K. Fung and K. H. Kuo, "Symmetry Study of the Mn-Si-Al Octagonal Quasicrystal by Convergent Beam Electron-Diffraction," *Appl. Phys. Lett,* vol. 52, pp. 2120-2121, 1988.

[88] Z. M. Wang and K. H. Kuo, "The Octagonal Quasilattice and Electron-Diffraction Patterns of the Octagonal Phase.," *Acta Cryst. A,* vol. 44, pp. 857-863, 1988.

[89] Z. Huang and S. Hovmoeller, "An Octagonal Quasicrystal Structure Model With 8_3 Screw Axes," *Philos. Mag. Lett.,* vol. 64, pp. 83-88, 1991.

[90] J. C. Jiang, S. Hovmoeller and X. D. Zou, "A 3-Dimensional Structure Model of 8-Fold Quasicrystals Obtained by High-Resolution Electron-Microscopy," *Philos. Mag. Lett,* vol. 71, pp. 123-129, 1995.

[91] L. Petti, M. Rippa, R. Capasso, J. Zhou and M. G. Maglione, "Plasmonic octagonal quasicrystals for surface enhanced Raman sensing," *Adv. Device Mater.,* vol. 1, pp. 47-51, 2015.

[92] T. Ishimasa, "Dodecagonal Quasicrystals Still in Progress," *Isr. J. Chem.,* vol. 51, pp. 1216-1225, 2011.

[93] N. Niizeki and H. Mitani, "Two-dimensional dodecagonal quasilattices," *J. Phys. A Math. Gen.,* vol. 20, p. L405, 1987.

[94] F. Gähler, "Crystallography of Dodecagonal Quasicrystal," in *Quasicrystalline Materials, Proceeding of the I.*, Singapore, World Scientific, 1988, pp. 272-284.

[95] P. Stampfli, "A dodecagonal quasiperiodic lattice in two dimensions," *Helv. Phys. Acta.,* vol. 59, pp. 1260-1263, 1986.

[96] M. Oxborrow and C. L. Henley, "Random square-triangle tilings: A model for twelvefold-symmetric quasicrystals," *Phys. Rev. B,* vol. 48, p. 6966, 1993.

[97] H. Chen, D. X. Li and K. H. Kuo, "New type of two-dimensional quasicrystal with twelvefold rotational symmetry.," *Phys. Rev. Lett.,* vol. 60, pp. 1645-1648, 1988.

[98] M. Conrad, F. Krumeich and B. Harbrecht, "A Dodecagonal Quasicrystalline Chalcogenide," *Angew. Chem. Int. Ed.,* vol. 37, pp. 1383-1386, 1998.

[99] S. Iwami and T. Ishimasa, "Dodecagonal quasicrystal in Mn-based quaternary alloys containing Cr, Ni and Si," *Phil. Mag. Lett.,* vol. 95, pp. 229-236, 2015.

[100] S. Schenk, S. Förster, K. Meinel, R. Hammer and B. Leibundgut, "Observation of a dodecagonal oxide quasicrystal and its complex approximant in the SrTiO3-Pt(1 1 1) system," *J.Phys. Condens. Matt.,* vol. 29, p. 134002, 2018.

[101] S. Schenk, E. M. Zollneer, O. Krahn, B. Schreck, R. Hammer, S. Förster and W. Widdra, "Full real-space analysis of a dodecagonal quasicrystal," *Acta Cryst. A,* vol. 75, pp. 307-313, 2018.

[102] A. Katz and D. Gratias, "A geometric approach to chemical ordering in icosahedral structures," *J. Non-Crystalline Solids,* Vols. 153-154, p. 187, 1993.

[103] H. B. Elswijk, J. T. M. De Hosson, S. van Smaalen and J. L. de Boer, "Determination of the crystal structure of icosahedral Al-Cu-Li," *Phys. Rev. B,* vol. 38, p. 1681, 1988.

[104] A. Yamamoto, "Ideal structure of icosahedral Al-Cu-Li quasicrystals," *Phys. Rev. B,* vol. 45, p. 5217, 1992.

[105] F. C. Frank and J. S. Kasper, "Complex alloy structures regarded as sphere packings. II. Analysis and classification of representative structures," *Acta Cryst.,* vol. 12, pp. 483-499, 1959.

[106] P. Kramer and R. Neri, "On periodic and non-periodic space fillings of E^m obtained by projection," *Acta Cryts. A,* vol. 40, pp. 580-587, 1985.

[107] L. Palatinus, "Ab Initio Determination of Incommensurately Modulated Structures by Charge Flipping in Superspace," *Acta Cryst. A,* vol. 60, pp. 604-610, 2004.

[108] A. Yamamoto, "Crystallography of Quasiperiodic Crystals," *Acta Cryst. A,* vol. 52, pp. 509-560, 1996.

[109] A. Yamamoto, "Software package for structure analysis of quasicrystals.," *Sci. Technol. Adv. MAter.,* vol. 6, p. 013001, 2008.

[110] A. Katz and M. Duneau, "Quasiperiodic patterns and icosahedral symmetry," *J. Phys. France,* vol. 47, pp. 181-196, 1986.

[111] P. A. Kalugin, A. Y. Kitaev and L. S. Levitov, "Al0.86Mn0.14: A six-dimensional crystal," *JETP Lett.,* vol. 41, p. 145, 1985.

[112] V. Elser, "The diffraction pattern of projected strucutres," *Acta Cryst. A,* vol. 42, pp. 36-43, 1986.

[113] P. Bak, "Symmetry, stability, and elastic properties of icosahedral incommensurate crystals," *Phys. Rev. B,* vol. 32, p. 5764, 1985.

[114] J. Wolny, "The reference lattice concept and its application to the analysis of diffraction patterns," *Pjil. Mag. A,* vol. 77, pp. 395-412, 1998.

[115] J. Wolny, B. Kozakowski, P. Kuczera, L. Pytlik and R. Strzalka, "What periodicities can be found in diffraction patterns of quasicrystals?," *Acta Cryst. A,* vol. 70, p. 181, 2014.

[116] J. Wolny, Kwazikryształy i inne dwuwymiarowe układy o zabronionej symetrii, zeszyty naukowe, Krakow: AGH, 1991.

[117] B. Souvignier, "Enantiomorphism of crystallographic groups in higher dimensions with results in dimensions up to 6," *Acta Cryst. A,* vol. 59, pp. 210-220, 2003.

[118] D. S. Rokhar, N. D. Mermin and D. C. Wright, "The Two-dimensional Quasicrystallographic Space Groups less than 23-fold," *Acta Cryst. A,* vol. 44, pp. 197-211, 1988.

[119] L. S. Levitov and J. Rhyner, "Crystallography of Quasicrystals; Application to Icosahedral Symmetry," *J. Phys. France,* vol. 49, pp. 1835-1849, 1988.

[120] M. Kleman and A. Pavlovitch, "Generalized 2D Penrose tilings: structural properties," *J. Phys. A: Math. Gen.,* vol. 20, p. 687, 1987.

[121] K. N. Ishikara and A. Yamamoto, "Penrose patterns and related structures. I. Superstructure and generalized Penrose patterns," *Acta Cryst. A,* vol. 44, pp. 508-516, 1988.

[122] M. Chodyn, P. Kuczera and J. Wolny, "Generalized Penrose tilings as a quasilattice for decagonal quasicrystal strucutre analyssis," *Acta Cryst. A,* vol. 71, pp. 161-168, 2015.

[123] M. Chodyn, P. Kuczera and J. Wolny, "Direct and Reciprocal Space Properties of the Generalized Penrose Tilings," *Acta Phys. Pol. A,* vol. 126, pp. 442-445, 2014.

[124] J. Wolny, "Average Unit Cell of the Fibonacci Chain," *Acta Cryst. A,* vol. 54, pp. 1014-1018, 1998.

[125] B. Kozakowski and J. Wolny, "Structure factor for decorated Penrose tiling in physical space," *Acta Cryst. A,* vol. 66, pp. 489-498, 2010.

[126] R. Strzalka, I. Buganski and J. Wolny, "Structure factor for an icosahedral quasicrystal within a statistical approach," *Acta Cryst. A,* vol. 71, pp. 279-290, 2015.

[127] P. Kuczera, J. Wolny, F. Fleischer and W. Steurer, "Structure refinement of decagonal Al-Ni-Co, superstructure type I," *Philos. Mag. A,* vol. 91, pp. 2500-2509, 2011.

[128] I. Buganski, R. Strzalka and J. Wolny, "The estimation of phason flips in 1D quasicrystal from the diffraction pattern," *Phys. Stat. Sol. B,* vol. 253, pp. 450-457, 2015.

[129] J. Wolny, I. Buganski, P. Kuczera and R. Strzalka, "Pushing the limits of crystallography," *J. app. Cryst.,* vol. 46, pp. 2106-2115, 2016.

[130] I. Buganski, M. Chodyn, R. Strzalka and J. Wolny, "The order-disorder evolution in quasicrystals through phason flips," *J. All. Comp.,* vol. 710, pp. 92-101, 2017.

[131] J. Wolny, A. Wnek, J.-L. Verger-Gaugry and L. Pytlik, "Average unit-cell approach to diffraction on Thue–Morse sequence and decorated quasicrystals," *Mat. Sci. Eng. A,* vol. 294, p. 381, 2000.

[132] J. Wolny, I. Buganski and R. Strzalka, "Model refinement of quasicrystals," *Cryst. Rev.,* vol. 24, pp. 22-64, 2018.

[133] B. Kozakowski, J. Wolny and P. Kuczera, "Structure of Quasicrystals Described by the Statistical Methods," *Phil. Mag.,* vol. 88, pp. 1921-1927, 2008.

[134] J. E. Socolar and P. J. Steinhardt, "Quasicrystals. II. Unit-cell configuration," *Phys. Rev. B,* vol. 34, p. 617, 1986.

[135] J. E. S. Socolar, P. J. Steinhardt and D. Levine, "Quasicrystals with arbitrary orientational symmetry," *Phys. Rev. B,* vol. 32, p. 5547, 1985.

[136] N. de Bruijn, *Ned. Akad. Weten. Proc. Ser. A,* vol. 43, pp. 27, 39, 53, 1981.

[137] A. E. Madison, "Substitution rules for icosahedral quasicrystals," *RSC Adv.,* vol. 5, p. 5745, 2015.

[138] A. E. Madison, "Looking for alternatives to the superspace description of icosahedral quasicrystals," *Proc. R. Soc. A,* vol. 475, p. 20180667, 2019.

[139] L. S. Levitov, "Local rules for quasicrystals," *Commun. Math. Phys.,* vol. 119, p. 627, 1988.

[140] C. T. Hann, J. S. Socolar and P. J. Steinhardt, "Local growth of icosahedral quasicrystalline tillings," *Phys. Rev. B,* vol. 94, p. 014113, 2016.

[141] J. W. Cahn, D. Shechtman and D. Gratias, "Indexing of icosahedral quasiperiodic crystals," *J. Mater. Res.,* vol. 1, pp. 13-26, 1986.

[142] M. Mihalkovic and P. Mrafko, "Tiling of canonical cells: AlMnSi quasicrystal model," *J. Non.-Cryst. Sol.,* Vols. 156-158, p. 936, 1993.

[143] I. Buganski, J. Wolny and H. Takakura, "The atomic structure of the Bergman-type icosahedral quasicrystal based on the Ammann–Kramer–Neri tiling," *Acta Cryst. A,* vol. 76, pp. 180-196, 2020.

[144] T. Ogawa, "On the Structure of a Quasicrystal –Three-Dimensional Penrose Transformation," *J. Phys. Soc. Jpn.,* vol. 54, pp. 3205-3208, 1985.

[145] C. S. Herz, "Fourier Transforms Related to Convex Sets," *Ann. Math.,* vol. 75, pp. 81-92, 1962.

[146] A. van Oosterom and J. Strackee, "The Solid Angle of a Plane Triangle," *IEEE Trans Biomed Eng.,* Vols. BME-30, pp. 125-126, 1983.

[147] D. Levine, T. C. Lubensky, S. Ostlund, S. Ramaswamy, P. J. Steinhardt and J. Toner, "Elasticity and Dislocations in Pentagonal and Icosahedral Quasicrystals," *Phys. Rev. Lett.,* vol. 54, p. 1520, 1985.

[148] M. de Boissieu, S. Francoual, M. mihalkovic, K. Shibata and A. Q. R. Baron, "Lattice dyna-mics of the Zn–Mg–Sc icosahedral quasicrystal and its Zn–Scperiodic 1/1 approximant," *Nat. Mat.,* vol. 6, pp. 977-984, 2007.

[149] F. Dugain, M. de Boissieu, K. Shibata, R. Currat and T. J. Sato, "Inelastic neutron scattering study of the dynamics of the AlNiCo decagonal phase," *Eur. Phys. J. B,* vol. 7, pp. 513-516, 1999.

[150] M. Krajci and J. Hafner, "Elementary excitations in quasicrystals," *J. Non-Cryst. Solids,* vol. 156, pp. 887-890, 1993.

[151] T. Janssen and O. Radulescu, "Theory of Phasons in Aperiodic Crystals," *Ferroelectrics,* vol. 305, pp. 179-184, 2004.

[152] P. A. Bancel, "Dynamical phasons in a perfect quasicrystal.," *Phys. Rev. Lett.,* vol. 63, p. 2741, 1989.

[153] A. Kiselev, M. Engel and H.-R. Trebin, "Confirmation of the Random Tiling Hypothesis for a Decagonal Quasicrystal," *Phys. Rev. Lett.,* vol. 109, p. 225502, 2012.

[154] K. Nagao, T. Inzuka, K. Nishimoto and K. Edagawa, "Experimental Observation of Quasicrystal Growth," *Phys. Rev. Lett.,* vol. 115, p. 075501, 2015.

[155] C. L. Henley, V. Elser and M. Mihalkovic, "Structure determinations for random-tiling quasicrystals," *Z. Kristallogr.,* vol. 215, p. 553, 2000.

[156] A. Niikura, A. P. Tsai, A. Inoue, T. Masumoto and A. Yamamoto, "Novel Face-Centered Icosahedral Phase in Al-Mg-Li System," *Jpn. J. App. Phys.,* vol. 32, p. L1106, 1993.

[157] N. Koshikawa, S. Sakamoto, K. Edagawa and S. Takeuchi, "New Stable Icosahedral Quasicrystal in Mg-Pd-Al System," *Jpn. J. App. Phys.,* vol. 31, p. L966, 1992.

[158] Z. Luo, S. Zhang, Y. Tang and D. Zhao, "Quasicrystals in as-cast Mg-Zn-RE alloys," *Scr. Metall.,* vol. 28, p. 1513, 1993.

[159] A. Niikura, A. P. Tsai, A. Inoue and T. Masumoto, "Stable Zn-Mg-rare-earth face-centred icosahedral alloys with pentagonal dodecahedral solidification morphology," *Phil. Mag. Lett.,* vol. 69, pp. 351-355, 1994.

[160] A. Niikura, A. P. Tsai, A. Inoue and T. Masumoto, "New class of amorphous and icosahedral phases in Zn–Mg–rare-earth metal alloys," *Jpn. J. App. Phys.,* vol. 33, p. L1538, 1994.

[161] T. J. Sato, E. Abe and A. P. Tsai, "Composition and stability of decagonal quasicrystals in the Zn-Mg-rare-earth systems," *Phil. Mag. Lett.,* vol. 77, pp. 213-219, 1998.

[162] A. P. Tsai, A. Yamamoto, A. Niikura, A. Inoue and T. Masumoto, "Structural model of a face-centred icosahedral phase in Al-Mg-Li alloys," *Phil. Mag. Lett.,* vol. 69, p. 343, 1994.

[163] V. Elser and C. L. Henley, "Crystal and quasicrystal structures in Al-Mn-Si alloys," *Phys. Rev. Lett.,* vol. 55, p. 2883, 1985.

[164] H. Takakura and A. Yamamoto, "An interpenetrated cluster model of p-type Zn–Mg–Ho icosahedral quasicrystal," *Phil. Mag.,* vol. 87, p. 2713, 2007.

[165] H. Takakura, M. Shiono, T. J. Sato, A. Yamamoto and A. P. Tsai, "Ab Initio Structure Determination of Icosahedral Zn-Mg-Ho Quasicrystals by Density Modification Method," *Phys. rev. Lett.,* vol. 86, p. 236, 2001.

[166] H. Takakura, A. Yamamoto, T. Sato, A. P. Tsai and Y. Ozawa, "Ab initioreconstruction of p-type icosahedral Zn-Mg-Ho quasicrystal structures," *Phil. Mag.,* vol. 86, p. 621, 2006.

[167] G. Kreiner, "Towards realistic quasiperiodic structures: modelling, synthesis and structure of (Ga,Zn)175−δMg97+δ — a large 3/2–2/1–2/1 Fibonacci approximant," *J. All. Comp.,* vol. 338, p. 261, 2002.

[168] K. Sugiyama, W. Sun and K. Hiraga, "Crystal structure of a cubic Al17Zn37Mg46; a 2/1 rational approximant structure for the Al–Zn–Mg icosahedral phase," *J. All. Comp.,* vol. 342, p. 139, 2002.

[169] C. P. Gomez and S. Lindi, "Structure of Ca(13)Cd(76): A Novel Approximant to the MCd(5.7) Quasicrystals (M=Ca, Yb)," *Angew Chem Int Ed Engl.,* vol. 40, p. 4037, 2001.

[170] C. P. Gomez and S. Lindi, "Comparative structural study of the disordered MCd/sub 6/quasicrystal approximants," *Phys. Rev. B,* vol. 68, p. 024203, 2003.

[171] A. I. Goldman, "Magnetism in icosahedral quasicrystals: current status and open questions," *Sci. Tech. Adv. Mater.,* vol. 15, p. 044801, 2014.

[172] T. J. Sato, "Short-range order and spin-glass-like freezing in A–Mg–R (A = Zn or Cd; R = rare-earth elements) magnetic quasicrystals," *Acta Cryst. A,* vol. 61, pp. 39-50, 2005.

[173] P. C. Canfield and Z. Fisk, "Growth of single crystals from metallic fluxes," *Phil. Mag. B,* vol. 65, p. 1117, 1992.

[174] Rigaku Oxford Diffraction, „CrysAlisPro Software System," Yarnton, Oxford, 2015.

[175] G. Oszlanyi and A. Suto, "Ab initio structure solution by charge flipping," *Acta Cryst. A,* vol. 60, p. 134, 2004.

[176] T. Janssen, G. Chapuis and M. de Boissieu, Aperiodic Crystals: From Modulated Phases to Quasicrystal: Strucutre and Properties, United Kingdom: Oxford University Press, 2018.

[177] S.-Y. Qiu and M. V. Jaric, "Atomic-structure model of i-(Al0.570Cu0.108Li0.322)," *Phys. Rev. B,* vol. 52, p. 894, 1995.

[178] S.-Y. Qiu, C. R. Rowell and M. V. Jaric, "Visualization and analysis of quasicrystal densities," *Comp. in Phys.,* vol. 10, p. 154, 1996.

[179] P. Buczek and J. Wolny, "Physical space description of decorated 1D aperiodic sequences," *Phys. Mag.,* vol. 86, p. 4181, 2006.

[180] P. Coppens and W. C. Hamilton, "Anisotropic extinction corrections in the Zachariasen approximation," *Acta Cryst. A,* vol. 26, pp. 71-83, 1970.

[181] C. P. Gomez, S. Ohhashi, A. Yamamoto and A. P. Tsai, "Disordered structures of the Tm-Mg0Zn 1/1 quasicrystal approximants (TM=Hf, Zr, Ti) and chemical intergrowth," *Inorg. Chem.,* vol. 47, p. 8258, 2008.

[182] C. L. Henley, in *Quasicrystals: The State of Art,* Singapore, World Scientific, 1991, p. 429.

[183] P. Gummelt, "Penrose tilings as coverings of congruent decagons," *Geometricae Dedicata,* vol. 62, pp. 1-17, 1996.

[184] M. Audier, J. Pannetier, M. Leblanc, C. Janot, J. M. Lang and B. Dubost, "An approachto the structure of quasicrystals: A single crystal x-ray and neutron diffraction studyof the R-Al5CuLi3phase," *Physica B,* vol. 153, p. 136, 1988.

[185] Q. Lin and D. Corbett, "New building blocks in the 2/1 crystalline," *PANS,* vol. 103, p. 13589, 2006.

[186] M. A. Ruderman and C. Kittel, "Indirect Exchange Coupling of Nuclear Magnetic Moments by Conduction Electrons," *Phys. Rev.,* vol. 96, p. 99, 1954.

[187] T. Kasuya, "A Theory of Metallic Ferro- and Antiferromagnetism on Zener's Model," *Prog. Theor. Phys.,* vol. 16, p. 45, 1956.

[188] K. Yoshida, "Magnetic Properties of Cu-Mn Alloys," *Phys. Rev.,* vol. 106, p. 893, 1957.

[189] A. I. Goldman and R. F. Kelton, "Quasicrystals and Crystalline Approximants," *Rev. Mod. Phys.,* vol. 65, pp. 213-230, 1993.

[190] I. Buganski, K. Toyonaga, H. Takakura, T. Yamada, M. de Boissieu, O. Perez, P. Fertey and J. Wolny, "The structure solution of the F-type i-ZnMgHf from the X-ray diffraction," *Mat. Sci. Eng.,* 2019.

[191] T. Yamada, H. Takakura, M. de Boissieu and A. Tsai, "Atomic structures of ternary Yb–Cd–Mg icosahedral quasicrystals and a 1/1 approximant," *Acta Cryst. B,* vol. 73, p. 1125, 2017.

[192] J. Hasegawa, S. Takeuchi and A. P. Tsai, "Stable quasicrystals and approximants in Zn–Mg–Zr and Zn–Mg–Hf alloys," *Phil. Mag. Lett.,* vol. 85, pp. 289-297, 2005.

[193] S. Ohhashi, E. Abe, M. Tanaka and A. P. Tsai, "Phase formation and structures of quasicrystals and approximants in the Zn–Mg–(Ti, Zr, Hf) system," *Acta Mater.,* vol. 57, pp. 4727-4735, 2009.

[194] T. Orsulova and P. Palcek, "Changes in hardness of magnesium alloys due to precipitation hardening," *Production Engineering Archives,* vol. 18, pp. 46-49, 2018.

[195] S. M. Zhu, J. F. Nie, M. A. Gibson, M. A. Easton and P. Bakke, "Microstructure and Creep Behavior of High-Pressure Die-Cast Magnesium Alloy AE44," *Met. Mat. Trans.,* vol. 43, pp. 4137-4144, 2012.

[196] A. Singh, "Tailoring microstructure of Mg–Zn–Y alloys with quasicrystal and related phases for high mechanical strength," *Sci. Tech. Adv. Mater.,* vol. 15, p. 044803, 2014.

[197] F. Laves and H. Witte, "Die Kristallstruktur des MgNi2 und seine Beziehungen zu den Typen MgCu2 und MgZn2," *Metallwirtsch. Metallwiss. Metalltech.*, vol. 14, pp. 645-649, 1935.

List of Conference Presentations

1. P. Kuczera, **I. Bugański**, W. Steurer., J. Wolny, *Atomic structure of decagonal Al-Cu-Me (Me =Co, Rh, Ir) quasicrystals*, 55th Polish Crystallographic Meeting, 27-28 June 2013, Wroclaw, Poland, **poster**
2. **I. Bugański**, R. Strzalka, J. Wolny, *Diffraction patterns of icosahedral quasicrystal using Average Unit Cell approach*, 12th International Conference on Quasicrystals, 1-6th September 2013, Krakow, Poland, book of abstracts, P-84, **poster**
3. **I. Bugański**, R. Strzalka, J. Wolny *Structure factor for arbitrarily decorated Ammann tiling in the Average Unit Cell approach,* C-MAC Days 2013, 9-12th December 2013, Ljubljana, Slovenia, **poster**
4. **I. Bugański**, J. Wolny, *The power series expansion of the characteristic function for Fibonacci chain probability distribution*, 56th Polish Crystallographic Meeting, 26-27th June 2014, Wroclaw, Poland, **poster**
5. **I. Bugański**, R. Strzalka, J. Wolny, *The structure factor for arbitrarily decorated Ammann tiling in the average unit cell approach*, IV AGH-HU joint symposium, September 2014, Krakow, Poland, **oral**
6. **I. Bugański**, J. Wolny, *The characteristic function for Fibonacci chain probability distribution with flips in LS sequence*, C-MAC days 2014, 8-11th December 2014, Zagreb, Croatia, **poster**
7. **I. Bugański**, R. Strzalka, J. Wolny, *Estimation of the flip ratio in the 1D quasicrystal from the diffraction pattern*, 57th Polish Crystallographic Meeting, 25-26th June 2015, Wroclaw, Poland, **poster**
8. **I. Buganski**, R. Strzalka, J. Wolny, *Estimation of the flip ratio in the 1D quasicrystal from the diffraction pattern*, 29th European Crystallographic Meeting, 23-28th August 2015, Rovinj, Croatia, **poster**
9. **I. Bugański**, R. Strzalka, J. Wolny, *Estimation of the flip ratio in the 1D quasicrystal from the diffraction pattern*, 8th Conference on Aperiodic Crystals, 30 August-4 September 2015, Praha, Czech Republic, **poster**
10. **I. Bugański**, R. Strzalka, J. Wolny, *Estimation of the flip ratio in the 1D quasicrystal from the diffraction pattern*, XXIII CAC 2015, Conference on Applied Crystallography, 20-24 September 2015, Krynica-Zdroj, Poland, **poster**
11. **I. Bugański**, R. Strzałka, J. Wolny, *The novel method of calculating corrections for phonons and phasons in quasicrystals,* C-MAC days 2015, 23-26 listopada 2015, Grenoble, Francja, **oral**
12. **I. Bugański**, R. Strzalka, J. Wolny, *Phason flips for an icosahedral quasicrystal*, 58th Polish Crystallographic Meeting, 23-24th June 2016, Wroclaw, Poland, **poster**
13. **I. Bugański**, R. Strzalka, J. Wolny, *Phasonic correction for quasicrystals – new definition*, AGH-HU joint Symposium 2016, 29-31.07.2016, Sapporo, Japan, **oral**
14. **I. Bugański**, R. Strzalka, J. Wolny, New approach to phasonic correction for quasicrystals, Kyoto-Krakow Symposium on Materials Science, 2.08.2016, Kioto, Japan, **oral**
15. **I. Bugański**, R. Strzalka, J. Wolny, H. Takakura, *The statistical description of the Cd-Yb icosahedral quasicrystal with the application of the novel concept of the phason disorder correction*, 18-23 September 2016, Kathmandu, Nepal, **oral**
16. **I. Bugański**, R. Strzalka, J.Wolny, *Phason flips in the statistical approach*, C-Mac days 2016, 21-23 November 2016, Bratislava, Slovakia, **oral**
17. **I. Bugański**, R. Strzalka, J. Wolny, *The frozen phason in quasicrystals: Moments' analysis and the analytical derivation,* 59 Polish Crystallographic Meeting, 29-30 June 2017, Wroclaw, Poland, **oral**
18. **I. Bugański**, J. Wolny, Additive phasonic correction for decagonal quasicrystal,C-MAC days 2017, 20-23 November 2017, Athens, Greece, **oral**
19. **I. Bugański**, K. Toyonaga, H. Takakura, J. Wolny, *The growth of the ZnMgHf icosahedral quasicrystal*, AGH-HU joint Symposium, 14-16.05.2018, Krakow, Poland, **oral**

20. **I. Bugański**, R. Strzałka, J. Wolny, *The refinement of the AlCuRh decagonal quasicrystal*, 28-29.06.2018, 60th Polish Crystallographic Meeting, Wroclaw, Poland, **poster**
21. **I.Bugański**, K. Toyonaga, H. Takakura, T. Yamada, M. De Doissieu, Oliver Perez, Pierre Fertey, 21. Janusz Wolny, *The structure formation of the F-type ZnMgHf Icosahedral quasicrusyal*, 8-13.07.2018, Aperiodic 2018, Ames, USA, **poster**
22. **I. Bugański**, R. Strzałka, J. Wolny, *New Technics for the refinement of quasicrystals*, 8-13.07.2018, Aperiodic 2018, Ames, USA, **oral**
23. **I. Bugański**, R. Strzałka, J. Wolny, *AlCuRh decagonal quasicrystal – new techniques for the refinement*, 22-27.08.2018, ECM31, Oviedo, Hiszpania, **poster**
24. **I.Bugański**, K. Toyonaga, H. Takakura, T. Yamada, M. De Doissieu, Oliver Perez, Pierre Fertey, Janusz Wolny, *The F-type icosahedral quasicrystal in ZnMgHf system*, 02-06.09.2018, XXIV Conference on Applied Crystallography, Arłamów, Polska, **poster**
25. **I. Bugański**, J. Wolny, H. Takkaura, *A real space structurerefinement of i-ZnMgTm*, 14th International Conferecne on Quasicrystals, 26-31.05.2019, Kranjska Gora, Słowenia, **poster**
26. **I. Bugański**, J. Wolny, H. Takakura, *The atomic structure of Bergman-type icosahedral ZnMgTm quasicrystal*, Interdisciplinary Symposium for Quasicrystals and Strongly Correlated Electron System, 23-27.06.2019, Sendai, Japonia, **poster**
27. **I. Bugański**, J. Wolny, H. Takakura, *The real space refinement of the icosahedral quasicrystal*, 32nd European Crystallographic Meeting, 18-23.08.2019, Vienna, Austria, **poster**
28. **I. Bugański,** J. Wolny, H. Takakura, *The real space structure solution of the P-type Bergman quasicrystal*, 2nd Hypermaterials meeting, 18-20th February 2020, Sendai, Japan, **poster**
29. **I. Bugański,** H. Takakura, *The structure factor of the Niizeki-Gähler tiling with phason flips*, 2nd Hypermaterials meeting, 18-20 February 2020, Sendai, Japan, **poster**

Prizes

1. The best oral presentation among young scientists for the presentation: *The novel method of calculating corrections for phonons and phasons in quasicrytsals*, C-MAC days 2015, 23-26 November 2015, Grenoble, France
2. The best poster prize founded by the Ausrian Academy of Sciences: *The real space refinement of the icosahedral quasicrystal*, 32nd European Crystallographic Meeting, 18-23 August 2019, Vienna, Austria
3. Grant PRELUDIUM 11, *The influence of the phason disorder on the diffraction pattern of quasicrystals*, 2016-2019